

Morphogenesis of pancreatic ductal adenocarcinoma-derived organoids

Samuel J. Randriamanantsoa

Vollständiger Abdruck der von der TUM School of Natural Sciences der Technischen Universität München zur Erlangung des akademischen Grades eines

Doktors der Naturwissenschaften (Dr. rer. nat.)

genehmigten Dissertation.

Vorsitz:

Prof. Dr. Ulrich Gerland

Prüfer der Dissertation:

1. Prof. Dr. Andreas R. Bausch
2. Prof. Dr. Maximilian Reichert

Die Dissertation wurde am 15.04.2024 bei der Technischen Universität München eingereicht und durch die TUM School of Natural Sciences am 02.05.2024 angenommen.

Abstract

The exocrine pancreas offers a formidable example of the tight link between form and function in biology. Enzymes crucial for digestion are produced in bud-like structures called acini, distributed over a large three-dimensional branched architecture, before being shuttled via a single seamless lumen toward the duodenum.

Pancreatic Ductal Adenocarcinoma (PDAC), a cancer developing in this organ, is a highly lethal disease, for which the 5-year survival rate has remained staggeringly low for the past 40 years [1], due to a combination of late diagnosis, aggressive metastasis, and poor efficacy of the treatments, which remain mostly palliative to this day [2].

To study morphogenetic events, understand disease progression, or test drugs in a biologically faithful environment, organoids - *in vitro* three-dimensional cell cultures that display features of an organ of interest - are a highly promising platform, that has been continuously rising in importance in the past decade. While great progress has been made in the generation of pancreas and PDAC organoids, shedding light on important biological aspects - such as the heterogeneity of tumour cell populations [3], or the existence of markers for increased tumour-formation potential [4] -, most of the state-of-the-art assays lead to the formation of sphere-like structures. Strikingly however, the precursor lesions of PDAC, known as Pancreatic Intraepithelial Neoplasia (PanIN) and Intraductal Papillary Mucinous Neoplasm (IPMN), also display three-dimensional, branched architectures, with terminal end buds and lumens [5, 6, 7], in crucial morphological contrast to spherical organoids.

Here, by embedding single murine PDAC-derived cells in a collagen matrix, we generate complex, three-dimensional organoids that display a branched structure, terminal end buds, and a lumen connecting the branched network, closely resembling the architectures of the exocrine pancreas and of its lesions. Through a combination of live imaging, chemical perturbations, immunostainings, and theoretical modelling, we investigate, in space and time, how cell motion, cell-cell interactions, extracellular matrix (ECM) interactions and protein expression combine to give rise to those final structures. We find that patterns in these features can be used to identify four phases of development, that we named Onset, Extension, Thickening, and Lumen Formation. From a fundamental research perspective, PDAC organoids provide a remarkable model system to study morphogenesis, and the self-organising processes involved in branching, budding, and lumen formation. From a clinical perspective, understanding how precursor lesions emerge and develop will provide important insights on the early events of cancer, before it progresses to advanced stages where treatment arrives too late to be effective.

Abstract

Das exokrine Pankreas ist ein hervorragendes Beispiel für die enge Verbindung von Form und Funktion in der Biologie. Die für die Verdauung relevanten Enzyme werden in den knospenartigen Strukturen des Pankreas, den sogenannten Azini, produziert und über dessen große dreidimensionale Architektur verteilt, bevor sie durch ein einzelnes Lumen zum Zwölffingerdarm transportiert werden.

Das duktales Adenokarzinom des Pankreas (PDAC), welches sich im Pankreas entwickeln kann, ist eine tödliche Erkrankung, bei der die 5-Jahres-Überlebensrate in den letzten 40 Jahren niedrig geblieben ist [1]. Die Ursache wird durch eine Kombination aus verspäteter Diagnose, aggressiver Metastasierung und schlechter Wirksamkeit der Behandlungen, die bis heute überwiegend palliativ sind, begründet [2].

In letzten Jahrzehnt haben Organoide, als vielversprechende Plattform für die Untersuchung von morphogenetischen Vorgängen, die Verbesserung des Verständnisses des Krankheitsverlaufs, sowie die Erprobung von Medikamenten in einer physiologisch relevanten Umgebung, an Bedeutung gewonnen, da diese *in vitro* dreidimensionalen Zellkulturen Merkmale des jeweiligen Organs aufweisen. Die Generierung von Pankreas und PDAC Organoiden verbesserte das Verständnis wichtiger biologischer Aspekte, wie beispielsweise die zelluläre Heterogenität von Tumoren und die Existenz von Markern zur Erkennung von Tumorerkrankungen. Obwohl die Mehrheit der aktuellen Forschung sich auf sphärische Strukturen bezieht, stehen diese im entscheidenden morphologischen Kontrast zu den Vorläuferläsionen von PDAC, die als Pancreatic Intraepithelial Neoplasia (PanIN) und Papillary Mucinous Neoplasm (IPMN) bekannt sind, welche dreidimensionale, verzweigte Architekturen mit terminalen Endknospen und Lumen aufweisen [5, 6, 7].

Die Einbettung einzelner muriner PDAC-Zellen in eine Kollagenmatrix führt zur Erzeugung komplexer, dreidimensionaler Organoide, die eine verzweigte Struktur, terminale Endknospen und ein Lumen, welches das verzweigte Netzwerk verbindet, aufweisen und der Architektur des exokrinen Pankreas und seiner Läsionen ähnlich sind.

Eine Kombination aus Mikroskopie von lebenden Zellen, biochemischen Störungen, Immunfärbungen und theoretischer Modellierung, ermöglicht die raum-zeitliche Untersuchung von Faktoren wie Zellbewegungen, Zell-Zell-Interaktionen, ECM-Interaktionen und Proteinexpression, die zur Erzeugung der endgültigen Struktur zusammenwirken. Anhand dieser Merkmale werden vier Entwicklungsphasen identifiziert, welche als Onset, Extension, Thickening und Lumen Formation benannt werden.

Aus Sicht der Grundlagenforschung sind PDAC-Organoide ein bedeutendes Modellsystem zur Untersuchung der Morphogenese und der selbstorganisierenden Prozesse, die bei der Verzweigung, der Knospung und der Lumenbildung eine Rolle spielen. Im klinischen Zusammenhang werden, durch die Verbesserung des Verständnisses der Entstehung und Entwicklung von Vorläuferläsionen, wichtige Erkenntnisse der Tumorbildung erhalten, bevor dieser ein fortgeschrittenes Stadium erreicht, in welchem Behandlungen, wie Resektionen oder medikamentöse Therapien, zu spät einsetzen, um wirksam zu sein.

Acknowledgments

First and foremost, I would like to deeply thank my Doktorvater, Prof. Andreas Bausch, for giving me the opportunity to perform research in his group, and for the trust, support, and good humour that he showed throughout my time here. Every meeting, although punctuated by mandatory (light-hearted) jokes about how French I was, was always insightful and left me eager to work. For this: *Merci Monsieur*.

I have had the privilege of working at the E27-E22 chair with colleagues of remarkable kindness and intelligence, who have made my time in the lab a wonderful experience. To Fabian Englbrecht, my long-standing office-mate, with whom strong bonds were formed upon cleaning the most disgusting office left for us on our first day at work. To Benedikt Buchmann, Henri Dehne, Alfredo Sciortino, Philip Bleicher and Pablo Fernández, senior figures of the lab for showing me the ropes when I was just a fledgling PhD student. To the members of the organoid group: Marion Raich, Franz Hutterer, Ann-Caroline Heiler, Sophie Kurzbach, Iris Ruider and Daphné Vannier, for always being so nice, for the stimulating discussions, and for bearing with me when the hardships of scientific publishing struck. Also, thank you all for dutifully putting in your talks “that one organoid timeline figure”, I can now pretend that I contributed to some pioneering work. To Kasia Tych, with whom I shared many pots of tea, and who would always provide both important professional advice, and exquisite conversation topics. To our TAs, especially Gabriele Chmel, and our secretary Katerina Girgensohn, for fielding all of my stupid questions, and without whom the laboratory would collapse in a second.

Much of this work would not have been possible without meeting Prof. Dr. Maximilian Reichert and Aristeidis “Aris” Papargyriou. I would like to sincerely thank them for being such bright research partners, for giving me the chance to perform true interdisciplinary research, and for tempering my (very physicist-like) tendencies towards the reductionism of biological systems. I am also grateful to Prof. Edouard Hannezo, with whom discussing the physics of our system and putting them into equations was salutary, at a moment where I started to doubt there was a place for “physics” in “biophysics”. Working with a physicist of his calibre was an honour.

Some of the most uplifting moments of my PhD came during the conferences I had the chance to attend. I lack the space to thank all the young and senior scientists I met there, and with whom we shared stories of successes and hardships. A special mention goes to the Lindau Nobel Meeting that I had the honour and privilege to attend. Seeing so many people sharing the idea of doing science for the greater good was the experience of a lifetime. Although the chances that they ever read this thesis are quite slim, I would like to acknowledge the exchanges I had with Prof. Christiane Nüsslein-Volhard, who was, to me, immensely inspirational as a human and as a scientist, and with Sir Richard Roberts who convinced me of the crucial role of science beyond the lab.

Lastly, my deepest thanks go to my family, my parents and my siblings, next to whom, throughout all my life, I have always found a warm and loving place.

Contents

Preface	1
1 Background and state of the art	5
1.1 Morphogenesis, structure formation, and the different models	5
1.2 Morphogenesis of a healthy pancreas	8
1.3 Elements of Pancreatic Ductal Adenocarcinoma	10
1.3.1 Incidence and prognosis	10
1.3.2 Available treatments	10
1.3.3 Pre-cancerous lesions	13
1.3.4 Stroma formation	14
1.4 Organoids	15
2 Branching morphogenesis formation in pancreatic organoids	17
2.1 Culturing three-dimensional PDAC organoids - Observations	17
2.2 Phases of development	18
2.2.1 Motion	21
2.2.2 Matrix interactions	23
2.3 A minimal biophysical model for the early phases of development	27
2.3.1 Rationale	27
2.3.2 Describing the model	29
2.3.3 Comparing model predictions to experimental results	32
2.3.4 Predicting the results of perturbations	33
2.4 Drug treatments - Functional experiments	36
2.5 Transcriptional programs at play	39
2.6 Discussion: on branching morphogenesis	41
3 Budding in pancreatic organoids	45
3.1 Focussing on bud formation - Rationale	45
3.2 Experimental results and hypotheses	45
3.2.1 The transition from Extension to Thickening: A competition between extension and retraction processes	45
3.2.2 Experimental results on key molecular players	46
3.2.3 Apparition of bud-shape structures	52
3.2.4 Inhibition experiments	57
3.3 Discussion: on budding	61
3.3.1 Organoid population not or less susceptible to batimastat treatment	61
3.3.2 What drives the change in the molecular players of tension	61

4	Lumen formation in pancreatic organoids	67
4.1	Focusing on lumen formation - Rationale	67
4.2	Hypotheses for lumen formation in pancreatic organoids	67
4.2.1	Mechanisms of luminogenesis	67
4.2.2	A Physics view of lumen formation	69
4.3	Results	72
4.3.1	Different phenotypes of lumens suggest different processes of lu- minogenesis	72
4.3.2	Fluid-based lumen formation: a focus on clear lumens	74
4.3.3	Cell death-based lumen formation: a focus on dark lumens	75
4.3.4	Epithelialisation and polarisation: a focus on the centre of the branches	76
4.4	Discussion: on luminogenesis	80
4.5	Perspectives: post-lumen formation	85
4.5.1	Known roles of lumens post-formation in other systems	85
4.5.2	Functionality in formed lumens	86
4.5.3	Pearl-like structure formation	87
5	Materials and methods	103
5.1	Ethics declaration	103
5.2	Mouse background	103
5.3	Cells and organoids manipulations	103
5.3.1	Two-dimensional (2D) cell culture of PDAC cells	103
5.3.2	Organoid preparation	104
5.3.3	Cloning and retroviral transfection	105
5.3.4	Chemical perturbations	105
5.3.5	Immunofluorescent staining	106
5.4	Imaging	107
5.4.1	Microscopes	107
5.5	Live imaging	108
5.5.1	General live imaging parameters	108
5.6	Image analysis tools	109
5.7	Data analysis	109
5.7.1	Estimation of organoid size	109
5.7.2	Bead branch tracking	109
5.7.3	Ki67 to DAPI ratio estimate	109
5.7.4	Cell nuclei number determination	110
5.7.5	Branch thickness measurement (live)	111
5.7.6	Branch thickness measurement (static)	111
5.7.7	Branch length measurement (live)	111
5.7.8	Branch counting (static)	111
5.7.9	Branching event counting	111
5.7.10	Collagen reflection microscopy	112
5.7.11	Intensity profiles and kymographs	112

5.7.12 Lumen type identification 112
 5.7.13 Lumen morphometrics 112
 5.7.14 Apoptotic event counting 113
 5.7.15 Figure preparation 113

Appendix 115

1 Permissions, data availability, and authors contributions 115
 1.1 Permissions 115
 1.2 Availability of data, materials, and code 115
 1.3 Contribution of authors to collaborative figures 115
 2 Experimental challenges brought by branching PDAC organoids 117
 2.1 The question of heterogeneity and reproducibility in organoid culture: problems and opportunities 117
 2.2 Imaging challenges 118
 2.3 Analysis challenges 118
 3 Additional methods 120
 3.1 Two-dimensional (2D) cell culture of pancreatic ductal cells (PDCs) 120
 3.2 Orthotopic implantation into mice 120
 3.3 Histology 120
 3.4 RNA-isolation 121
 3.5 RNA-sequencing 121
 3.6 Statistical analysis of gene expression data 121

List of Tables

5.3	Additional fluorescent probes.	106
5.1	Primary antibodies.	107
5.2	Secondary antibodies.	108
5.4	Objective list.	108

List of Figures

0.1	NIH categorical spending	1
0.2	Schematic representation of the pancreas	3
0.3	Haematoxylin and eosin-stained section of a high grade PanIN	3
1.1	PubMed search for “morphogenesis”	6
1.2	Whipple procedure	11
2.1	Schematic of the floating collagen gel assay preparation	19
2.2	Matrigel- and collagen-grown organoids exhibit strikingly different morphologies	20
2.3	Comparing healthy and cancerous structures, in primary tissues and in organoids	21
2.4	From a single cell to a complex branched structure	22
2.5	Major axis length evolution of collagen-grown organoids over time	22
2.6	Diversity of organoid morphologies at Day 13	23
2.7	Organoids interact with the ECM and remodel it	25
2.8	Organoids plastically remodel their environment	26
2.9	Cell-ECM interactions.	27
2.10	Summarised patterns of organoids’ development phases	29
2.11	Migration directionality and branching events during the Extension phase	30
2.12	Correlation between branching and proliferation events	31
2.13	Evolution of the normalised volumetric growth rate per day of branches according to their width	34
2.14	Complementary empirical cumulative distribution function of non-terminal branch lengths	34
2.15	Evolution of the branch number per organoid over time	35
2.16	A minimal biophysical model captures the main morphogenetic dynamics from the onset phase up to the early thickening phase.	36
2.17	Sensitivity analysis for the minimal biophysical model.	38
2.18	Perturbing the structure formation processes	39
2.19	Effect of MMP-inhibition on structure formation	40
2.20	Transcriptional profiles in organoids at Day 7 and 13	42
2.21	Transcriptional profiles of Matrigel- and collagen-grown organoids at Day 13	43
3.1	Representative time-lapse of F-actin distribution in branches and buds	46
3.2	Representative time-lapse of cell membrane intensity in a YFP-Caax 9591 cell line during the Thickening phase	47

List of Figures

3.3	Representative time-lapse of myosin intensity in a GFP-tagged 9591 cell line during the Thickening phase	47
3.4	F-actin and PMLC2 distribution in organoids with lumens	48
3.5	Representative time-lapse of E-cadherin intensity in a mNeonGreen-tagged 9591 cell line during the Thickening phase	49
3.6	Complementary empirical cumulative distribution functions of cell mean velocities in organoids at different time points	50
3.7	Bud forming after adhesion loss at the tip	50
3.8	Schematic balance of forces exerted on a branch	52
3.9	Caption	56
3.10	Breakage events in the Extension and in the Thickening phases	59
3.11	Phenotype dependency - Calyculin	60
3.12	Perturbation experiments support the surface tension increase hypothesis	65
3.13	Concentration dependency - Blebbistatin.	65
4.1	Schematic view of known processes of lumen formation	73
4.2	Coexistence of clear and dark lumens	79
4.3	Fluid intake and fluid transfer contribute to clear lumen formation.	81
4.4	Time-lapse of microlumen nucleation and fusion and influence of forskolin	82
4.5	Apoptosis contributes to dark lumen formation <i>via</i> cavitation, and to cell elimination in the apical and basal directions.	91
4.6	Supporting measurements for clear and dark lumens.	93
4.7	Organoids undergo progressive epithelialisation and polarisation along the central (fault) line	95
4.8	Effect of perturbations of actomyosin dynamics on lumen formation	96
4.9	Clearing of cells in cavities	97
4.10	Transport of fluid and materials in lumens	98
4.11	Lumens can retain molecules	99
4.12	Mucin distribution	101
4.13	Pearl-like structures in organoids at day 24.	101
5.1	DAPI (blue) and Ki67-positive (green) cell numbers estimated from maximum projections using manual or semi-automated counting, at day 3, 5, 7, 9,11, and 13 (n = 24 organoids). Reproduced and adapted from [8].	110

Preface

From the first cell divisions patterning an embryo, to the properly timed elimination of diseased cells in an organism for its recovery, the spatiotemporal regulation of biological processes is a crucial feature of life.

Cancer, a large group of diseases characterised by an unregulated growth of abnormal cells spreading uncontrollably, is a tragic example of this regulation going awry.

The consequences are devastating: in 2020, 10 million deaths worldwide - approximately one in six deaths - could be attributed to cancer [9]. This toll is projected to reach a staggering macroeconomic cost of \$25.2 *trillions* from 2020 to 2050 [10].

Considerable effort has been, and is still, dedicated to addressing this global issue: for the fiscal year 2023, the American National Institutes of Health were granted a budget of more than 8 billion USD for cancer research alone [11].

Research/Disease Areas (Dollars in millions and rounded)	2015	2016	2017	2018	2019	2020	2021	2022	2023 Estimated	2024 Estimated	2020 US Mortality ¹⁹	2020 US Prevalence SE ¹⁹
Clinical Research	\$11,366	\$12,176	\$12,695	\$13,870	\$15,868	\$17,610	\$17,681	\$18,002	\$18,795	\$19,235	-	-
Genetics	\$7,480	\$8,070	\$8,501	\$9,105	\$9,864	\$10,544	\$11,010	\$11,615	\$12,189	\$12,445	-	-
Neurosciences	\$5,742	\$6,460	\$7,317	\$8,224	\$9,468	\$10,122	\$10,716	\$11,294	\$11,882	\$12,155	-	-
Prevention	\$7,027	\$7,566	\$8,052	\$8,757	\$9,485	\$10,482	\$10,553	\$10,952	\$11,369	\$11,596	-	-
Biotechnology	\$6,018	\$6,433	\$6,556	\$6,923	\$7,219	\$7,767	\$7,847	\$8,604	\$8,960	\$9,137	-	-
Brain Disorders	\$3,916	\$4,577	\$5,156	\$5,882	\$6,954	\$7,565	\$7,963	\$8,492	\$8,770	\$9,011	-	-
Infectious Diseases	\$5,032	\$5,518	\$5,684	\$6,024	\$6,313	\$8,301	\$8,212	\$8,161	\$8,463	\$8,491	-	-
Behavioral and Social Science	\$3,762	\$4,137	\$4,547	\$5,096	\$6,499	\$7,040	\$7,329	\$7,849	\$8,199	\$8,382	-	-
Cancer	\$5,389	\$5,589	\$5,980	\$6,335	\$6,520	\$7,035	\$7,362	\$7,635	\$8,078	\$8,786	708,729	9.6% (0.19%)
Clinical Trials and Supportive Activities ¹⁷	\$3,136	\$3,476	\$3,775	\$5,207	\$6,058	\$6,637	\$6,480	\$6,560	\$6,831	\$6,987	-	-
Rare Diseases	\$3,679	\$4,342	\$4,613	\$5,227	\$5,655	\$5,947	\$6,191	\$6,515	\$6,807	\$7,070	-	-
Bioengineering	\$3,540	\$3,841	\$4,106	\$4,592	\$5,091	\$5,646	\$5,720	\$6,231	\$6,635	\$6,762	-	-
Aging	\$2,698	\$3,150	\$3,572	\$4,084	\$4,653	\$5,276	\$5,657	\$6,044	\$6,282	\$6,342	-	-
Pediatric	\$3,632	\$3,959	\$4,176	\$4,499	\$4,922	\$5,347	\$5,465	\$5,707	\$5,919	\$6,081	-	-
Health Disparities ³⁰	\$2,825	\$3,093	\$3,168	\$3,178	\$3,381	\$3,484	\$4,362	\$4,901	\$5,246	\$5,318	-	-
Human Genome	\$2,891	\$3,200	\$3,274	\$3,626	\$3,895	\$4,340	\$4,293	\$4,770	\$5,056	\$5,123	-	-
Neurodegenerative	\$1,662	\$2,058	\$2,554	\$3,085	\$3,578	\$4,021	\$4,463	\$4,819	\$4,987	\$5,051	-	-
Women's Health ⁸	\$3,989	\$4,540	\$4,769	\$5,048	\$4,469	\$4,466	\$4,610	\$4,593	\$4,802	\$4,969	-	-

Figure 0.1: NIH categorical spending. Cancer category highlighted in blue. From [11].

With this, tremendous improvement has been possible, through a combination of better prevention, detection, and treatment [9]. Indeed, for all sites of cancer combined, the 5-year relative survival rate rose from 49% in 1975-77 to 68% in 2012-18 [12]. For

List of Figures

instance, within this timeframe, 5-year survival rates for cancers in sites such as kidney (50% to 77%), breasts (75% to 91%), or prostate (68% to 97%), saw considerable gains [12].

There remains however cancers that have not benefitted from those improvements, and for which the survival rates remain staggeringly low.

In particular, pancreatic ductal adenocarcinoma (PDAC), a disease developing in the exocrine part of the pancreas, barely saw its 5-year survival rate improve from 3% in 1975-77 to 12% in 2012-18, and stands today as one the most lethal forms of cancer [12], principally due to a combination of poor diagnosis, treatment inefficacy, and extremely aggressive tumour development and metastatic spread [2, 13].

Three main challenges therefore emerge to improve this bleak picture:

- Finding reliable cancer markers to perform diagnosis as early as possible.
- Developing a system, as faithful as possible to the real organ or tumour, to engineer and test new therapies.
- Understanding the dynamics through which tumours grow and progress.

The high PDAC lethality predictably hinders direct patient studies, and thus animal models and *in vitro* systems remain the first options for research.

Animal models allow studies in entire organisms, thereby retaining important complex interactions between the multiple parts of the system. However, this complexity conversely makes the clear determination of biological mechanisms difficult

In contrast, *in vitro* models, through a drastic reduction of system complexity, have made the isolation of individual biological mechanisms possible, but simultaneously run the risk of being over-simplified and unrelated to the patient's reality.

The past decade saw the emergence and development of organoid technology *in vitro* systems of cells growing in three dimensions and recapitulating important features of the organ modelled, while remaining tractable from an experimental and analytical point of view [14, 15].

This promising technology has been applied with great success to pancreas and PDAC research, be it to mimic development processes [16, 17, 18, 19] or to assess therapy efficacy [20, 21, 22, 23].

Despite the achievements obtained in recapitulating biological features, most, if not all, of the pancreas and pancreatic cancer organoids form sphere-like structures called *spheroids*. Yet, both the exocrine pancreas, and the PDAC precancerous lesions are anything but spherical.

Both structures indeed exhibit a highly three-dimensional architecture, displaying branches, terminal buds, and a lumen connecting this network [7] as visible in Fig. 0.2, 0.3.

Physicists will be familiar with the concept of the “spherical cow”, a tongue-in-cheek jab at the (over-)simplification of the system that occasionally accompanies the analysis

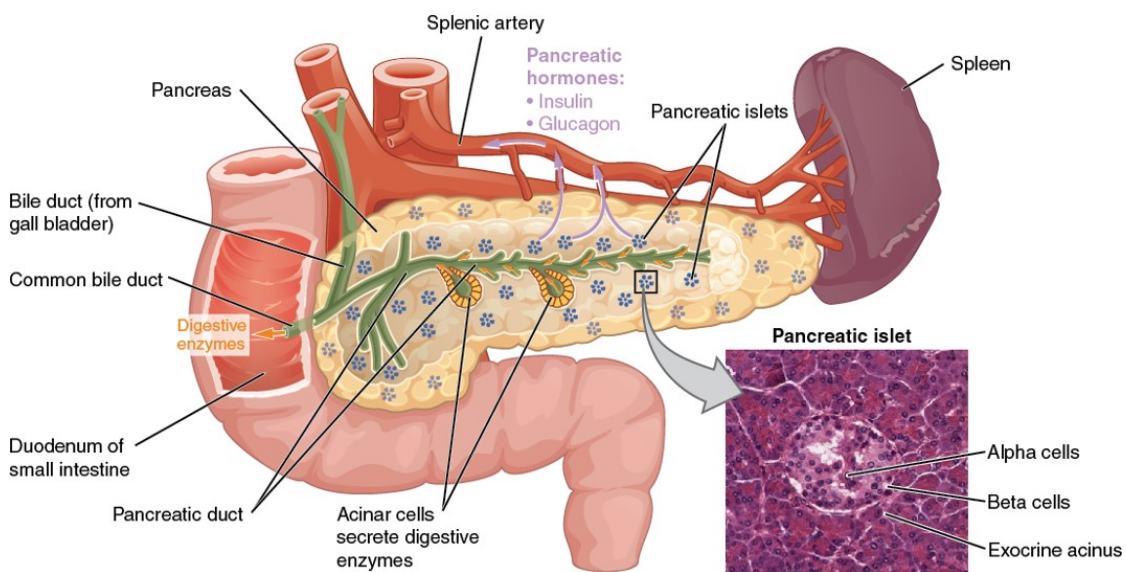


Figure 0.2: Schematic representation of the pancreas. Credit: *Human Anatomy and Physiology* - Rice University 2019. Micrograph provided by the Regents of University of Michigan Medical School ©2012

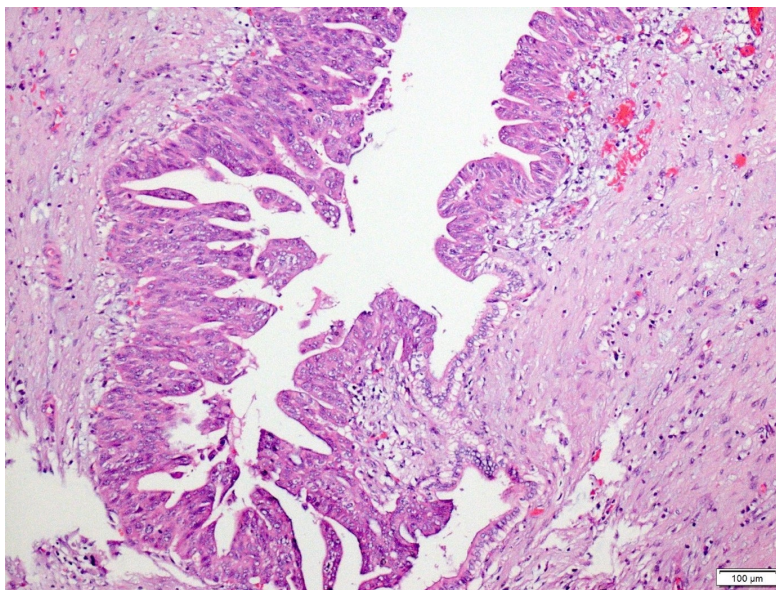


Figure 0.3: Haematoxylin and eosin-stained section of a high grade PanIN, a precancerous lesion. Credit: Ayşe Armutlu - <https://www.pathologyoutlines.com/topic/pancreaspanin.html>

List of Figures

of a problem by theoreticians.¹

Yet, this cheeky concept contains a warning that experimentalists should also heed: in one's quest towards achieving *function*, one should take care not to lose too much of the *form*.

In biology especially, form and function are tightly associated: the branched architecture of the exocrine pancreas allows the production of digestive enzymes in buds (the acini) over a distributed network, which are then shuttled through a seamless lumen towards the duodenum. Similarly, the behaviour of a drug on a flat two-dimensional layer of cells is certainly different from its behaviour in a dense, complex, three-dimensional tissue.

To bridge this morphological gap, we therefore set to go beyond spheroids, and attempted to achieve closer morphological likeness for PDAC organoids.

This thesis describes a novel three-dimensional assay, in which an initial single PDAC cell can proliferate and self-organise into a complex three-dimensional tissue that bears morphological hallmarks of the exocrine pancreas and of its precancerous lesions, namely: a branched architecture, terminal end bud-like structures, and a single seamless lumen connecting every branch.

An introduction chapter will first present elements of morphogenesis, of pancreatic ductal adenocarcinoma, and a general overview of the state-of-the-art for organoids and their capabilities.

Then, in a second chapter, this thesis will focus on the spatio-temporal dynamics that lead to the establishment of a branched architecture in organoids, through cell proliferation, invasion of the matrix, and stochastic branching. A minimal theoretical model accounting for these elements was able to recapitulate the experimental observations and will also be described.

A third chapter is devoted to the phenomenon of budding, by which the tips of the branched organoid round up and start resembling the terminal buds of a pancreas or of a pancreatic lesion, accompanied by an epithelialisation of the tissue. In particular, the chapter discusses the behaviour of molecular players in tissue surface tension, such as actin and myosin for active contractility, and E-cadherin for cell-cell adhesion, to understand the role of forces in the emergence of buds.

Lastly, a fourth chapter is dedicated to the processes by which a single seamless lumen is formed. Remarkably, this work finds that multiple processes, such as cell death, fluid intake, and the establishment of apico-basal polarity, contribute to the apparition of a tubular network.

In summary, this thesis aims to provide a biophysical description of the morphogenetic events and dynamics that characterise the development of PDAC organoids, from their onset as a single cell, to their final multicellular structure.

¹This joke has countless versions. Here is one of many: "Milk production at a dairy farm was low, so the farmer wrote to the local university, asking for help from scientists. A theoretical physicist took up the challenge, and spent two weeks intensively working to find a solution to the problem. At last, the physicist emerged from his office and, upon returning to the farm, told the farmer: 'The solution is as follows: let us first assume a spherical cow...'"

1 Background and state of the art

This thesis will focus on the processes that allow cells to build *in vitro* complex three-dimensional structures called *organoids*, that reproduce features of an organ or tumour of interest. This chapter will first provide some generalities on morphogenesis, before focusing on the morphogenesis of the healthy pancreas, and on the development of pancreatic ductal adenocarcinoma (PDAC), a highly lethal form of cancer developing in it.

We will then introduce the organoid technology, and the perspectives it might open for new research avenues, facing the bleak prognosis of PDAC and its lack of effective treatment.

1.1 Morphogenesis, structure formation, and the different models

Morphogenesis, the ensemble of processes by which organs and tissues are formed and patterned is a fundamental question that has been, and is still, actively explored across species - from nematodes like *C. elegans* and fruit flies like *Drosophila melanogaster* to humans - and across scales - from the emergence of a whole organism, to the molecular interactions at play within a single cell -.

This topic has generated considerable interest, existing from as far back as the Antiquity [24]. A simple query of the PubMed database for the term “morphogenesis” reveals an astonishing 502 894 results appearing between 1898 and 2023 (Fig. 1.1).

To a biophysicist, morphogenesis stands as a fascinating object of research, as it sits at the intersection of both Biology and Physics. From the work of Crick, Franklin, Watson, and Wilkins who elucidated the structure and the role of DNA as the carrier of the genome, to the work of Nüsslein-Volhard, Wieschaus and Lewis discovering the genes controlling regulating early embryonic development, the latter half of the 20th century has seen tremendous advances in our understanding of how biological information is stored and gives rise to complex structures. Although the developmental *biology* interpretation, based on genes and molecules, might appear for the modern reader as the mainstream view of morphogenesis, one should note that a *physics-based* interpretation actually existed as the dominant view prior. The current of *Entwicklungsmechanik* (German for “developmental mechanics”), notably pioneered by the work of Wilhelm Roux, sought to understand the tissue remodelling occurring during embryogenesis through the prism of mechanics before being phased out in favour of the developmental biology experimental paradigm consisting of “identify[ing] genes, ‘knock[ing]’ them out, and see[ing] what stops” [25]. The recent decades have however seen a return of physics in

1 Background and state of the art

an attempt to explain both the mechanics of tissue changes during morphogenesis, but also the existence of larger organising principles [25]¹

By merging the biological and the physical approaches, biophysics might thus help bridge “the gap between genotype and phenotype” and understand how the massive amount of information encoded in the genome is extracted, parsed, and transcribed into morphogenetic events that give rise to an organism [24].

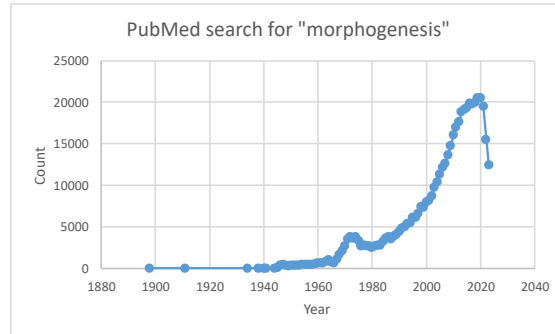


Figure 1.1: **PubMed search for “morphogenesis”**. Query performed on 16.01.2024, up to 2023.

As morphogenesis encompasses a multitude of processes leading to the formation of a multitude of shapes and organs, an exhaustive review is beyond this manuscript. This thesis will instead introduce some general concepts, and primarily focus on the formation of two fundamental types of structures: branches and tubes. For a deeper introduction, the reader may refer to some of the following reviews [24, 29, 30, 31].

Self-organisation and robustness are particularly remarkable features of these processes. Indeed, in the case of mammalian embryos for example, the fertilized egg cell, will, reliably² and without having to rely on a central “leader” giving instructions to each of the agents, develop into a fully fledged organism. This cell will divide, form the initial morula, generate a cavity to form the blastocyst, and, following implantation, undergo gastrulation - establishing the main body axes -, neurulation - forming the precursors of the central nervous system -, and organogenesis - giving the body its organs -.

Several components there play a role in the patterning, fate determination and shaping of the tissue, that we describe briefly below, drawing from the review of Gilmour, Rembold and Leptin[24].

Patterning at the large scale level can occur via morphogens, signalling molecules which, through their varying local concentration leading to gradients across the tissue, act on cells differentially to specify their fate, by activating signalling cascades [24]. In mammals, molecules such as transforming growth factor β (TGF- β), sonic hedgehog

¹The seminal book of D’Arcy Thomson “*On Growth and Form*” [26, 27] published more than a century ago, represents one of the most celebrated attempt at interpreting the apparition of shaped biological structures through the prism of physics and mathematics, that is still revisited and debated to this day [28], illustrating the longevity of this *physics-based* approach.

²In healthy, non-pathological cases.

1.1 Morphogenesis, structure formation, and the different models

(SHH), bone morphogenic protein (BMP), epithelial growth factor (EGF) or Wnt have been reported to act as such morphogens [24, 32, 33, 34, 35].

At a local level, following morphogen signalling, transcription factors such as Twist and Snail may be activated, which will then induce or repress the activation of proteins that will alter the cell behaviour and fate [24].

Lastly, effectors in cell motility (actomyosin), cell-cell adhesion (cadherins), cell-ECM adhesions (integrins), or cell polarity (polarity complexes) to name a few, will remodel the tissue [24].

In addition to this signalling cascade - or more accurately loop, as downstream elements of the process can act as feedback on upstream elements -, additional biophysical factors may affect morphogenesis. The ECM composition and stiffness can affect the ability of cells to develop certain structures such as lumens [36]. The curvature of the tissue and the apicobasal mechanical Curvature, apicobasal mechanical tension, and fluid intake may likewise drive and alter tissue morphogenesis [37, 38].

Despite the variety of genes, morphogens, transcription factors and signalling networks that have been evidenced during the past decades, recent work has aimed to identify commonalities in the morphogenesis of similar structures, beyond their biological peculiarities.

In the case of branching morphogenesis, the extensive knowledge acquired on the signalling pathways involved [39, 40] does not directly translate into knowledge of the principles that govern the size of branches, the topology of the network, or the coordination of hundreds or thousands of elongating tips required to form an organ [41].

To answer those questions, models drawing from physics have sought to establish frameworks that could, without delving into the underlying cellular and molecular complexity, recapitulate the statistical properties of observed experimental systems, by focusing on general design principles. The branching-annihilating random walk (BARW) model is a representative example of this current [41]. There, the authors considered the branched architecture of the murine mammary gland epithelium, and found that a “stochastic and time-invariant program of tip branching”, with ductal elongation, random branching and competition between tips, was capable of recapitulating the branching morphogenesis. Strikingly, this model identified cell density as a feedback mechanism that could, simply, regulate the growth of the organ, in a self-organising manner, a finding that indicates that morphogenesis is not necessarily orchestrated following a precise, pre-determined sequence of orders [41]. Underscoring the possibility to generalise these findings to a different organ, the model was found to also be capable of recapitulating the development of the murine kidney [41].

In spite of the general biophysical processes identified, the biological context may still matter, and imply some tailoring for the model to perform well. For instance, applying the “vanilla” BARW model to the development of the murine salivary gland fails to recapitulate important properties such as the subtrees sizes or the duct length [42]. To adapt the model to this system, one should account for the fact that not every tip of the developing salivary gland has the same potential to contribute to branch generation: indeed, there exist some heterogeneity in the proliferation capabilities of cells in the network (indicative of a non-stationary growth process) [42]. Furthermore,

1 Background and state of the art

one should account for the fact that the network develops surrounded by a mesenchyme that concomitantly expands, correlating the proliferation of the cells in the two domains [42]. With these additions, an inflationary branching-delayed random walk (IBDRW) model can then be proposed, which exhibits much better quantitative agreement with the experimental data [42].

For an introduction to the variety of models that seek to identify overarching design principles for branching morphogenesis, the reader may refer to the following review written by Hannezo and Simons [43].

1.2 Morphogenesis of a healthy pancreas

While the organoids that constitute the focus of this thesis are derived from PDAC a disease that develops in the adult pancreas, understanding the morphogenetic processes at play in the developing pancreas may provide important clues on the self-organisation mechanisms used in organoid formation.

This section largely draws from a comprehensive 2021 review written by Flasse, Schewin, and Grapin-Botton [44], to which we refer the reader. For a review of pancreatic development illustrated by numerous stainings at important embryonic days, the reader can refer to a 2007 review by Jorgensen *et al.* [45].

Primordium formation

In the murine pancreas, the primordium emerges from the posterior foregut endoderm, from cells expressing the PDX1 transcription factor, giving rise to the dorsal bud at embryonic day 8.75 (E8.75).

This single-layered bud then undergoes stratification, becoming multi-layered, and the ventral pancreatic bud forms around E9. At E9.5 pancreatic progenitors, endocrine progenitors and differentiated endocrine cells - characterised by glucagon expression -, will appear. Towards E10-E10.5, the epithelium will have developed into a multi-layered structure surrounding a primary central lumen connecting the developing pancreas to the gut tube. Molecularly, the pancreatic progenitors at this stage are characterised by the expression of Pdx1, Hlx9, Ptf1a, Nkx6-1, Nkx2-2, Nkx6-2 and Sox9 [45]. Cells at the periphery of the epithelium named “cap cells” are anchored to the basal lamina - composed of laminin and collagen - through integrins, but are not yet displaying apical polarity markers, contrary to cells facing the central lumen that express aPKC, PAR3, Ezrin and ZO1 [44]. Cells in-between, the “body cells” are disorganised and unpolarised.

Microlumen formation

The next main restructuring of the tissue occurs between E10.5 and E11.5, where cap cells and body cells acquire apical polarity, evidenced by ZO1 a marker for tight junctions [46]. Multiple microlumens, unconnected with the primary lumen, emerge in the centre of rosettes of cells distributed in the epithelium, along with a downregulation of E-cadherin and phosphorylated Myosin light chain thought to be mediated by PDX1.

While the exact mechanism through which those microlumens appear remains unclear, reports have evidenced that apoptosis was not observed at that point, ruling out the so-called “cavitation” mechanism [47, 48, 49] at play in the mammary and salivary gland [32, 50]. Experiments however suggest that cell junction rearrangement combined to apical membrane domain expansion [46] contribute to this luminogenesis process.

Between E11.5 and E12.5, epithelial cells further reorganise and microlumens start connecting, forming an early branched network. This coalescence process appears to require the involvement of atypical protein kinase C (aPKC), PAR3, PAR6, Crumbs3 and Cdc42 [46, 51], while further luminogenesis is likely fuelled in the cap regions by vesicle trafficking [52]. To remodel the connections between microlumens into monolayers, the Rho GTPase activating protein Stard13 was found to be essential [53]

Tip-trunk segregation

At E12.5 the dorsal and ventral pancreatic buds have fused, and the epithelium now displays invaginations at its surface that denote the position of future branch tips. The multipotent pancreatic progenitors undergo a progressive fate restriction, starting their specification toward the ductal, acinar or endocrine identity [54]. Through branch tip splitting *via* a mechanism of clefting and bifurcation [55], budding and lateral branching [46, 56], the pancreas then develops a non-stereotypical branched architecture. Note that in addition to the changes happening at the molecular level, proliferation and cell motion and deformation also plays a large role in the tissue remodelling [57]. The multiple lumens are at this stage hyperconnected, with redundancies, and without a sense of hierarchy in the network [58]. Towards E14.5, redundancies are pruned, and the network starts adopting a more hierarchical structure. Tip cells in the branches will give rise to the acini whereas the trunk of the branches will form the pancreatic ducts. The future endocrine pancreas will form from cells delaminating from the main body.

Plexus remodelling and pancreatic tree development

After E14.5, the lumen plexus (*i.e.* the interwoven network of cavities) starts resolving into the ductal system, and thick interlobular ducts connect thin intralobular ducts in the hierarchical tree, by day E17.5.

Concomitantly, heavy branching morphogenesis can be observed driven by a combination of multipotent and fate-restricted progenitors [54]. These progenitors, located at the terminal parts of ducts, undergo proliferation contributing to the duct elongation, and stochastically bifurcating, thus forming new branches [54]. When an elongating branches approaches an existing duct, the branch terminates, and the acinus maturation process begins [54].

While this section has primarily described the development of the murine pancreas, the reader can refer to the work of Dolensšek, Rupnik and Stožer for a comparison with the human pancreas [59].

1.3 Elements of Pancreatic Ductal Adenocarcinoma

1.3.1 Incidence and prognosis

PDAC is a highly lethal cancer - principally developing in the exocrine part of the pancreas -, which, despite representing only 3% of the new cancer cases in males and females in the United States in 2020, ranks fourth in the leading cancer-related death cases ranking, accounting for 8% of the deaths [1]. Whereas most cancers benefitted from advances in prevention, detection and therapy, with a combined 5-year survival rate of 69% in 2015, PDAC prognosis has remained staggeringly low, with a 5-year survival rate barely rising from 3% to 9% in the span of forty years [1].

Indeed, patients display very little symptoms before the disease reaches an advanced stage, with the majority (53%) of the patients presenting and being diagnosed at a distant stage [1]. This lack of symptoms is further compounded by the absence of biological markers that would allow early detection.

1.3.2 Available treatments

Surgery

Resection, the surgical removing of the entirety or parts of the diseased tissue, remains to date the “only realistic and potentially curative option” [2]. Procedures have considerably improved since the 1970s and 1980s, with better pre-operative selection of resectable patients, increase in surgeon experience, minimisation of invasiveness, blood loss and operative time, and improvement of critical care [60, 61].

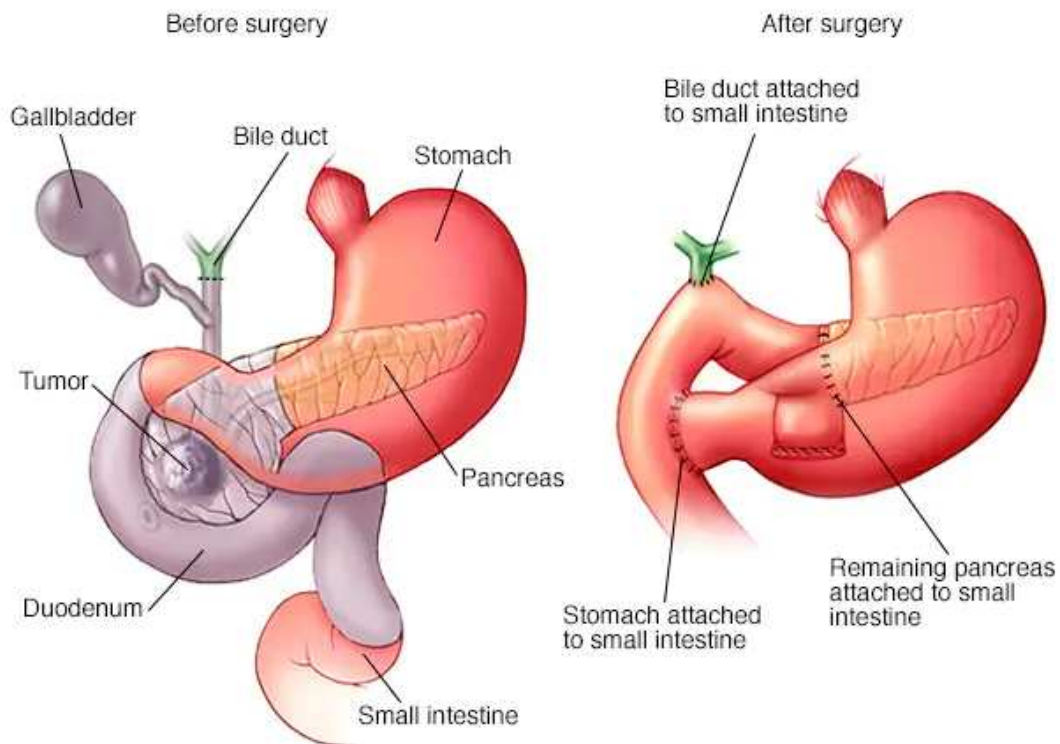
Depending on the location and involvement of the tumours, different surgical procedure are performed. In the case of pancreaticoduodenectomy, also known as a Whipple procedure (see Fig. 1.2), the head of the pancreas, as well as a large part of the duodenum, bile duct, gallbladder, and the lymph nodes associated with it, is removed. For distal pancreatectomy, the body and tail of the pancreas are removed. Lastly, in the case of total pancreatectomy, the entirety of the pancreas is ablated, which leaves patients unable to produce digestive enzymes or insulin, necessitating an external supplementation for the rest of their life [62].

However, tumours can only be realistically removed on patients that are at an early stage of the disease, which unfortunately represents a minority of the diagnosed cases (less than 20% in 2000 [61]). Indeed, upon PDAC progression, tumours can infiltrate the space surrounding a nerve (perineural invasion), the retroperitoneal space (kidney, duodenum, etc.), disseminate through the bloodstream (haematogenous dissemination), or invade major vessels such as the hepatic artery, which renders the cancer unresectable [2].

Chemotherapy

Upon metastasis and in absence of a resection possibility, chemotherapy, potentially coupled to radiotherapy, becomes the main option for treatment, despite only mild im-

1.3 Elements of Pancreatic Ductal Adenocarcinoma



© MAYO FOUNDATION FOR MEDICAL EDUCATION AND RESEARCH. ALL RIGHTS RESERVED.

Figure 1.2: **Whipple procedure.** Credit <https://www.mayoclinic.org/tests-procedures/whipple-procedure/about/pac-20385054>, accessed 03/04/2023.

1 Background and state of the art

provement on the patients' survival and quality of life.

While an exhaustive list of the therapies proposed to treat PDAC is beyond the scope of this thesis, we will introduce below some of the major attempts, drawing from the comprehensive review of Adamska, Domenichini, and Falasca [2].

Historically, 5-fluorouracil (5-FU) has been administered in PDAC treatment, either alone, or in combination therapies. 5-FU is thought to act primarily by inhibiting the production of deoxythymidine monophosphate (dTMP), essential for DNA replication and repair [63]. Additionally, a secondary mode of action was also reported through incorporation of 5-FU in DNA and RNA, causing cytotoxicity [63]. The drug was however found to provide (very) mild clinical benefits, while being highly toxic and triggering multiple adverse effects. In a clinical study treating 63 advanced pancreatic cancer patients with 5-FU, clinical benefit response was observed in only 4.8% of the patients, with a 12-month survival rate of 2% [64].

5-FU was progressively replaced by gemcitabine, which now constitutes the standard for first line therapy, improving both the clinical benefits and the 12-month survival rate (respectively 23.8% and 18% in the aforementioned clinical study [64]). Upon cellular uptake and phosphorylation, gemcitabine triphosphate inhibits DNA chain elongation, competing with oxycytidine triphosphate, leading to DNA damage and cell death [65]. Despite those improvements, the median survival rate of patients treated with gemcitabine as a single agent remains abysmal at around 5.65 months [64].

To further improve the efficacy of treatments, combination therapies were developed, among which Abraxane and FOLFIRINOX are two notable ones. Abraxane is a combination of gemcitabine with albumin-bound paclitaxel, the latter of which is thought to improve intratumoral delivery and inhibits microtubuli function. Patients treated with Abraxane showed increased overall survival, one-year survival and progression-free survival compared to gemcitabine-only-treated patients, at the cost of increased adverse effects such as neutropenia (decrease in neutrophils levels), leukopenia (decrease in leukocytes levels) or neuropathy (nerve damage). FOLFIRINOX is a combination of irinotecan, oxaliplatin, fluorouracil and leucovorin that was also shown to be superior to gemcitabine-only in terms of overall survival, progression-free survival and one-year survival. This treatment also helped reduce the deterioration in quality of life for patients, but increased incidence of adverse effects such as neutropenia, thrombocytopenia (decrease in platelets levels), or diarrhoea was observed [2].

Thus, in addition to the aforementioned therapies which appear to act through non-specific cellular uptake, so-called "targeted therapies" have emerged, that target particular mutations, growth factors, or receptors, more specific to cancer cells. The analysis of more than 600 whole PDAC exomes and genomes stored by the International Cancer Genome Consortium has revealed that four genes are commonly altered in PDAC: *KRAS* in 90% of the cases, *TP53* in 80%, *CDKN2* in 60% and *SMAD4* in 40%, plus a variety less frequently altered genes such as *ARID1A*, *KDM6A*, *RNF43*, *TGFBR2*, *GNAS*, *MAP3K21*, *BRAF*, *SMARCA4*, *ACVR2A*, *ACVR1B*, *NRAS*, and changes in the Notch, Wnt, TGF- β , Ras/MAPK/PI3K and JAK-STAT pathways, among many other [66]. PDAC exomes were found to display 40 simple somatic mutations on average, along with around 6000 in the genome [66]. Although beyond the scope of this thesis, the reader

may find that different cancer subtype classifications have been proposed based on the observed patterns of gene expression, notably the so-called Colisson, Moffitt, and Bailey classifications, along with the Chan-Seng-Yue and Kalimuthu classifications [66].

While targetting one of the four main mutated genes seems like a promising idea at first glance, early results appear disappointing. For instance, direct, upstream, or downstream inhibition of *KRAS* yielded results that were not better than the existing standard of care [2]. Exceptions to this trend include, among others, Erlotinib, an Epidermal Growth Factor Receptor (EGFR) inhibitor, and inhibition of *JAK1* and *JAK2* in patients resistant to gemcitabine [2], while molecules targetting *TP53* are being tested.

The high heterogeneity in PDAC at the tumour, patient and population levels [67, 68, 69], combined with the difficulty to predict a therapy's efficacy [21], the late diagnosis, and aggressive metastases, conspire to make PDAC a highly lethal disease.

1.3.3 Pre-cancerous lesions

As the treatment of advanced forms of carcinoma appears extremely challenging, focusing on the early events of cancer development could provide new preventative and curative opportunities.

To characterise the degree of advancement of PDAC, practitioners have developed a classification, based on histological stages, and formalised (in their most recent iterations) by two international conferences: the Baltimore consensus of 2004 [70], later revised in the 2015 Baltimore consensus [5]. Cells in the healthy pancreatic ductal epithelium are normally, cuboidal to low-columnar, but may exhibit *KRAS* mutations [66, 70]. In the following stage, lesions called low-grade PanIN (formerly including PanIN-1, PanIN-2 and intermediate-grade dysplasia IPMN and Mucinous Cystic Neoplasm (MCN)) may manifest, with “tall columnar cells with basally located nuclei and abundant supranuclear mucin” [5, 70], *KRAS* activation and telomere shortening [66]. IPMN are neoplasms with varying degrees of “mucin secretion, cystic dilatation, and invasiveness” [70]. Distinguishing morphologically between PanIN and IPMN can prove difficult, and thus a size threshold has been proposed: lesions < 0.5 cm are classified as PanIN whereas > 1 cm are classified as IPMN [5]³ MCN, more infrequent, are cystic lesions producing mucin, often asymptomatic, and usually not connected to the main pancreatic duct. The interested reader may find a detailed review of these precursor lesions in the review of Distler *et al.* for instance [71].

Strikingly, it was recommended that pathologists do not report low-grade PanIN lesions as “they are so common and of no proven clinical significance” as of 2015 [5].

In a further stage, prior to the full-blown invasive carcinoma, lesions may develop into high-grade PanIN (formerly PanIN-3) characterised by “papillary or micropapillary lesions [...], ‘budding off’ of small clusters of epithelial cells into the lumen, and luminal necrosis” along with carcinoma-like phenotype at the cell level without invasion through the basement membrane [5, 70]. Inactivation of *TP53*, *CDKN2A* and/or *SMAD4* may

³In-between, intraductal lesions could be large PanIN or small IPMN [5].

also occur at this stage [66]. These high grade lesions were found to be “clinically important” and are thus reported [5]⁴

Beyond their cytonuclear characteristics, those lesions are architecturally highly three-dimensional, possess varying numbers of branches (for PanIN and IPMN) and may be packed densely in the ducts, but be unconnected between them [7]. Three distinct phenotypes appeared in 3D reconstruction, termed “tubular” (with ductal, branching structures), “lobular” (with grape-like connected locules forming a nodule), and “dilated” (large inflation of the duct connected to thinner ducts) [7].

1.3.4 Stroma formation

In addition to the transformations taking place at the cellular level, PDAC is also characterised by strong desmoplasia, *i.e.* the formation of a dense stroma, notably composed of collagen type I, made by over-active pancreatic stellate cells and fibroblasts (which may represent up to 90% of the tumour’s mass), thereby altering the properties of the ECM [72, 73]. Traditionally, these alterations of the matrix were thought to have solely deleterious effects. The stiffening of the matrix induced by the activity of the stellate cells and fibroblasts was reported to promote tumour progression, and generate a positive feedback loop that encourages fibroblasts to become Cancer-Associated Fibroblasts (CAF) [74]. These CAF can in turn secrete collagen type I and III, fibronectin and proteoglycans and promote Epithelial to Mesenchymal Transition (EMT) and cancer invasiveness [73]. Stellate cells, in inflammatory conditions may also promote tumorigenic capabilities of cancer cells by secreting interleukin-6 (IL-6).

On top of its tumour-promoting activity, the stroma may also be lowering the efficacy of chemotherapy, as the stiffening the matrix may decrease the vascularisation of the tumour and act as a barrier against molecules, therefore impairing the delivery of chemotherapeutic agents [75].

Targeting the stroma to improve drug delivery and efficacy may thus appear as a therapeutic avenue. As an example, Olive *et al.* sought to deplete the tumour-associated stroma by inhibiting the Hedgehog pathway, and found that doing so led to a transient increase in the vascularisation of the tumours, before a return to the *ante*-drug addition status [75].

However, the stroma was also found to have a protective role for the organism, which may explain why the initial successes in stroma-depletion did not translate to successes in clinical trials [76].

Strikingly, in parallel of the reported increase in tumour vascularisation induced by the Hedgehog pathway inhibition [75], experiments found that SHH deletion led to an

⁴I note that on a superficial level, high grade lesions often appear along existing invasive carcinoma, which *de facto* places them in a position where they are “clinically” relevant, compared to low grade lesions that presumably occur earlier in the disease progression. It thus appears that the notion of “clinical relevance” is conflated with the low rate of transformation from low grade to high grade lesion. While understandable from the point of view of limited time and means in health services, omitting to report low grade lesions appears problematic for a disease that suffers from a lack of visible external symptoms in its early forms, and that is essentially incurable when detected late.

increase in tumour aggressiveness, along with an undifferentiated phenotype and increased proliferation [77]. Furthermore, depleting the CAF population had an immunosuppressing effect that decreased survival, and led to tumours with “enhanced hypoxia, epithelial-to-mesenchymal transition, and cancer stem cells” [78].

Carelessly targeting the stroma may thus have unintended and potentially deleterious consequences.

Combined, the issues described in the above sections urgently raise the need for *in vitro* models capable of addressing three objectives: identifying markers for early diagnosis at the onset of the disease, understanding the mechanisms of disease progression and spreads, and allowing for the test of drugs in conditions biologically and morphologically similar to the tumour environment.

1.4 Organoids

The above sections have shown that *in vivo* morphogenesis of tissues, both in healthy and pathological context, encompassed a multitude of highly complex processes, with multiple factors, effectors and regulators.

Going *in vitro* may help to lower this complexity and establish minimal systems exhibiting behaviours of interest, allowing an easier dissection of the mechanisms at play. Two-dimensional cell culture has, for a century, provided tremendous benefits: cultures are easy to maintain compared to living animals, present less ethical challenges, display generally reproducible behaviour, grow homogeneously, and can be accessed and perturbed easily, among many more helpful properties [79, 80].

However, 2D cell culture has been found to induce behaviours and phenotype that differ, sometimes quite starkly, from the *in vivo* systems they purport to model [79, 80, 81].

To bridge this gap between highly complex and expensive *in vivo* systems, and simple - sometimes even simplistic - and cheaper 2D *in vitro* systems, organoids - three-dimensional *in vitro* cellular cultures recapitulating features of a biological tissue of interest - have emerged during the past decade as a powerful *in vitro* platform.

Huch and Knoblich propose the following definition for organoids, adapted here to include the case of cancer organoids:

Definition 1.4.1 *Organoids*: *a 3D structure derived from either pluripotent stem cells (Embryonic Stem Cell (ESC), induced Pluripotent Stem Cell (iPSC)), neonatal or adult stem/progenitor cells, [or cancer cells], in which cells spontaneously self-organise into properly differentiated functional cell types, and which recapitulates at least some function of the organ [or tumour]. [82].*

Through their three-dimensionality, organoids indeed possess a number of advantages over 2D cultures when aiming to mimic *in vivo* behaviour: cells in organoids adopt a more faithful 3D shape and can be in contact with multiple neighbours in all directions, they may not be homogeneously exposed to growth factors and signalling, be in contact with an ECM, differentiate, etc. [79, 80, 81]. This has allowed advances in the

1 Background and state of the art

fields of morphogenesis studies, self-organisation, disease modelling, drug screening or transplantation [15, 82, 83, 84, 85, 86, 87, 88].

Organoids have similarly brought advances for the field of pancreas and pancreatic cancer: allowing the deconstruction of the pancreas development *in vitro* and the expansion of pancreatic progenitors [16], modelling human and mouse ductal pancreatic cancer features from neoplasms to invasive carcinomas [18], recapitulating tumour histology along with the genetic alterations typical of pancreatic cancer [22], and are being used as a platform to develop personalised treatment adapted to the individual patient context [20].

Among organoids, spheroids - sphere-like structures formed by the aggregation of multiple cells or by the self-organised development of a single cell - have proved particularly useful and popular, due to their relative ease of culture, ease of imaging and ease of analysis, combined with their abilities to recapitulate important biological features of the organ or tumour of interest [16, 18, 20, 22].

However, while spheroids are perfectly fitting within the definition of Huch and Knoblich aforementioned, they generally are architecturally very different from the organ or tissue they aim to model, which, we argue, ultimately limit their faithfulness, and the complexity of the dynamics they can exhibit.

This thesis will present the results of efforts to develop more architecturally-faithful pancreatic cancer organoids, that go beyond spheroids, and recapitulate the complex branched morphology of the pancreas and its associated lesions. Importantly, this thesis will focus on the processes that lead to this final morphology, as “the path to the endpoint matters” [82].

2 Branching morphogenesis formation in pancreatic organoids

Preliminary remarks

This chapter is dedicated to the morphogenetic, self-organisation events that lead to the formation of branched structures in PDAC organoids.

These findings led to a publication in *Nature Communications* [8] co-first-authored with Aristeidis “Aris” Papargyriou, under the co-supervision of Prof. Andreas R. Bausch and Prof. Maximilian Reichert, from which are reproduced here part of the results and figures. Aris and I contributed equally on the paper. The project was conceived together with Aris, and Profs. Bausch, Reichert and Prof. Christina Scheel. Maximilian Schuster - under Aris’ supervision - and Giulia Zecchin - under my supervision -, assisted us for part of the experiments and analysis. Prof. Dieter Saur provided the primary cell lines used throughout this thesis. Animal experiments were performed by Dr. Katja Peschke, Prof. Reichert, and histology was performed by Dr. Katja Steiger. Aris, Dr. Rupert Öllinger, Prof. Roland Rad, and Dr. Hans Carlo Maurer should be credited for their work on isolating, sequencing, and analysing the transcriptomic data. The model was developed in tight collaboration with Prof. Edouard Hannezo.

2.1 Culturing three-dimensional PDAC organoids - Observations

Matrigel and collagen cultures

To study PDAC in vitro, we used primary tumour cells from a KC mouse model of pancreatic cancer with the genetically engineered mutation $Ptfla^{Cre/+};Kras^{G12D/+}$ [89], cultured in a medium composed of Dulbecco’s Modified Eagle Medium (DMEM) high-glucose, 10% v:v Fetal Bovine Serum (FBS), and optionally 1% v:v Penicillin/Streptomycin (hereafter the “culture medium”).

In order to generate three-dimensional structures, we embedded cells in an extracellular matrix (ECM), the choice of which proved to be critical in determining the type of structures that emerged.

Matrigel, a mixture of ECM proteins obtained from crushed tumours of Engelbreth-Holm-Swarm mouse sarcoma has been one of the long-standing standards matrices for three-dimensional cell culture [90].

Previous studies using pancreatic cells have evidenced the formation of three-dimensional sphere-shaped structures called spheroids, upon embedding of the cells in Matrigel,

whether with murine embryonic pancreatic progenitor or human foetal pancreata, [16, 91, 92, 93].

Unsurprisingly, embedding primary tumour cells from a KC mouse model (9591 cell line) into Matrigel (Growth factor-reduced Matrigel, 356230 Corning) domes, led to the formation of spheroids, as was the case in other studies with pancreas cells [16, 93].

Compared to the morphology of the exocrine pancreas -in which PDAC develops- (Fig. 0.2), or to the morphology of its precancerous lesions (Fig. 0.3, and [7] for 3D reconstructions), spheroids are however lacking important architectural features: a branched structure, the presence of bud-like tips, and a tubular lumen connecting the branches, being among the most prominent ones.

In the hope of generating structures more architecturally faithful to the pancreas and its lesions, we adapted a protocol from studies performed on mammary organoids [86, 94] (Fig. 2.1). Briefly, single murine PDAC cells were embedded inside a gel of collagen type I (rat tail, 354236 Corning) which was detached from the bottom of the culture dish upon polymerisation, and allowed to float in culture medium. This protocol is further described in chapter 5 - Materials and Methods.

Crucially, culturing PDAC cells in collagen led to the apparition of three-dimensional structures bearing key morphological features missing in spheroids, and reminiscent of the structures of pre-cancerous pancreatic lesions such as PanIN, IPMN or MCN. Collagen-grown organoids displayed a highly three-dimensional, branched architecture, displaying terminal end buds and a single seamless lumen connecting the network together, strikingly distinct from Matrigel-grown spheroids (Fig. 2.2).

Within 13 days of culture, Matrigel-grown organoids grew as spheroids of about 80 μm in diameters, whereas collagen-grown organoids developed branched structures that could reach around 2000 μm in extent, indicating starkly different processes of growth depending on the ECM (Fig. 2.2).

Furthermore, we found that those branched organoids appeared could emerge in other types of pancreatic cancer lines such as in a $\text{Pdx1}^{\text{Cre}/+};\text{Kras}^{\text{G12D}/+};\text{TP53}^{\text{fl}/\text{fl}}$ model (the so-called KPC mouse model) but that healthy wild type adult pancreatic ductal cells did not seem to exhibit this branching ability (Fig. 2.3).

Given the simplicity of the culture medium (DMEM and FBS), and the absence of additional growth factors, we set out to investigate the self-organising dynamics that led to the spontaneous emergence of these highly complex structures, starting from the single cell stage (Fig.2.3).

2.2 Phases of development

Hereafter, and unless explicitly mentioned otherwise, we focus on organoids grown from a cell line named “9591”, isolated from the tumour of a $\text{Ptf1a}^{\text{Cre}/+};\text{Kras}^{\text{G12D}/+}$ mouse.

To shed light on the processes of development in space and time, we performed extensive live imaging of growing organoids using bright field and confocal microscopy. Investigating patterns of cell motion, cell-ECM interactions, and protein expression over the course of 13 days revealed marked differences, which allowed us to define four phases

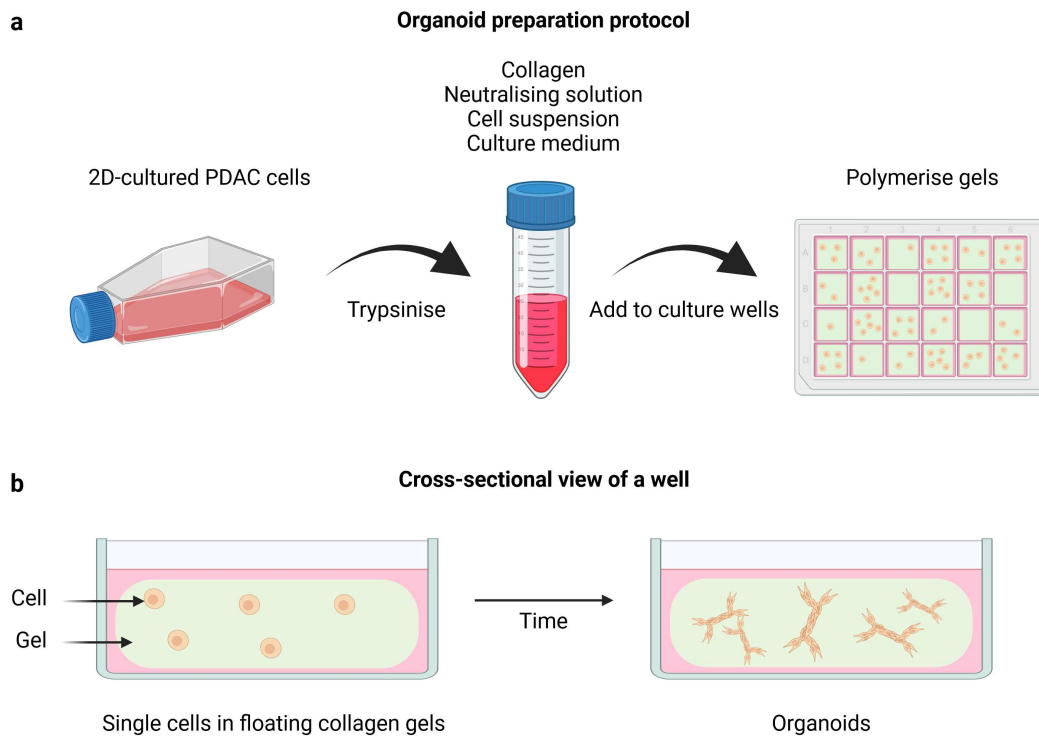


Figure 2.1: **Schematic of the floating collagen gel assay preparation.** **a** Organoid preparation protocol. Briefly, PDAC cells are first cultured in 2D, detached with trypsin at confluence, and then mixed with collagen, neutralisation solution and culture medium, before being plated in culture wells, where the gels polymerize and are then detached. **b** Cross-sectional view of a well, with single cells embedded in floating gels, giving rise to organoids over time. Figure created with BioRender.

of development, that we named the “Onset”, “Extension”, “Thickening”, and “Lumen formation” phases¹ (Fig. 2.5).

In the following subsections, we will provide an overview of the characteristic patterns observed for each of the developmental phases, before focusing on the branching morphogenesis process occurring in the Onset and Extension phases. Chapter 3 will focus on the Thickening phase, while Chapter 4 will focus on the Lumen Formation phase.

Figure 2.10 recapitulates the observed patterns in cell motion, cell-ECM interaction, and cell proliferation for each phase.

¹As the identified development phases were named after the most prominent architectural changes occurring at that time point, we have chosen to capitalise the phase names to distinguish them from the events. Thus, for the remainder of this thesis “Onset”, “Extension”, “Thickening”, and “Lumen Formation” all refer to the organoid development phases, whereas “onset”, “extension”, “thickening”, and “lumen formation” refer to the architectural changes in the general acceptance of the terms.

2 Branching morphogenesis formation in pancreatic organoids

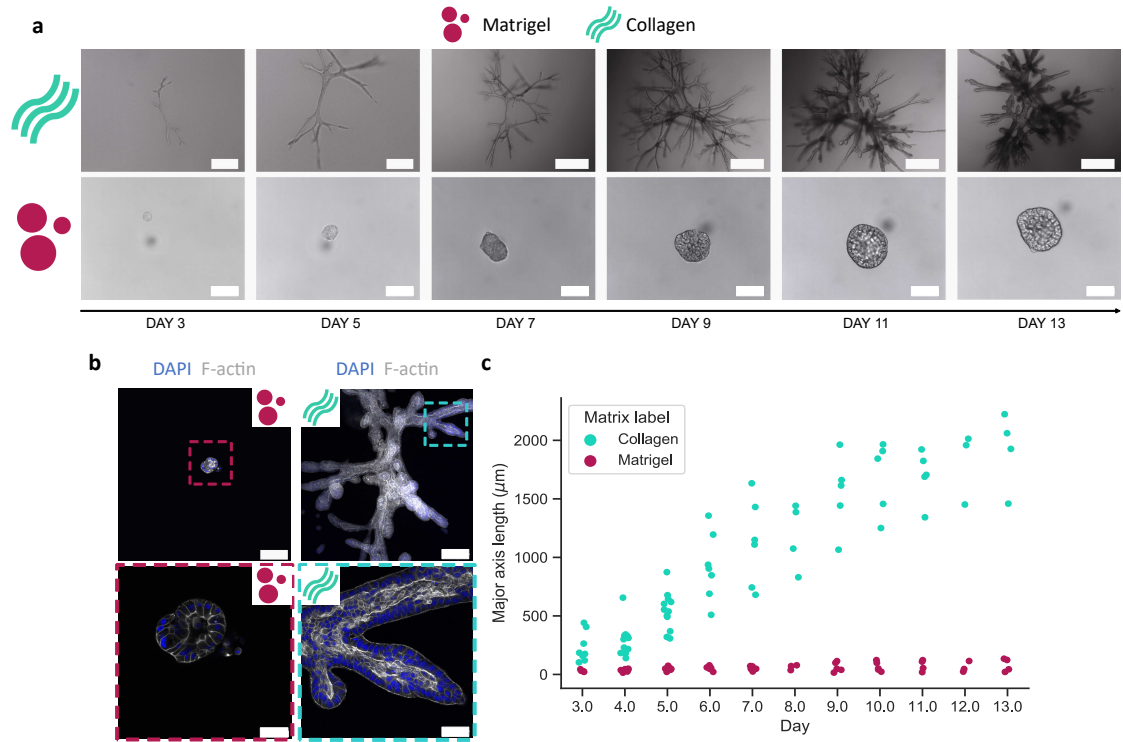


Figure 2.2: **Matrigel- and collagen-grown organoids exhibit strikingly different morphologies.** **a** Bright field snapshots of collagen- (top, $n = 71$ organoids) and Matrigel-grown organoids (bottom, $n = 54$ organoids) at various time points. Scale bars: $200 \mu\text{m}$ top, $50 \mu\text{m}$ bottom. **b** Matrigel- (left column) and collagen-grown (right column) Day 13 organoids stained against DAPI (blue) and F-actin (white). Zoomed insets marked by the dashed boxes are shown in the bottom row. $n = 3$ individual experiments for each. Scale bars, top from left to right: $200 \mu\text{m}$ for the first two pictures, $500 \mu\text{m}$ for the rest; bottom: $100 \mu\text{m}$. **c** Major axis length evolution over time of individual collagen- (cyan, $n = 71$ organoids) and Matrigel-grown (magenta, $n = 54$) organoids. In collaboration with Aristeidis Papargyriou, reproduced and adapted from [8].

We note that while the number of days elapsed since seeding provides a strong indication for the development phase of organoids, the precise timing might vary between samples, owing to experimental heterogeneity that we discuss further in section 2.1. The general hallmarks of each described developmental phases are however present in every organoids, despite the apparent morphological diversity of end point phenotypes at Day 13 (Fig. 2.6)

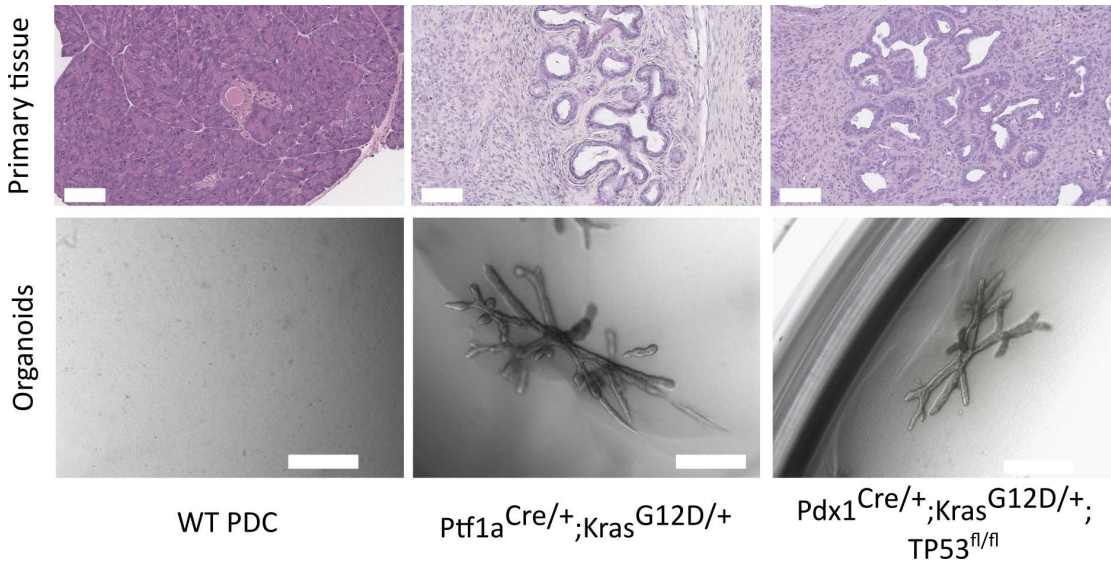


Figure 2.3: **Comparing healthy and cancerous structures, in primary tissues and in organoids.** Top, from left to right: haematoxylin and eosin staining of primary tissue sections from a healthy pancreas, a $Ptf1a^{Cre/+};Kras^{G12D/+}$ tumour, and a $Pdx1^{Cre/+};Kras^{G12D/+};TP53^{fl/fl}$ tumour ($n = 3$ technical replicates). Bottom from left to right: bright field images of representative organoids at day 13, grown in collagen from wild type pancreatic ductal cells (WT PDC), $Ptf1a^{Cre/+};Kras^{G12D/+}$ cells, and $Pdx1^{Cre/+};Kras^{G12D/+};TP53^{fl/fl}$ cells, all cultured in cell culture medium (see Methods) ($n = 3$ individual experiments). Scale bars: top, 100 μm ; bottom, 500 μm . Reproduced and adapted from [8]. Organoids by Aristeidis Papargyriou. Histology by Prof. Katja Steiger.

2.2.1 Motion

The motion of cells in organoids is one of the more readily identifiable feature that exhibits drastic changes as the structures develop, which prompted the segmentation of the development process into phases, each bearing as a signature a particular pattern of cell motility.

To study it, we use live microscopy, combining bright field imaging and the confocal imaging of labelled-nuclei.

Onset

After seeding in the collagen matrix, the initial single cell undergoes several rounds of proliferation, breaking symmetry and forming an elongated structure with a principal axis of elongation. Cells in this phase are characterised by a back-and-forth motion within the organoids, forming branches one- to two-cells wide, that intermittently elongate and retract in the surrounding collagen (Fig. 2.10a).

2 Branching morphogenesis formation in pancreatic organoids

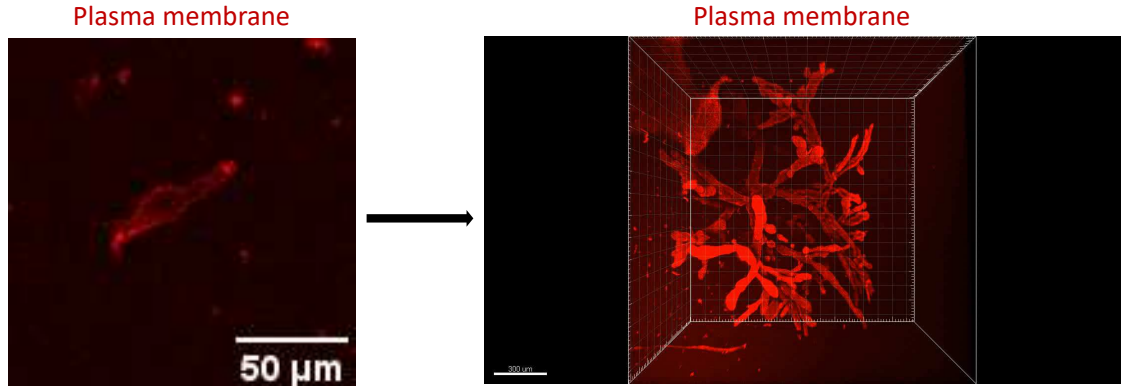


Figure 2.4: **From a single cell to a complex branched structure.** Representative picture of an initial PDAC 9591 cell upon seeding in collagen (left) that gives rise to a highly branched organoid (right) after 13 days of culture. Plasma membrane labelled in red using CellMask. The right picture is a 3D reconstruction of confocal slices.

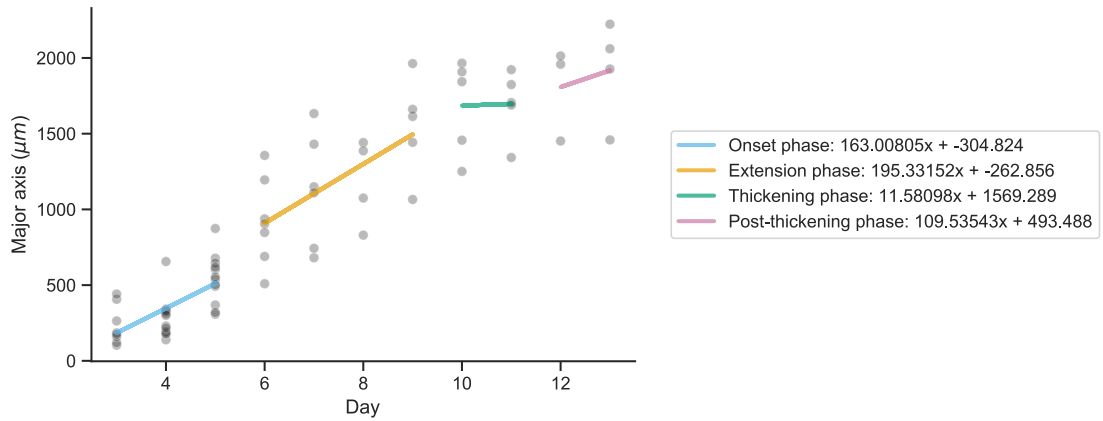


Figure 2.5: **Major axis length evolution of collagen-grown organoids over time** with linear fits highlighting the different phases (blue: Onset, orange: Extension, green: Thickening, pink: Lumen Formation; $n = 71$ organoids). Reproduced and adapted from [8].

Extension

Around day 7, the back and forth motion of branches is replaced by a highly directional invasive motion, with cells mostly moving from the proximal regions of the branches to the distal regions (Fig. 2.10 a, a', 2.11). Cells at the tip of branches display a spiky protrusion as they invade the matrix at a constant speed (Fig. 2.11c), leading to an increase in organoids' main axis length of about $195 \mu\text{m}$ per day. Furthermore, the invasion speeds across the organoid appeared similar (Fig. 2.11b).

We found that branching events occurred following tip cell division in more than 90%

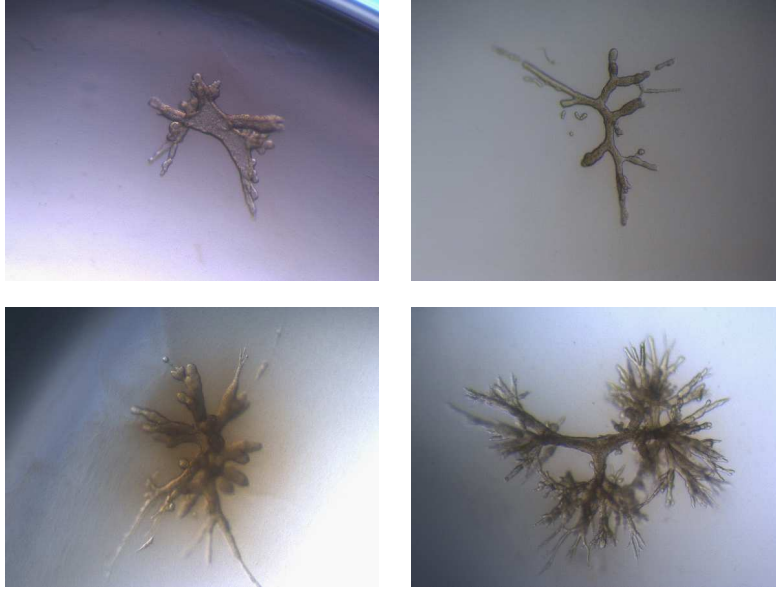


Figure 2.6: **Diversity of organoid morphologies at Day 13.** All organoids were cultured in the same well, under the same culture conditions.

of the cases (Fig. 2.12).

Thickening

Around 9 days post-seeding, we noted an arrest in the extension of branches, their switch from a spiky phenotype at the tip to a rounded one, their thickening leading to a marked increase in width, and a strong contraction of the organoid inducing a deformation in the surrounding collagen (Fig. 2.10), in stark contrast to the Extension phase.

As the branches retract their spiky protrusions and thicken, we observed the formation of terminal end bud-like structures at their tips.

Lumen formation

Following the Thickening phase, we observed that organoids transitioned from a “solid rod” structure to a hollow one, by forming microlumens at multiple locations, eventually giving rise to a single seamless lumen connecting all branches, as indicated by the strong F-actin apical signal (Fig. 2.2b).

2.2.2 Matrix interactions

We observed the organoids deform the surrounding collagen as they grew in the bright field images. To further quantify the interactions between cells and their surrounding matrix we embedded fluorescent beads in the collagen before polymerisation (see Methods), and tracked the position of beads in cones in front branch tips. Fig. 2.10b shows

2 Branching morphogenesis formation in pancreatic organoids

how each developmental phase is characterised by a distinct pattern of cell-ECM interaction. During the Onset phase, branch extending and retracting generate a global contractile motion around the organoid. In contrast, branches invading the matrix during the Extension phase generate very little deformation, suggesting that migration at this stage may involve a different process. In the Thickening phase, we evidenced a large contraction field surrounding the organoid, along with the retraction of branches and their widening. Finally, branches appeared static during the Lumen Formation phase, with observable deformation due to the organoid increasing their volume upon lumen formation.

To investigate the effect of these deformations on the matrix, we used reflection microscopy - also known as second harmonic generation (SHG) - to image the collagen structure [95, 96].

We observed that branches were able to remodel the randomly oriented collagen fibres in the matrix into aligned fibre cones visible in front of the tips (Fig. 2.7a-b, Fig. 2.8a). We also evidenced an accumulation of collagen surrounding the organoids in a “cage-like structure”.

Cells were found to express proteins such as $\alpha 6$ integrin or laminin on their basal surface, mediating the interactions between branches and collagen (Fig. 2.7c-d).

Crucially, we found that cells plastically remodelled their environment when grown in collagen. Indeed, by exposing organoids to Triton X-100 to degrade cell membranes and dissociate the organoids, thus abolishing the active forces exerted on the matrix, we observed that the “cage-like” collagen structures were preserved (Fig. 2.8c-d).

Our observation joins other studies in highlighting the key role of mechanical plasticity in branching morphogenesis [86, 87, 97].

While mechanical interactions appear to be the dominant remodelling mechanism in the Thickening phase (and to some extent in the Onset phase), we evidenced that, in the Extension phase, organoids primarily digested the matrix through the use of Matrix metalloproteinase (MMP) (Fig. 2.9a), known to play a major role in cancer invasion and metastasis [98, 99] and thus explaining the weak deformation field.

Noting the decrease in MMP levels between day 7 and 13 (Fig. 2.9), it remains at this stage unclear what governs the expression of MMP.

Proliferation patterns

We assessed the proliferation capabilities of organoids over their growth using immunostainings against Ki-67 (a proliferation marker) and DAPI at different developmental stages (Fig. 2.10c-e). We quantified the proliferative fraction as the ratio being Ki-67-positive cells over the DAPI-stained cells. At the Onset stage, we observed that every cell was capable of proliferation. As organoids progressed towards the Extension, Thickening and Lumen Formation phases however, we noted a decrease of the proliferation fraction, with cells in the core of the organoids becoming Ki-67-negative, and proliferation persisting in tips cells (Fig. 2.10c,e)

This change in proliferation pattern was apparent in the evolution of the cell number, exhibiting an exponential growth within the first five days of growth, before slowing

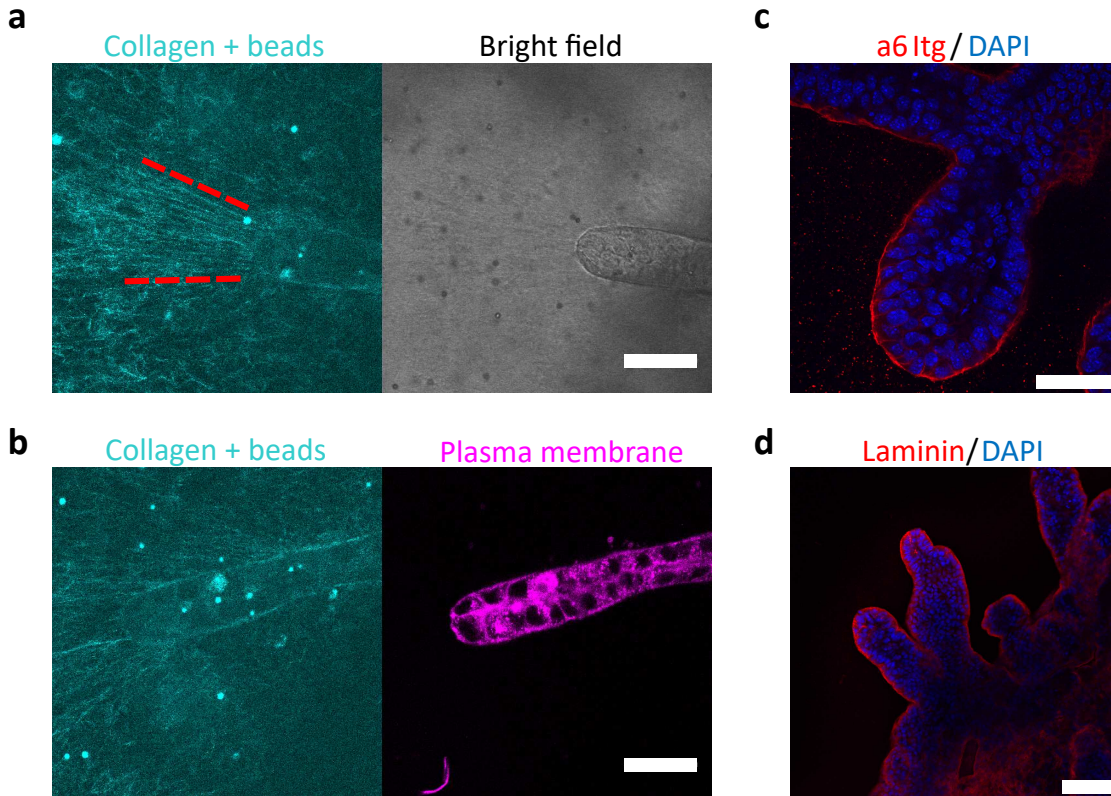


Figure 2.7: **Organoids interact with the ECM and remodel it.** **a** Collagen fibres visualized with reflection microscopy (cyan), in front of a thickening branch at Day 10 ($n = 2$ replicates). The branch is pulling on the fibres in front of it, aligning them in a cone, outlined by the red-dashed lines. **b** Collagen fibres visualized with reflection microscopy (cyan) around the branch of an organoid at Day 10 (plasma membrane stained in magenta, $n = 2$ replicates). **c** Staining of DAPI (blue) and $\alpha 6$ integrins (red) a mediator of cell-ECM adhesion. **d** Staining of DAPI (blue) and Laminin (red) a major component of the basal lamina. For **c-d**: organoids Day 13, $n = 3$ individual experiments. Scale bars: **a-c** 50 μm , **d** 100 μm . Reproduced and adapted from [8].

down and plateauing in the latter stages (Fig. 2.10d), which is in turn reflected in the evolution of organoids' major axis length (Fig. 2.2c).

Through immunostainings against Ki-67, we observed that every cell in the organoid at the Onset stage appeared capable of proliferation, with the cell number increasing exponentially within the five days following seeding (Fig. 2.10c-e).

2 Branching morphogenesis formation in pancreatic organoids

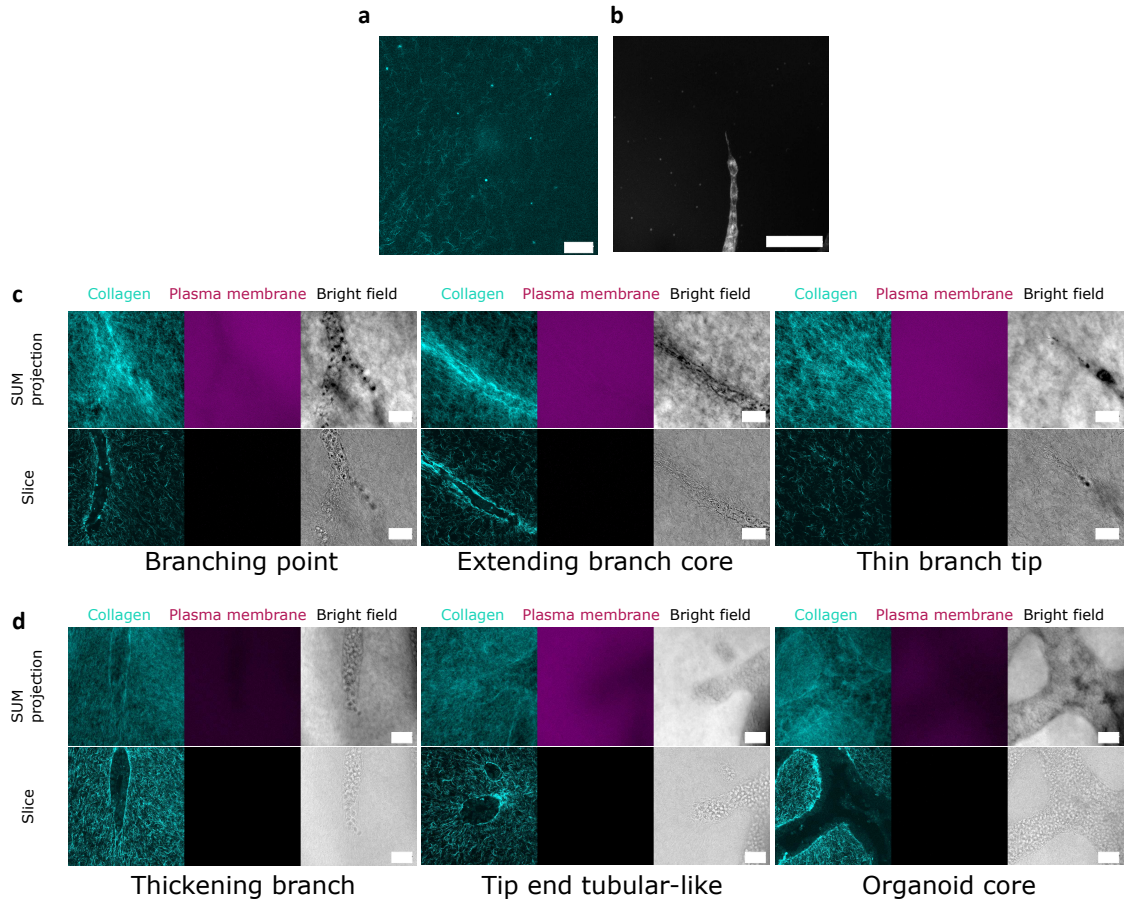


Figure 2.8: Organoids plastically remodel their environment. **a** Collagen fibres far away from organoids, visualized with reflection microscopy ($n = 3$ organoids). The fibres display no particular alignment far away from organoids. Confocal slice. **b** Plasma membrane staining of an invasive protrusion at D7 ($n = 13$ organoids). Summed slices projection. **c, d** Organoids were treated at D8 (**c**, $n = 3$ organoids) or D11 (**d**, $n = 3$ organoids) with Triton-X 100 and fixed. Triton-X 100 degrades the cell membrane and provoke the dissociation of organoids. Organoids are stained with CellMask, a plasma membrane marker (magenta), to ensure that the membrane has been properly washed away after the Triton-X treatment. Collagen fibres are visualized with reflection microscopy (cyan). The architecture of the collagen surrounding the organoids is preserved, indicating a plastic deformation of the ECM. Summed slices projections and single confocal slices are shown. Scale bars (a), (c), (d): 50 μm ; in (b): 100 μm . Reproduced and adapted from [8].

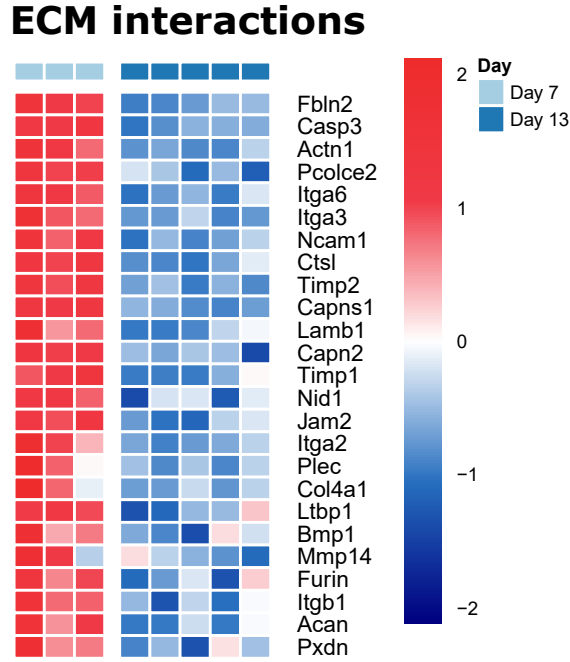


Figure 2.9: **Cell-ECM interactions.** **a** Up- and downregulation heatmap of ECM interactions-related genes (log₂ transformed) comparing collagen-grown organoids at day 7 and 13. **b** Time-lapse of an organoid branch upon 10 μ M batimastat addition at day 8. MMP-inhibition prevents branch elongation, indicated by black arrows. Reproduced and adapted from [8].

2.3 A minimal biophysical model for the early phases of development

2.3.1 Rationale

The existence of different developmental phases, each characterised by varying patterns in cell motion and proliferation, raises the question of the existence of control mechanisms directing the transition between phases.

We aimed to probe whether a limited set of biophysical principles could describe quantitatively the emergence of branched structures occurring in the Onset, Extension and the early Thickening phase.

In collaboration with Prof. Edouard Hannezo of IST Austria, we therefore developed a minimal analytical model [8], that we reproduce in part here, with details fully available in the Supplementary Note of our publication [8].

We show hereafter that modelling serves a dual role in our study. It first provides quantitative agreement with our experiments in the unperturbed case, underscoring the power of a minimal set of fundamental parameters in capturing the emergence of self-organised structures. The transition between different phases of growth, notably seen through the change in proliferation capabilities, emerges spontaneously in the model.

2 Branching morphogenesis formation in pancreatic organoids

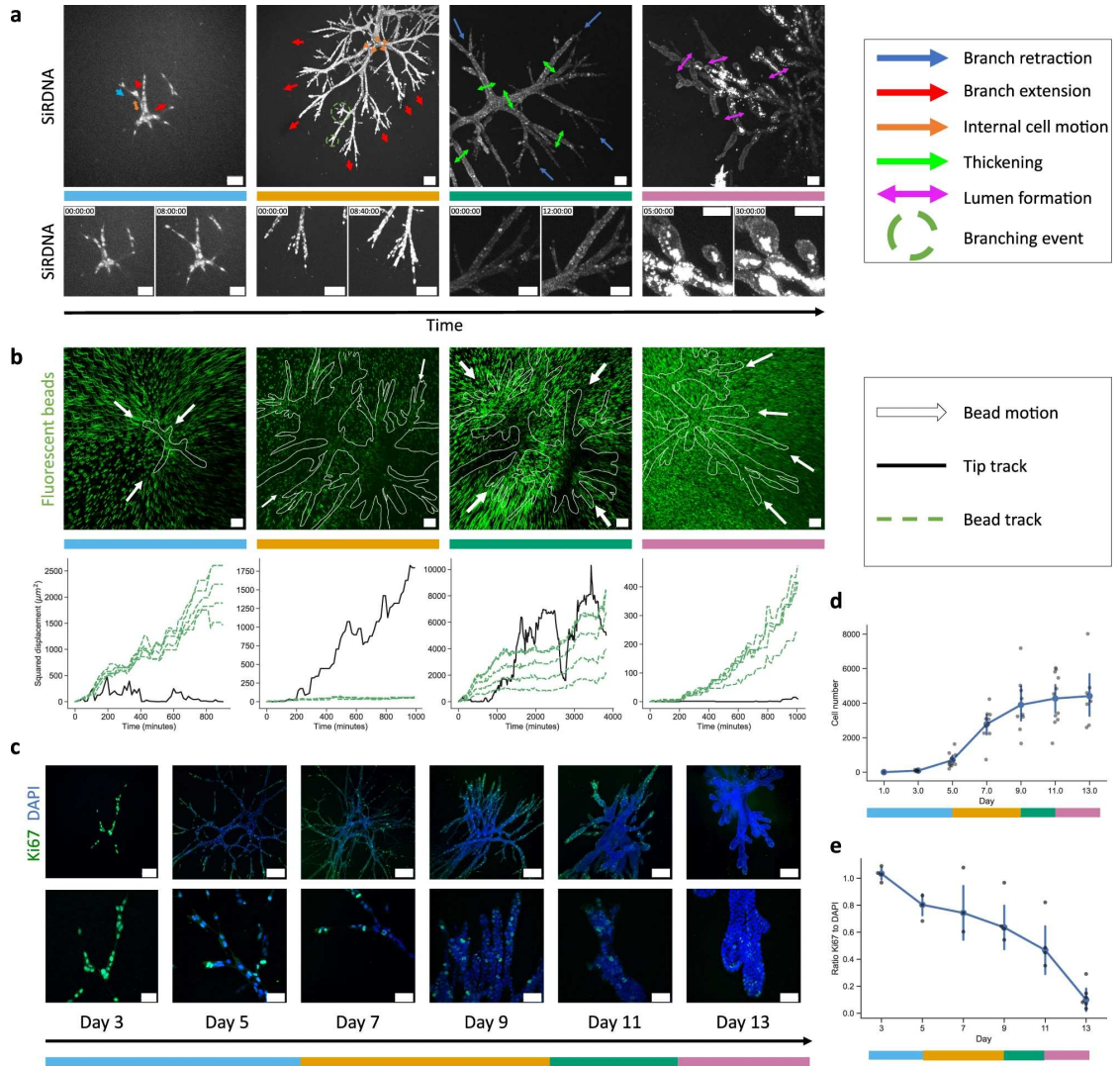


Figure 2.10: *Caption on the next page.*

Furthermore, stochasticity in the model is sufficient to recapitulate the emergence of different organoid phenotypes, and their variability.

In addition, the model is able to make qualitative and semi-quantitative predictions on the influence of chemical perturbations on the branching process².

The model therefore serves as a powerful tool for abstraction, yielding accurate predictions on organoids dynamics without having to consider the exact microscopic details of the mechanisms at play. This property is particularly important when dealing with building blocks of organoids structures such as cell motion, cell-ECM interactions, and

²“Semi”-quantitative, as perturbations of biological processes through chemical means are often accompanied by off-targets effects that may not directly be accounted by the “simulated” perturbations.

Figure 2.10: **Summarised patterns of organoids' development phases.** Development phases are denoted by colour bars with the following color code: blue - onset, orange - extension, green - thickening, pink - lumen formation. Organoids shown here are grown in collagen. **a** Cellular motion patterns observed with live confocal imaging for each development phase ($n = 66$ organoids). Cell nuclei are stained with SiRDNA (white). Scale bars: $100 \mu\text{m}$. From left to right: Day 4 SUM projection, and Day 7, Day 10, Day 13 maximum projections. **b** Top, time-projections of fluorescent beads (green, maximum projections) trajectories at different time points, indicating the deformation field around the organoids. Organoids are outlined in white and white arrows denote the direction of bead motion. From left to right: Day 4-5, Day 7-8, Day 8-9, Day 13-14. Scale bars: $100 \mu\text{m}$. Bottom, corresponding representative squared displacement of a branch tip (solid black) and the motion of beads (dashed green) in front of it, for each development phase. **c** Immunostainings of Ki67 (green) and DAPI staining (blue) in organoids at different time points. Top scale bars, from left to right: $80 \mu\text{m}$ first picture, $200 \mu\text{m}$ second picture, $200 \mu\text{m}$ for the rest. Bottom (zoom-in of the top row images) scale bars: $50 \mu\text{m}$. Confocal slices. **d** Cell number evolution in organoids, estimated based on maximum projections of DAPI stainings ($n = 56$ organoids). Blue line indicates the mean tendency. Error bars: 95% confidence interval (CI). **e** Ratio of Ki67- over DAPI-positive cells ($n = 24$ organoids). Blue line indicates the median. Error bars: standard deviation. Reproduced from [8].

protein expression, which are highly complex, taken both individually and together.

2.3.2 Describing the model

The model considers three fundamental and general processes of branching morphogenesis: proliferation - mediated by cell division at a rate k_d -, branching - triggered by tip cells at a rate k_b -, and invasion - through cells actively migrating at a speed v_0 - (Fig. 2.16a). We describe the morphometrics of branches at time t through their average width $w(t)$, their average length $l(t)$, and we denote $N_c(t)$ and $N_b(t)$ respectively the total number of cells and branches in the organoids.

Two equations govern the system: a mass conservation equation and a force balance equation that accounts for potential feedbacks between different parameters.

Intuitively, this model can be interpreted as a competition between the proliferation process and the elongation and branching processes. Following mass conservation, at a given k_d , increasing v_0 and k_b will favour thin branches, whereas lowering v_0 and k_b will lead to shorter and thicker branches.

The force balance at the tip cell of a branch generally reads:

2 Branching morphogenesis formation in pancreatic organoids

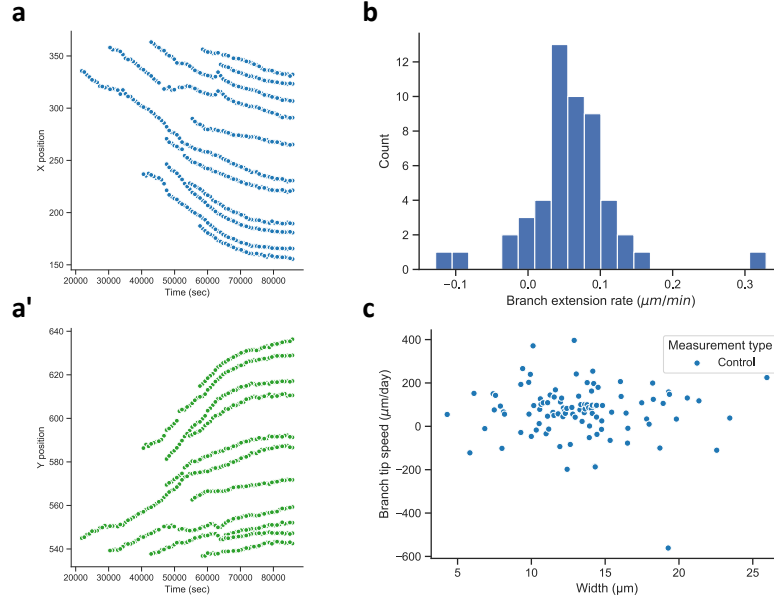


Figure 2.11: **Migration directionality and branching events during the Extension phase.** **a** X (blue) and **a'** Y (green) positions for cells in an extending branch, representative of the dominant extension behaviour between day 7 and 10. **b** Mean branch extension rate distribution between day 7 and 10 ($n = 51$ branches). **c** Instantaneous branch tip speed versus branch width for organoids between day 7 and 10 in the Extension phase. No correlation between the tip speed and the tip width can be observed ($n = 103$ points, $N = 3$ organoids). Reproduced and adapted from [8].

$$\zeta L'(t) = f_0 + \chi \rho(t) \quad (2.1)$$

with ζ a friction term, $L'(t)$ the change over time of the branch length, f_0 the active migration force (active cell migration occurring at a velocity $v = f_0/\zeta$), χ a compressibility, and $\rho(t) = N(t)/L(t)$ the 1D cell density ($\chi\rho(t)$ denoting the compressive forces from the bulk of the follower cells).

Feedback is introduced in the equation to account for the observed decrease in proliferation capabilities evidence by the Ki-67 stainings as organoids grew in size. We indeed evidenced a strong negative relationship between the volume growth rate of branches (taken as a proxy for proliferation) and their width (Fig. 2.13).

The exact origin of this decrease remains for now unclear in PDAC organoids. Studies on Madin-Derby canine kidney (MDCK) monolayers and tumour spheroids have proposed that such decrease in proliferation could be linked to a negative mechanical feedback [100, 101, 102], and contact-inhibition of proliferation [103, 104, 105]. However, numerous other mechanisms such a diffusion-limited growth or inhibitory short range signals have also been observed to play a role in other branching systems [39, 106, 107].

2.3 A minimal biophysical model for the early phases of development

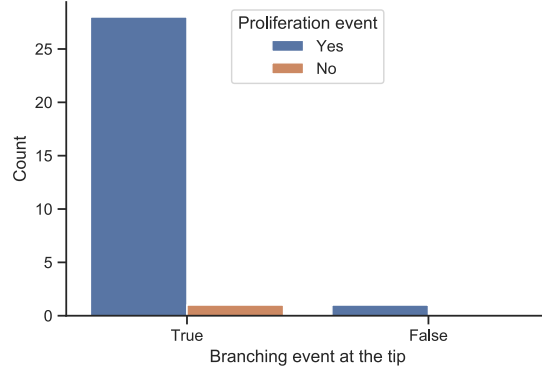


Figure 2.12: **Correlation between branching and proliferation events** in the leading 6 cells of a branch tip between day 7 and 10. True-Yes: branching event was preceded by a proliferation event. True-No: branching event occurred without being preceded by a proliferation event. False- Yes: proliferation event occurred, but a branching event did not follow (n = 30 events, N = 4 organoids). Reproduced and adapted from [8].

We therefore described the negative feedback on proliferation in a mechanism-agnostic way such that:

$$k_d = k_d^0 \left(1 - \frac{w}{w_0}\right) \quad (2.2)$$

with w_0 the branch width at which proliferation is fully abolished, and k_d^0 the maximal division rate.

We observed that the invasion speed v_0 remained constant during the Extension phase (Fig. 2.11b-c), resulting in the following equations for the dynamics:

$$\begin{cases} \frac{d(N_b l)}{dt} &= v_0 e^{k_b t} \\ \frac{dN_c}{dt} &= k_d^0 \left(1 - \frac{w}{w_0}\right) N_c \end{cases} \quad (2.3)$$

where the first equation relates the increase in total length of the organoids with the invasion speed and the branching rate, and where the second equation describes the increase in cell number, slowing down due to the negative linear feedback evidenced between width and growth rate. Upon simulation of the model, two phases appear: proliferation is first exponential with $k_d \approx k_d^0$ as branches are initially kept thin by elongation and branching (so the negative feedback is minimal) then proliferation becomes dominant over elongation and branching, effectively leading to a plateau in thickness where $w \approx w_0(1 - k_b/k_d)$ and the proliferation rate decreasing to the increased feedback.

We note that in this model, branching is key to the organoid ability to expand.

Indeed, in the case of a single branch invading the matrix, elongation is linear in time with v_0 - dominating at short timescales -, whereas proliferation is exponential in time

- dominating at long timescales -. In the case of 2D cell monolayers on a flat substrate or in the case of 3D spheroids in Matrigel, the edge’s geometry is similarly constraining the growth to be linear in time, leading the competing proliferation term to catch up quickly, limiting the duration of the uninhibited exponential growth phase and resulting in a drop of the proliferation capabilities. Intuitively, those systems are becoming “thick too quickly”.

In contrast, a system where branching is possible now has a leading edge growing exponentially, which allows the elongation processes to compete longer with proliferation (which eventually catches up as long as $k_b < k_d$).

This argument could explain why collagen-grown branched organoids are able to reach sizes an order of magnitude superior to the sizes of Matrigel-grown spheroids.

2.3.3 Comparing model predictions to experimental results

We then sought to compare the model’s output with the experimentally-observed time course of organoid growth from an original single cell, to the end of the Extension phase. For simulations, we implemented a spatial version of the model, described in the Supplementary Theory Note of [8].

Using the acquired live imaging data between day 7 and 9, we were able to determine the following parameters for the model.

We found that the tip invasion speed remained constant during the extension phase at $v_0 \approx 80 \mu\text{m}/\text{day}$, independently of branch width (Fig. 2.11b-c), and that tip cells could occasionally separate from the branch, and continue migrating through the collagen at a similar speed. To estimate the proliferation rate and the maximum width at which proliferation was abolished, we performed a linear fit on the evolution of the normalised volumetric growth rate as a function of width for branches, and found $k_d = 3.9d^{-1}$ and $w_0 = 25 \mu\text{m}$.

To determine the branching rate k_b , two methods were considered. The first one relies on the estimation of the average branch length between day 7 and 9 (Fig. 2.14) found to be $l_0 \approx 150 \mu\text{m}$, which, with the assumption of a constant invasion speed $v_0 = 80 \mu\text{m}/\text{day}$, yields $k_b \approx v_0/l_0 \approx 0.55d^{-1}$. One can also derive k_b from the increase in branch number obtained from static measurement at different timepoints, where the best fit value, using a single exponential growth rate, yields $k_b = 0.75d^{-1}$ (Fig. 2.15). We note that the value of k_b affects the growth of organoids after their initial phase of uninhibited proliferation (further shown in the simulations Fig. 2.17), but that the differences are minimal within this range. For the simulation, we chose $k_b = 0.75d^{-1}$.

The simulation is initialised as a single cell, making up a single branch, of width $w = 5 \mu\text{m}$ and length $l = 20 \mu\text{m}$, corresponding to the average dimensions of a PDAC cell upon seeding. Each new branch is set to appear with a nascent width of $w = 5 \mu\text{m}$.

We report overall an excellent agreement between the predictions of our model, shown in Figure 2.16, both qualitatively (Fig. 2.16b, g) and quantitatively (Fig. 2.16c-f). Importantly, despite extracting parameters from data acquired between Day 7 and 9, our model was able to recapitulate the entire timeline of organoid development from the seeding point to the early Thickening phase.

2.3 A minimal biophysical model for the early phases of development

We first found that the model recapitulated the evolution of the average cell number in organoids, with the predicted initial phase of uninhibited exponential growth, followed by a reduction in proliferation, visible (Fig. 2.16c).

The predicted number of branches closely matched the observed experimental values, following an exponential growth over time (Fig. 2.16e). Importantly, the model was also capable of recapitulating the experimental variability in the number of branches between organoids, with the standard deviation growing exponentially in time and with the same order of magnitude as the average number of branches, a hallmark of a stochastic (Poisson) branching process (Fig. 2.16f-g). This suggests that the stochasticity of the branching process is enough to account for a large part of the differences observed in organoid sizes and morphologies (Fig. 2.6), without requiring organoids to exhibit intrinsically different branching rates. This does not, however, rule out the existence of potential inter-organoids biological differences, which should compound this variability, and may in turn contribute to further biomechanical feedback.

Lastly, the model predicts that the average width of branches should follow an initial phase of growth in the early days of organoids development, before plateauing due to the negative feedback on proliferation in later stages. Moreover, the model predicts that the average width should differ between “non-terminal branches” (*i.e.* segments of branches between two consecutive branching points), and “terminal branches” (*i.e.* segments taken between the last branching point and the tip of a branch). Terminal branches should exhibit a width plateau at lower values than the non-terminal branches, as the former are still subject to elongation which favours thinning. Both of those predictions were found to be in close qualitative and quantitative agreement with the experimental data (Fig. 2.16d), further highlighting the power of the model. The apparent deviation in the later stages between the terminal branch width predicted by the model and the experimental data can be attributed to the emergence of other budding processes, that are further discussed in Chapter 3.

2.3.4 Predicting the results of perturbations

Having noted the overall agreement between our model and experimental results under standard culture conditions, we sought to further use our model to predict the effect of perturbations in organoid growth, introduced *via* various chemicals and discussed in details in the following section 2.4.

We can first simulate the effects of impairing migration, something performed experimentally through the use of batimastat - a broad-spectrum MMP inhibitor -, by altering the value of the invasion speed v_0 . The model predicts that for $v_0 \approx 0$ and proliferation remaining active, the organoids should thicken and tend toward w_0 at long time scales, as the branch elongation normally counteracting volumetric growth is abolished (Fig. 2.17b, e, Fig. 2.18b, e-f).

Conversely, impairing proliferation by decreasing k_b , experimentally feasible using aphidicolin - a proliferation-inhibiting drug -, while keeping migration possible, should lead to a thinning of the organoids, as no new cells are produced to sustain volumetric growth. The model further predicts that newly formed branches should be particularly

2 Branching morphogenesis formation in pancreatic organoids

susceptible to breaking events, as the linear elongation process will dominate over the low proliferation induced by the low cell number, leading to the thinning of the branches and the creation of rupture points (Fig. 2.17d, h, Fig. 2.18a, e-f).

Our model thus exhibits very good agreement with experimental results in both unperturbed and perturbed conditions, and reveals that a minimal set of biophysical rules is enough to recapitulate the formation of the complex branched structures that appear during the early stage of organoid morphogenesis, while remaining agnostic as to the particular molecular pathway involved. Future perturbation experiments could then be checked against the predictive power of the model, as the resulting morphology of the organoid bears the signature of the altered processes.

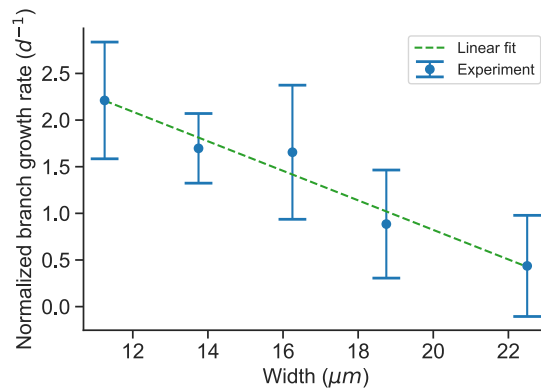


Figure 2.13: **Evolution of the normalised volumetric growth rate per day of branches according to their width** ($n = 85$ points, $N = 3$ organoids). Reproduced and adapted from [8].

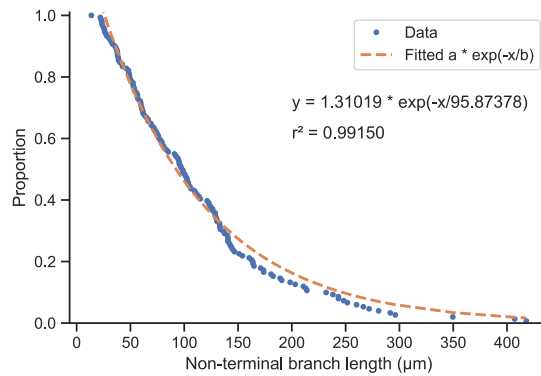


Figure 2.14: **Complementary empirical cumulative distribution function of non-terminal branch lengths** for organoids at day 7-10 (blue dots, $n = 151$ branches, $N = 4$ organoids) and fitted curve for an exponential distribution (dashed orange line).

2.3 A minimal biophysical model for the early phases of development

Manual branch counting - Median estimator in solid line

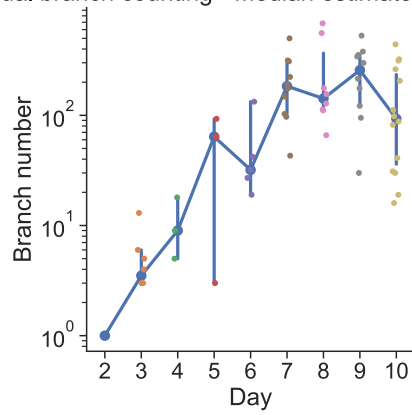


Figure 2.15: **Evolution of the branch number per organoid over time** Median estimator is shown in solid blue line. Error bars: 95% confidence interval (N= 65 organoids).

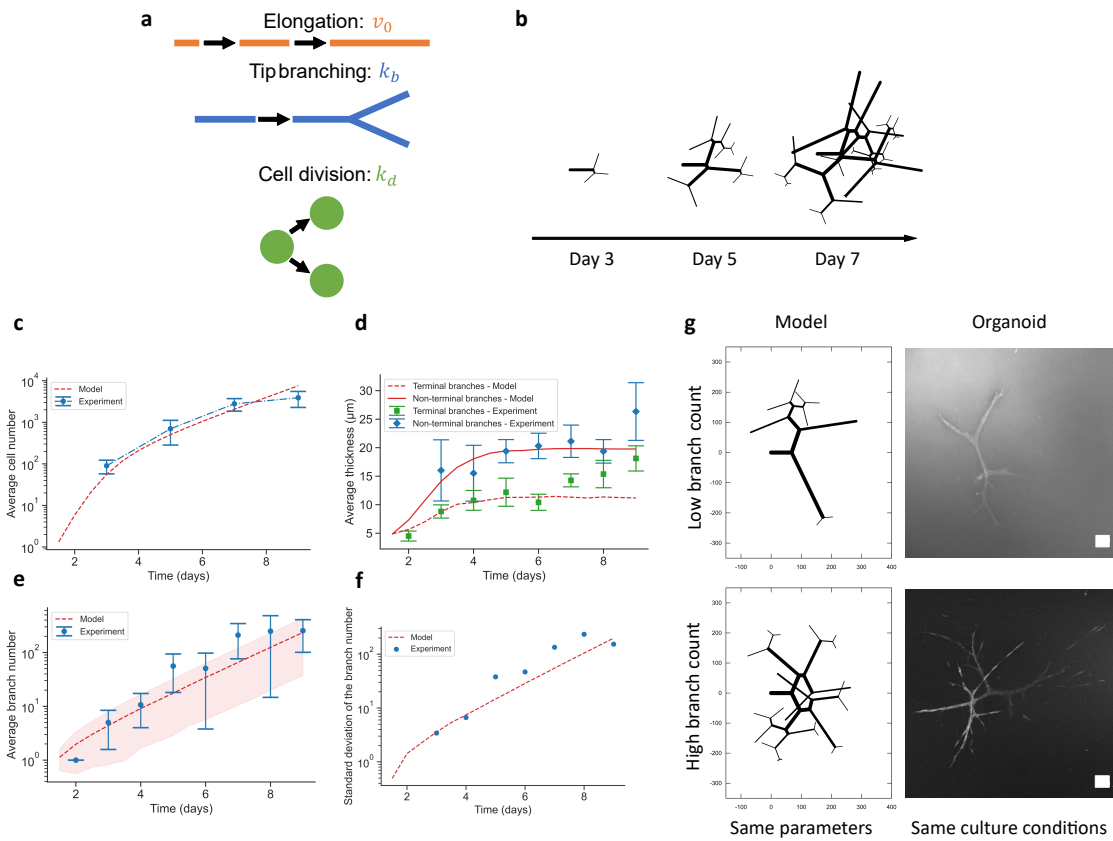


Figure 2.16: *Caption on the next page.*

Figure 2.16: **A minimal biophysical model captures the main morphogenetic dynamics from the onset phase up to the early thickening phase.** **a** Schematic representation of the processes considered in the model: branch elongation speed v_0 , branching rate k_b , and proliferation rate k_d . **b** Spatial simulation of the branching process over time in pancreatic organoids using the determined PDAC organoids' growth parameters. **c** Evolution of the cell number over time for experimental PDAC organoid data (Experiment, blue solid line, mean \pm sd, $n = 55$ organoids) and model predictions (red-dashed line). **d** Evolution of the measured mean branch width over time for terminal branches ($n = 1420$ terminal branches, $N = 74$ organoids) and for non-terminal branches ($n = 123$ non-terminal branches, $N = 53$ organoids), and predictions of the spatial model. Error bars: standard error of the mean. **e** Evolution of the branch number per organoid over time ($N = 65$ organoids) and prediction of the model. The blue dots indicate the mean tendency. Error bars: standard deviation. **f** Evolution of the measured standard deviation of the number of branches per organoid over time and prediction of the model. **g** Comparison between organoid shapes simulated by the spatial model (left column) and actual organoids (right column, plasma membrane stain, summed slice projection), both at Day 5. Note that due to the stochasticity of the branching process, the simulated organoids can capture the phenotype diversity in the number of branches, even though the simulations parameters identical in the top and bottom panels. Scale bars: 100 μm . Reproduced from [8].

2.4 Drug treatments - Functional experiments

To further investigate the biological mechanisms driving the branching morphogenesis of PDAC organoids, and challenge the predictions of our minimal model, we performed inhibition experiments using chemical compounds.

Aphidicolin - Inhibiting proliferation

We probed the role of proliferation in structure formation by using aphidicolin (Sigma A4487), an inhibitor of DNA replication, added at day 7 during the Extension stage.

We found that branch elongation was reduced but remained possible, before organoids progressively lost their extension phenotype, retracting their invasive protrusions and exhibiting tip rounding (Fig. 2.18a, c-d). As predicted by the model, we found that branches that remained capable of invasion became gradually thinner at their centres before breaking, underscoring the importance of a sustained generation of cells to maintain branch integrity upon elongation (Fig. 2.17d, h). For branching events occurring

2.4 Drug treatments - Functional experiments

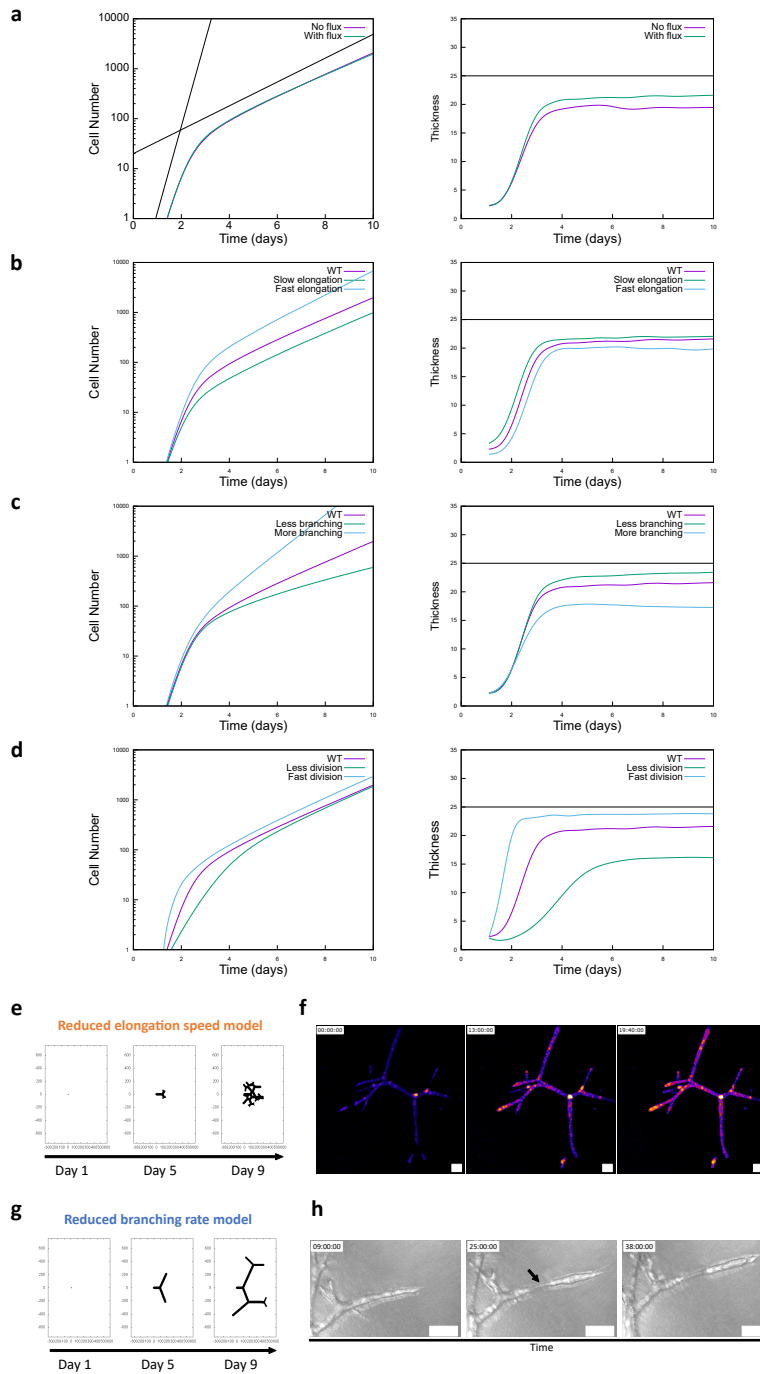


Figure 2.17: *Caption on the next page.*

following the addition of aphidicolin, we noted that the newly formed branches could not extend equally, likely because of an insufficient number of new cells being generated

Figure 2.17: **Sensitivity analysis for the minimal biophysical model.** **a-d** Model predictions of cell number evolution (left column) and of mean branch thickness evolution (right column), under different simulation parameters. Black lines in **a** are shown as a guide to the eye to indicate the initial exponential growth phase, before the plateauing. Black lines in the right column graphs indicate the maximum width w_0 allowed by the growth feedback, in absence of branching and elongation. Plots are averaged over $n=30$ simulations. **a** With/without cell flux between branching point; **b** With slower/faster elongation speeds compared to the WT parameters (elongation speed respectively divided by 2 and multiplied by 2); **c** With less/more branching comparing to the WT parameters (branching rate respectively divided by 2 and multiplied by 2); **d** With less/more division compared to the WT parameters (cell division rate respectively divided by 2 and multiplied by 2). **e** Spatial simulation of the branching process over time in pancreatic organoids using a reduced branch elongation speed **f** Local thickness increase visualization in a D8-9 organoid upon addition of 10 μM batimastat. The bright spots indicate areas of increasing thickness. The organoid does not extend in size but thickens, as predicted qualitatively by the model. **g** Spatial simulation of the branching process over time in pancreatic organoids using a reduced branching rate speed. **h** Bright field time-lapse of an organoid branch upon addition of 2 $\mu\text{g.mL}^{-1}$ of aphidicolin at D7. Black arrows indicate a spot of local branch thinning due continued cell migration but inhibited proliferation, as predicted qualitatively by the model. Scale bars in **f**, **h**: 100 μm . Reproduced from [8].

to sustain the branch growth (Fig. 2.18a, c).

Batimastat - Inhibiting MMP and invasion

We then probed whether MMP-mediated collagen degradation was essential for branching morphogenesis, by adding batimastat (Sigma SML0041) - a broad spectrum MMP inhibitor - during the Extension phase. Batimastat addition generally led to an arrest in branch elongation, with branches losing their extensile phenotypes, with a retraction of invading protrusions, and a rounding and thickening of branches (Fig. 2.18b-d, 2.17f), as predicted by our minimal model (Fig. 2.17c).

We also noted a reduction in the branch volumetric growth rate, also predicted as a consequence of the negative feedbacks on proliferation induced by the arrest of extension (Fig. 2.18c).

By treating organoids with batimastat at different time points of the developmental stage, we sought to identify where MMP-mediated invasion was critical to structure formation (Fig. 2.19). We found that addition of batimastat at seeding time or at day 3 or 5 during the Onset phase led to thin-branched organoids or small and scattered organoids, preventing the formation of thick-branched structures. In contrast, treating

organoids at day 9 or 11 - during the Thickening and the Lumen Formation phase respectively -, where branches should have normally stopped invading, did not have such drastic effect, with over 50% of organoids forming thick-branched structures.

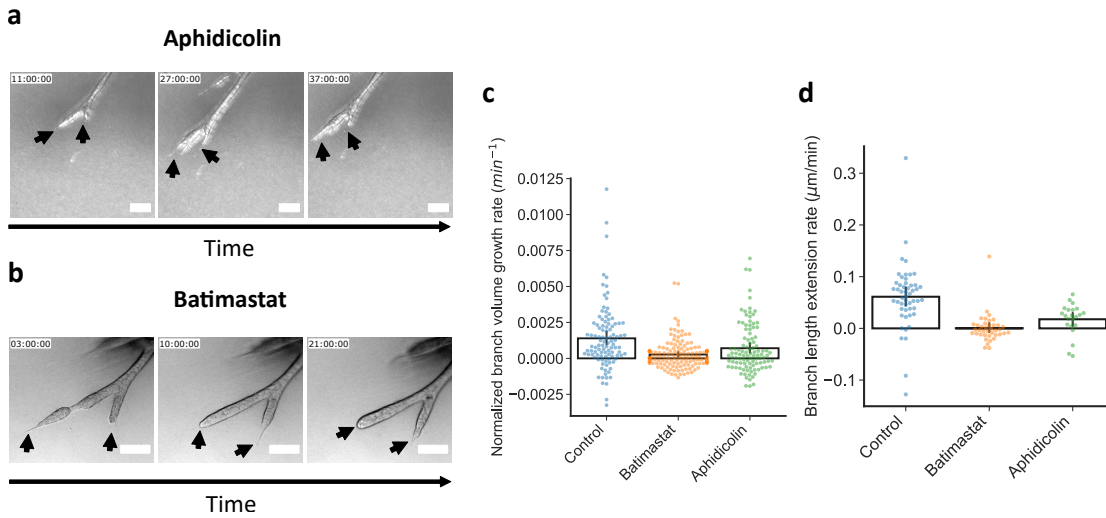


Figure 2.18: **Perturbing the structure formation processes.** **a** Time-lapse of an organoid branch upon addition of $2 \mu\text{g}\cdot\text{mL}^{-1}$ of aphidicolin at D7. Black arrows indicate spots of impaired branching. **b** Time-lapse of an organoid branch upon $10 \mu\text{M}$ batimastat addition at D8. Black arrows indicate stopped extension. **c** Normalised branch instantaneous volume growth rate for control ($n = 103$ points, $N = 3$ organoids), batimastat- ($n = 142$ points, $N = 2$ organoids), and aphidicolin-treated ($n = 103$ points, $N = 3$ organoids) organoids at the Extension stage. **d** Branch length extension rate for control ($n = 51$ branches, $N = 3$ organoids), batimastat- ($n = 39$ branches, $N = 2$ organoids), and aphidicolin-treated ($n = 22$ branches, $N = 3$ organoids) organoids at the Extension stage. Scale bars: $100 \mu\text{m}$. Black bar plots in c, d: mean \pm 95% CI. Reproduced and adapted from [8].

2.5 Transcriptional programs at play

To investigate the biological changes in organoids over the course of their development, we performed an analysis of the transcriptional profiles during the Extension phase at day 7 and during the Lumen Formation phase at day 13 (Fig. 2.20).

We found that the Extension phase, morphologically characterised by matrix invasion and branch elongation, displayed enrichment in markers such as Myc and E2F involved in cell proliferation signalling (Fig. 2.20c).

9591 originate from an epithelial cluster of Kras^{G12D} induced pancreatic cancer, and display this epithelial identity when cultured in 2D. Remarkably, we found that cells appeared to de-differentiate, during the Extension phase, towards a mesenchymal iden-

thelial identity at the transcriptional level.

We also compared the transcriptional profiles of Matrigel- and collagen-grown organoids at Day 13 to assess the effects of the culture ECM on the transcriptome. In addition to stark differences in morphologies and in growth dynamics, we observed that Matrigel- and collagen-grown organoids exhibited distinct transcription profiles (Fig. 2.2). Indeed, Matrigel spheroids displayed features of a basal-like identity of PDAC at Day 13, in contrast to the classical identity of Day 13 collagen-grown organoids.

2.6 Discussion: on branching morphogenesis

This thesis and its associated paper [8] have introduced PDAC-derived organoids as a powerful tool to investigate the spatiotemporal dynamics of tumour growth *in vitro*, in an architecturally-faithful manner.

Indeed, organoids grown in collagen displayed complex, self-organising, morphogenesis processes, leading to the emergence of tridimensional branched structures, displaying terminal end buds, and possessing a displaying a seamless lumen connecting the network, in an architecture highly reminiscent of PDAC pre-cancerous lesions *in vitro*, and in stark contrast with organoids grown in Matrigel which only formed spherical structures.

These organoids allow the observation in real time of the biophysical dynamics of branch formation and luminogenesis in real time, offering the opportunity to relate the extensively-characterised genetic events reported during morphogenesis with the physical processes shaping the structures.

We have observed that cells originating from epithelial clusters of *Kras*^{G12D}-induced pancreatic cancers, exhibited a switch to a rather mesenchymal identity (de-differentiation) within the early stages of development, before re-differentiating towards an epithelial identity in the later stages, underscoring the plasticity of cancer cells.

We also have evidenced that organoids initially displayed a so-called “basal-like” identity in the early stages, and later a “classical-like” gene signature as they formed lumens, which should prove useful for translational research and drug testing, given the strong influence of transcriptomic subtypes on therapeutic vulnerabilities.

Multiple reports have evidenced that the particular mechanisms for branching morphogenesis may differ from one organ to another [40, 107]. However, minimal biophysical models relying on fundamental (local) rules and self-organisation, have been shown to recapitulate key properties such as size and topology of modelled organs [41, 108].

Here, we found through modelling that a competition between proliferation, elongation and branching processes was key to determining the size and architecture of organoids during the Onset and Extension phases, and was sufficient to explain a large part of the observed heterogeneity.

2 Branching morphogenesis formation in pancreatic organoids

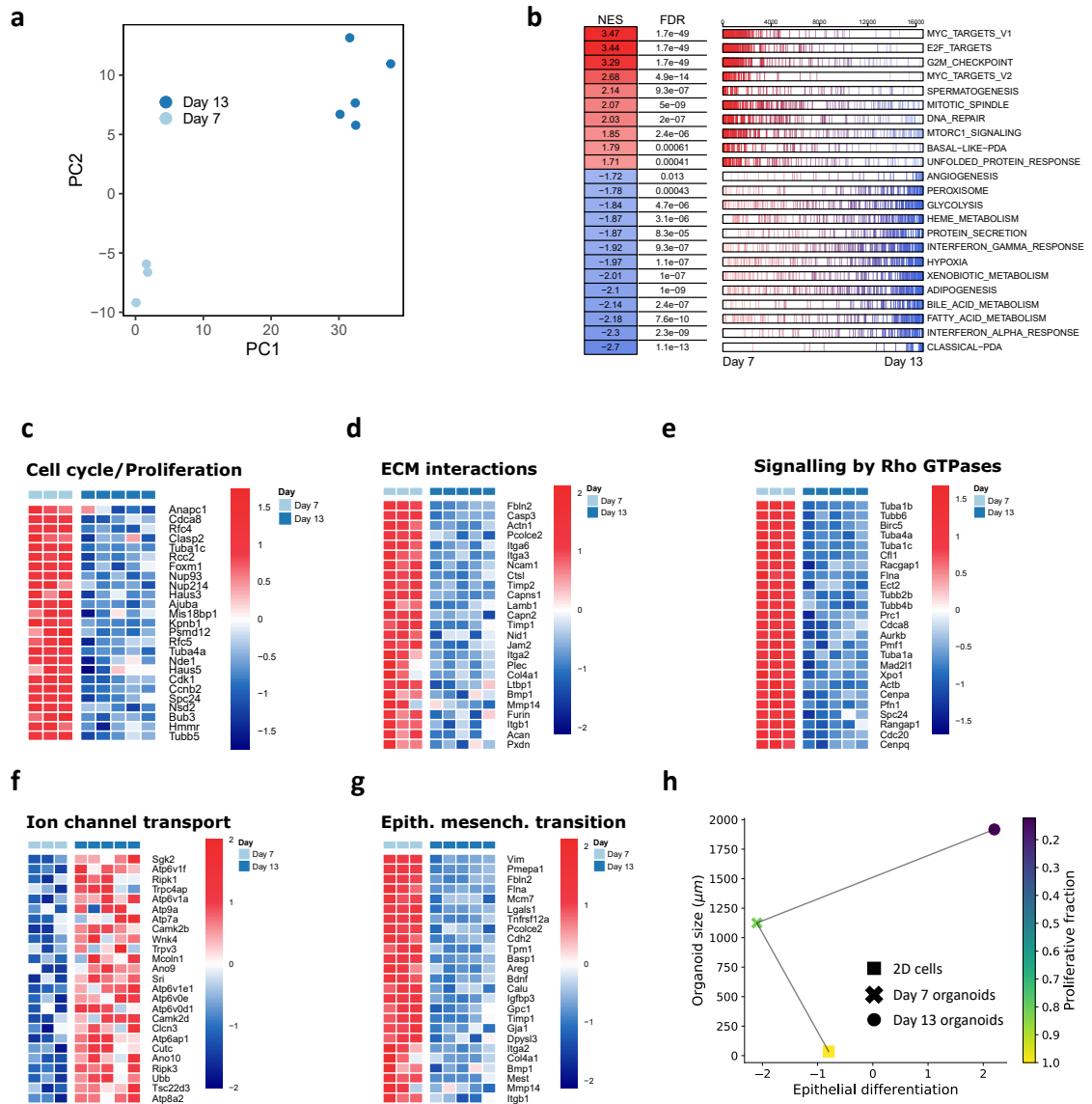


Figure 2.20: **Transcriptional profiles in organoids at Day 7 and 13.** Up- and downregulation genes heatmaps (\log_2 transformed) compare collagen-grown organoids at day 7 (D7) and 13 (D13). **a** Principal component analysis of bulk RNA sequencing of collagen-grown organoids at D7 ($n = 3$ individual experiments) and D13 ($n = 5$ individual experiments). **b** Corresponding up- and downregulated clustered pathways Transcriptional profiles heatmaps for: **c** Cell cycle- and proliferation-related genes; **d** Extracellular matrix- (ECM) related genes; **e** Rho GTPase signaling-related genes; **f** Ion channel transport-related genes heatmap. **g** Epithelial- and mesenchymal-related genes heatmap. **h** Developmental trajectory from 2D cells to D7 and D13 organoids. Reproduced and adapted from [8]

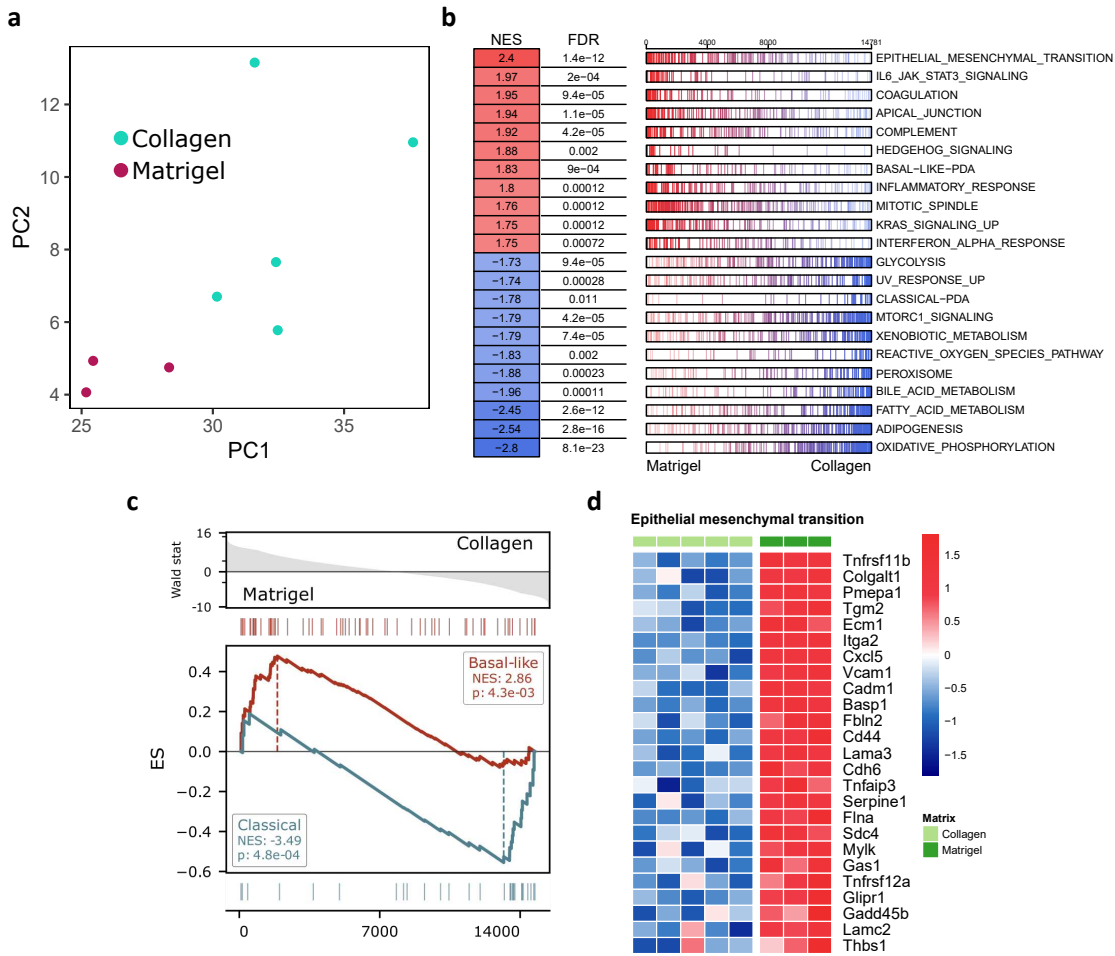


Figure 2.21: **Transcriptional profiles of Matrigel- and collagen-grown organoids at Day 13.** **a** Principal component analysis of bulk RNA sequencing of Day 13 Matrigel- (magenta, $n = 3$ independent experiments) and collagen-grown (cyan, $n = 5$ independent experiments) organoids. **b** Summary of gene set enrichment analysis between Matrigel- and collagen-grown organoids, showing normalised enrichment scores (NES) and false discovery rates (FDR). Bars represent individual genes for a given gene set. **c** Expression scores for the “Classical” and “Basal-like” signatures displayed by Matrigel- and collagen-grown organoids at Day 13. **d** Expression patterns for epithelial to mesenchymal transition (EMT) related markers, differentially expressed between Matrigel- and collagen-grown organoids at Day 13. Reproduced and adapted from [8].

3 Budding in pancreatic organoids

3.1 Focussing on bud formation - Rationale

Bud-like structures are a critical morphological feature of both the healthy exocrine pancreas and of its precancerous lesions [7].

Beyond the pancreas, buds are also crucial parts of other organs such as mammary glands [94] or the lung alveoli [88].

Beyond the immediate questions related to pancreas and pancreatic cancer, there exists a broader question of fundamental morphogenesis, on whether there exists commonalities in mechanisms leading to the formation of architecturally similar structures, or whether those structures arise from different mechanisms.

After the Extension phase in which organoids acquire their branched architecture, cell invasion and branching events stop, and organoids enter the Thickening phase, generally around Day 9 post-seeding.

Notably, we characterized the Thickening phase of organoid development by the arrest in the extension of branches, their switch from a spiky phenotype at the tip to a rounded one, their marked increase in width, and by a strong retraction of the organoid branches inducing a deformation in the surrounding collagen.

Some of the results shown in this chapter have led to a manuscript *Coexisting mechanisms of luminogenesis in pancreatic cancer-derived organoids*, in revision at the time of writing, authored with Marion Raich, under the supervision of Andreas R. Bausch, with the help of Dieter Saur for resources, and Maximilian Reichert for reviewing. Figures used in the submitted manuscript are marked with “Submitted for publication in *Coexisting mechanisms of luminogenesis in pancreatic cancer-derived organoids*”.

3.2 Experimental results and hypotheses

3.2.1 The transition from Extension to Thickening: A competition between extension and retraction processes

From a force balance perspective, the motion of branches can be interpreted as governed by a competition between processes that tend to favour extension (or maintain the branch extended), and processes that tend to oppose extension (or favour retraction). We summarise this balance between in Fig. 3.8.

Active cell migration (driven by the consumption of Adenosine triphosphate (ATP), and made possible thanks to MMP digesting the collagen), along with the compressive forces generated by the directed flow of cells from the stem of a branch to its tip, contribute to the extension. Opposing it, cell-cell adhesion (mediated by adhesion proteins

3 Budding in pancreatic organoids

such as cadherins) and active cell contractility (mediated by the actomyosin cortex) are components of the tissue tension, that should tend to minimise the surface area [109].

While extension forces are greater than retraction forces, the Extension phase continues. However, if retraction forces reach a threshold where they overcome the extension forces, the Extension phase should cease, and the Thickening phase starts (Fig. 3.8).

A quantitative estimation of forces and of the respective contributions of the different processes is made difficult by the absence of direct means to probe the organoids (see Section 2). We can however investigate at a qualitative/semi-quantitative level, by studying the variations in the expression of key molecular players, and branches and cells motions and interactions with the extracellular matrix.

3.2.2 Experimental results on key molecular players

The deformation field evidenced during the Thickening phase (Fig. 2.10b), prompted an investigation into the sources of the forces at play.

Due to their ubiquitous roles in force generation and transmission in cells, we looked at the behaviour of actin, myosin, and E-cadherin, [110, 111].

Actin Using SiR-actin (SC001 Spirochrome), a fluorescent probe binding to actin, and a LifeAct-expressing murine PDAC cell line (see Methods chapter 5), we imaged organoids using live confocal microscopy, between the Extension and the Thickening phases.

Prior to the thickening of the branches, the actin signal appeared to be homogeneously distributed throughout the organoid along the spindle-like cell cortex.

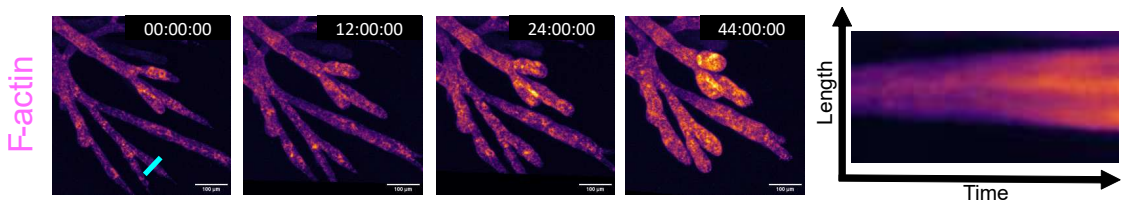


Figure 3.1: **Representative time-lapse of F-actin distribution in branches and buds**, labelled by SiR-actin during the Thickening phase, and corresponding kymograph taken along the cyan line.

During budding however, we detected an increasing F-actin signal in the forming terminal end bud-like structures (Fig. 3.1).

To rule out the possibility of this signal increase being solely due to cell compaction despite actual actin expression remaining constant, we used a Caax-tagged cell line expressing YFP labelling the membrane (see Methods), and checked whether we could observe a similar increase in brightness of the buds.

Upon budding, we could not detect a marked increase of the YFP-Caax signal, leading us to conclude that the increase in the actin signal was due to actual up-regulation (Fig. 3.2).

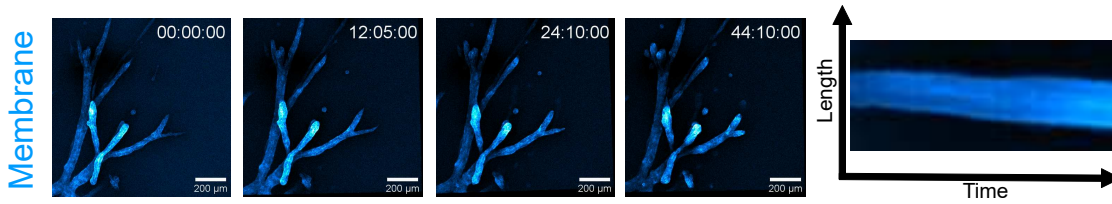


Figure 3.2: **Representative time-lapse of cell membrane intensity in a YFP-Caax 9591 cell line during the Thickening phase**, and corresponding kymograph taken along a bud. In collaboration with Marion Raich.

Myosin Next, we aimed to determine whether the rounding and retraction of a branch was the result of a myosin-mediated process.

Using an overexpressing myosin-IIa GFP-tagged cell line (see Methods), we detected myosin heavy chain expression along the branches, notably on their basal side and along a central line (Fig. 3.3).

Live-cell imaging revealed that the global intensity of the myosin signal did not appear to increase as organoids thickened, and that myosin went from initially distributed relatively homogeneously, to relocated to the basal side of organoids and along a central line in the branches.

Immunostaining against phosphorylated-myosin light chain 2 similarly displayed a strong signal at the basal side of organoids, as well as a signal on the apical side, (see Fig. 3.4).

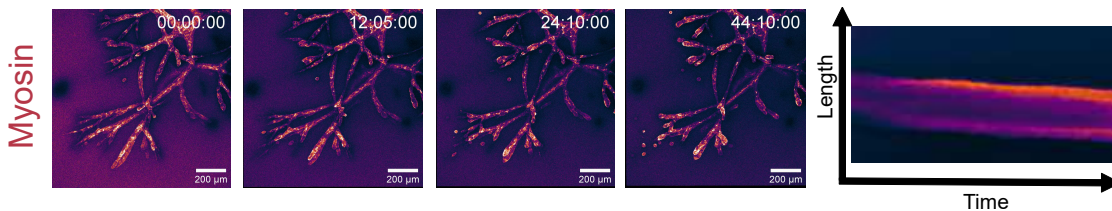


Figure 3.3: **Representative time-lapse of myosin intensity in a GFP-tagged 9591 cell line during the Thickening phase**, and corresponding kymograph taken along a bud. In collaboration with Marion Raich.

E-cadherin We then wondered if changes in the cadherin expression could be accompanying the observed increase in the actin signal and contribute to explaining the budding behaviour. Indeed, cadherins, through their connection to actin filaments (via p120, β -catenin and α -catenin) have been reported to play a key role in morphogenetic processes via the transmission of forces, the reorganisation of cell-cell contacts, tissue stiffening, and mechanosensing [112, 113].

To monitor the dynamics of cadherin expression, we imaged an endogenous E-cadherin-tagged cell line, labelled with mNeonGreen, and could observe a gradual increase in intensity, as organoids transitioned from the Extension to the Thickening phase. Cells expressed E-cadherin on the basal and lateral sides, and developed a strong signal at the

3 Budding in pancreatic organoids

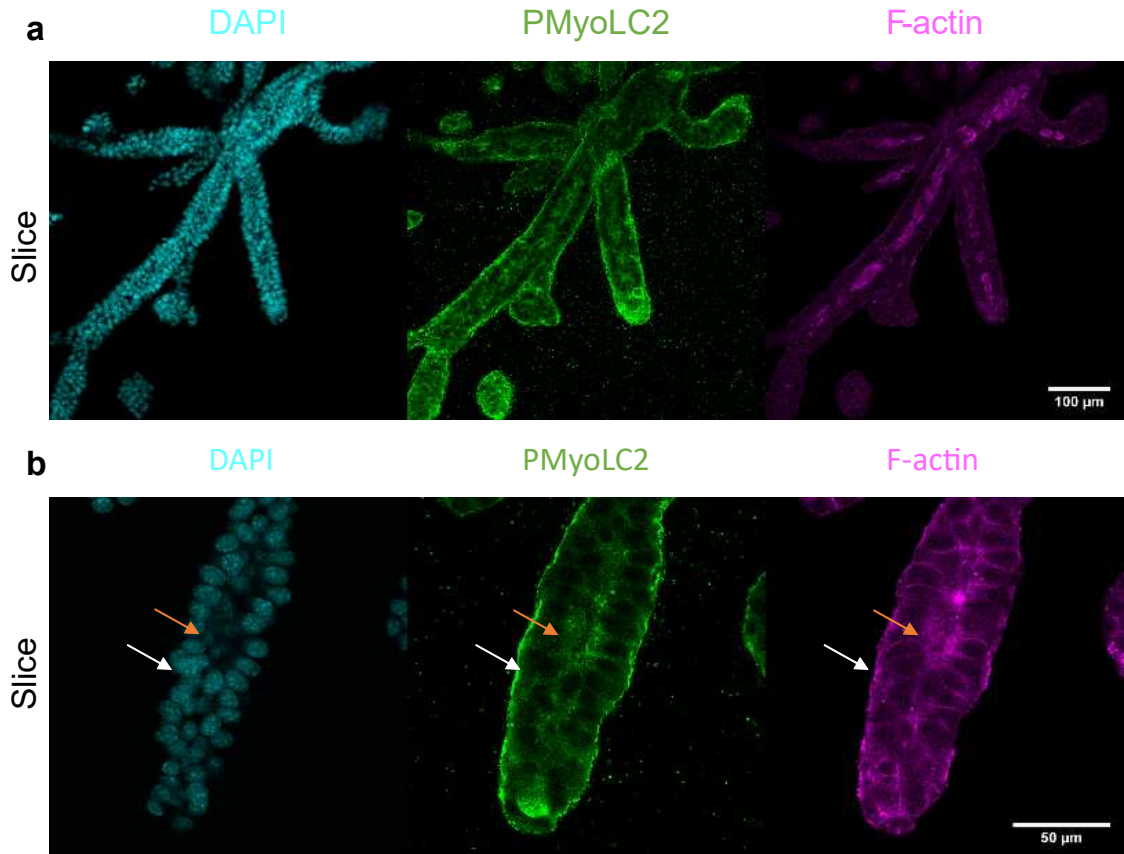


Figure 3.4: **F-actin and PMLC2 distribution in organoids with lumens.** **a** Staining of Phosphorylated Myosin Light Chain 2 (PMLC2) and F-actin in an organoid displaying nucleating lumens. **b** Closeup view of terminal structures. The white arrow indicates the basal side and the orange arrow indicates the apical side. Submitted for publication in *Coexisting mechanisms of lumino-genesis in pancreatic cancer-derived organoids*

future apical side, in the centre of the branch (Fig. 3.5).

Thus, the globally increasing actin and E-cadherin signals and the relocation of myosin to the basal side of the organoids suggest an increase in the tension of branches.

This rise in branch tension, evidenced by the change in intensities and/or distributions of key molecular players, should therefore, absent a compensatory increase in extension processes magnitude of effect, favour an arrest in branch elongation up to branch retraction.

To investigate whether indeed, there was no (or at least not sufficient) increases in extension forces that could prevent retraction, we analysed how the active cell migration, cell-ECM adhesion and proliferative pressure processes varied during the Extension and the Thickening phase.

Active cell migration Decoupling a potential decrease in the active cell migration

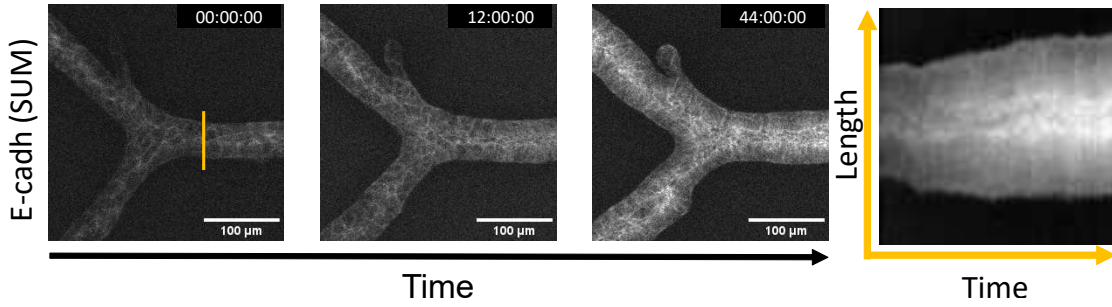


Figure 3.5: **Representative time-lapse of E-cadherin intensity in a mNeonGreen-tagged 9591 cell line during the Thickening phase,** and corresponding kymograph taken along a bud. Submitted for publication in *Coexisting mechanisms of luminogenesis in pancreatic cancer-derived organoids*

capabilities of cells from the effective empirical arrest of cell migration is difficult.

We can however analyse the cell motion prior to the Thickening phase to explore whether signs of active migration capability decrease are visible.

Tracking cell motion in organoids labelled with SiR-DNA during the Extension phase, we observed a constant mean velocity from day 7 to day 10 [114] (Fig. 3.6). Similarly, we could not evidence a significant correlation between the tip speed and its width during the extension phase (Fig. 2.11c).

These two observations argue for constant active cell migration velocities until the arrest brought by the transition to the Thickening phase. This indicates that for this extension process, there is no increase in magnitude that would oppose the increase in tissue tension.

Active cell migration could potentially be affected by a loss in cells' ability to digest collagen, mediated by MMP. Bulk RNA sequencing revealed a downregulation in MMP expression from organoids during the extension phase at day 7 to the lumen formation phase at day 13, but it remains unclear whether this downregulation occurs as a consequence of the thickening, or is correlated in time with it (Fig. 2.20d).

Cell-ECM adhesion Reflection microscopy revealed that collagen fibres remain in contact with the forming buds, indicating that cell-ECM adhesion is preserved during the Thickening phase, through integrins notably (see Fig. 2.7).

In rare cases however, a loss of adhesion at the tip indeed led to branch retraction, which support the hypothesis that tension being able to trigger rounding (see Fig. 3.7).

Proliferative pressure Lastly, dividing cells in the branches can generate compressive forces that may drive the extension by pushing the leading cells forwards. Considering a one dimensional branch of length $L(t)$ extending solely due to the effect of proliferative pressure, we can generally write:

3 Budding in pancreatic organoids

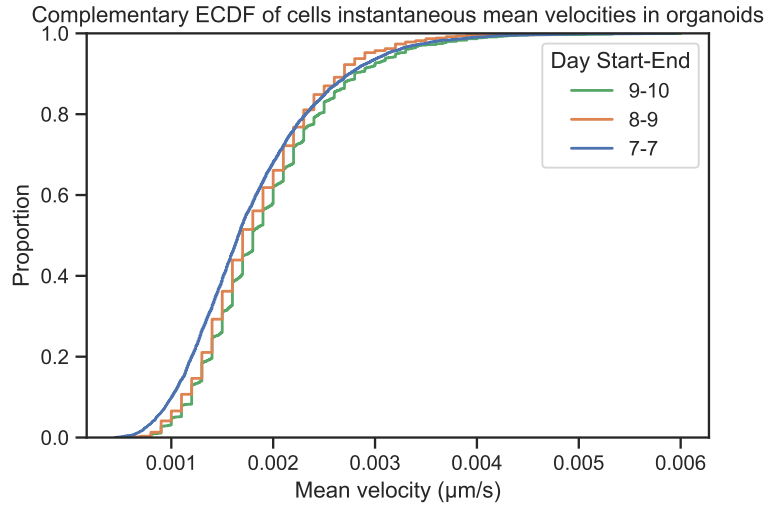


Figure 3.6: **Complementary empirical cumulative distribution functions of cell mean velocities in organoids at different time points.** Data acquired in collaboration with Giulia Zecchin [114]. N=5 organoids (7-7:2; 8-9:1; 9-10:2)

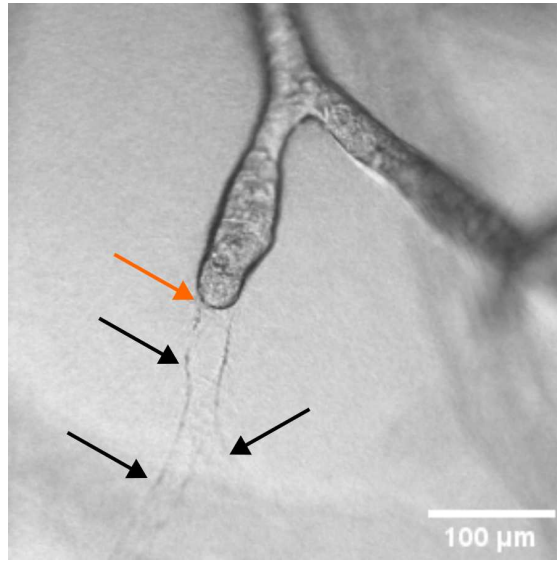


Figure 3.7: **Bud forming after adhesion loss at the tip.** The black arrows indicate the collagen path left behind the branch as its tip cell(s) lost their adhesion to the ECM, leading to the retraction and the rounding of the branch. Scale bar: 100 μm .

$$\xi L'(t) = \sigma_p(t) \quad (3.1)$$

$$\xi L'(t) = \chi \rho(t) \quad (3.2)$$

$$\rho(t) = N(t)/L(t) \quad (3.3)$$

3.2 Experimental results and hypotheses

with ξ a friction term, $L(t)$ the length of the branch, $L'(t)$ the elongation of the branch, σ_p the compressive stress generated by proliferation, χ a compressibility, $\rho(t)$ the cell density, $N(t)$ the number of cells in the branch.

Experimentally, stainings against Ki67, a proliferation marker, revealed an overall progressive decrease of the proliferative population as organoid age increased (Fig. 2.10c-e).

We define $\beta(t) = N_{Ki67+}(t)/N(t)$ as the ratio between the Ki67-positive population and the total cell population in a branch, found to decrease over time. For generality, we consider the decay of the ratio to be polynomial in time, with k_β a decay constant, so that

$$\beta'(t) = -k_\beta t^n \quad ; \quad \text{with } n \geq 1, n \in \mathbb{R} \quad (3.4)$$

With $\beta(t=0) = 1$ as all cells are initially capable of proliferation, we find

$$\beta(t) = 1 - \frac{k_\beta}{n+1} t^{n+1} \quad (3.5)$$

Assuming a proliferation rate k_d , we can write the number of cells at a certain time point as

$$N(t + \Delta t) = N(t) + k_d N_{Ki67+}(t) \Delta t \quad (3.6)$$

$$\frac{N(t + \Delta t) - N(t)}{\Delta t} = k_d \beta(t) N(t) \quad (3.7)$$

$$\implies \frac{N'(t)}{N(t)} = k_d \beta(t) \quad (3.8)$$

$$(3.9)$$

Integrating, we find

$$\ln N(t) = k_d \int \beta(t) dt \quad (3.10)$$

$$= k_d \left[\int dt - \frac{k_\beta}{n+1} \int t^{n+1} dt \right] \quad (3.11)$$

$$= k_d \left[t - \frac{k_\beta}{(n+1)(n+2)} t^{n+2} + C \right] \quad (3.12)$$

$$\implies N(t) = e^{k_d t} \times e^{-\frac{k_d k_\beta}{(n+1)(n+2)} t^{n+2} + e^{k_d C}} \quad (3.13)$$

with C an integration constant. As organoids arise from a single cell, we have $N(t=0) = 1$, thus $C = 0$ and we find

$$N(t) = e^{k_d t (1 - \frac{k_\beta}{(n+1)(n+2)} t^{n+2})} \quad (3.14)$$

We can now rewrite the stress σ_p generated by proliferation as

3 Budding in pancreatic organoids

$$\sigma_p(t) = \frac{\chi}{L(t)} e^{k_d t (1 - \frac{k_\beta}{(n+1)(n+2)} t^{n+2})} \quad (3.15)$$

If we study the limit behaviour as $t \rightarrow \infty$, we have $\lim_{t \rightarrow \infty} L(t) = L_f$, with L_f a finite length, as empirically, organoids reach a finite size and do not grow infinitely.

Therefore, looking at the highest degree term, we find

$$\lim_{t \rightarrow \infty} \sigma_p(t) = \lim_{t \rightarrow \infty} e^{-t^{n+2}} \quad (3.16)$$

$$= 0 \quad ; \quad \forall n \geq 0, n \in \mathbb{R} \quad (3.17)$$

$$(3.18)$$

Furthermore, we also evidenced a negative linear dependency between the volumetric growth rate of branches and their width (Fig. 2.13), further arguing for a decrease in proliferation forces in the organoids in general, and in the branches in particular.

Taken together, these observations suggest that proliferative forces should decrease during the transition between the Extension and the Thickening phases.

Intermediate conclusion

In summary, having evidenced experimentally the increase in tissue tension - shown through the actin, myosin and E-cadherin signals -, and the absence of increasing extension forces - with a constant cell velocity pre-Thickening, a maintained cell-ECM adhesion, and decreasing proliferation capabilities -, support the idea of a switch between the Extension and the Thickening phase mediated by an alteration in the balance between the different forces at play.

This simple picture is schematised in Fig. 3.8.

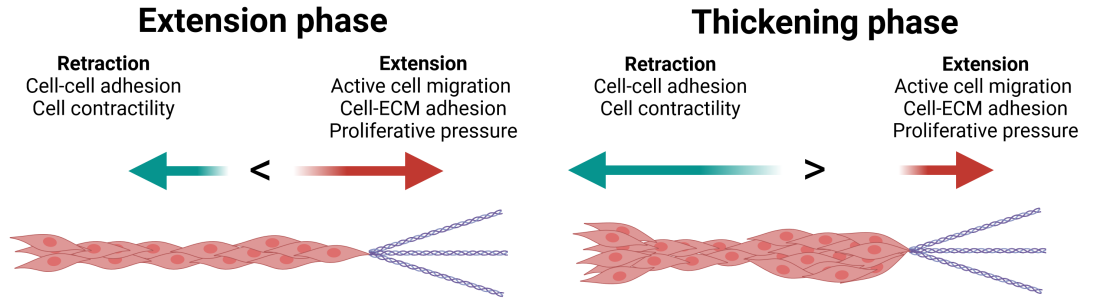


Figure 3.8: **Schematic balance of forces exerted on a branch.** Created with BioRender.

3.2.3 Apparition of bud-shape structures

The imbalance between the retraction and the extension forces should not only explain why branches' extension is arrested, but also why they thicken and bud.

Simplified case: without proliferation

We first consider the simplified case of a branch without proliferation, as it will allow us to use a volume conservation argument, and later relax this assumption.

Considering a cylindrical branch of radius r and of length l with constant volume, we write

$$V(t) = l(t) \times \pi r(t)^2 \quad (3.19)$$

$$V(t + \Delta t) = l(t + \Delta t) \times \pi r(t + \Delta t)^2 \quad (3.20)$$

$$V(t + \Delta t) = V(t) \quad (3.21)$$

with

$$l(t + \Delta t) = l(t) + \Delta l \quad (3.22)$$

$$r(t + \Delta t) = r(t) + \Delta r \quad (3.23)$$

$$(3.24)$$

and $\Delta l = k_l \Delta t$, k_l being the rate of extension or retraction of the branch. Momentarily omitting the time dependency notation, we can thus write

$$(l + \Delta l)(r + \Delta r)^2 = lr^2 \quad (3.25)$$

$$\implies (r + \Delta r)^2 = \frac{lr^2}{l + \Delta l} \quad (3.26)$$

$$\implies r + \Delta r = r \sqrt{\frac{l}{l + \Delta l}} \quad (3.27)$$

$$\Delta r = r(t) \left(\sqrt{\frac{l(t)}{l(t) + \Delta l}} - 1 \right) \quad (3.28)$$

For a branch retracting, we have $\Delta l < 0$ and

$$0 < l + \Delta l < l \quad (3.29)$$

$$\sqrt{\frac{l}{l + \Delta l}} > 1 \quad (3.30)$$

$$\implies \Delta r > 0 \quad (3.31)$$

and thus the branch radius (its thickness) should increase.

Accounting for proliferation

Experimentally, we however evidenced that some proliferation is still possible in the branches, as shown by the Ki67 signal (Fig. 2.10c-e) present in the branches. We now relax the constant volume assumption so that

$$V(t + \Delta t) \neq V(t) \quad (3.32)$$

$$V(t + \Delta t) = V(t) + \Delta V \quad (3.33)$$

with ΔV the volume change of the branch over a time step Δt . Thus

$$V(t) = l(t)\pi r(t)^2 \quad (3.34)$$

$$V(t + \Delta t) = l(t + \Delta t)\pi r(t + \Delta t)^2 \quad (3.35)$$

$$l(t + \Delta t) = l(t) + \Delta l \quad (3.36)$$

$$r(t + \Delta t) = r(t) + \Delta r \quad (3.37)$$

Injecting the above in Eq. 3.33, we can write

$$l(t + \Delta t)\pi r(t + \Delta t)^2 = l(t)\pi r(t)^2 + \Delta V \quad (3.38)$$

$$(l + \Delta l)\pi(r + \Delta r)^2 = l\pi r^2 + \Delta V \quad (3.39)$$

$$\implies \Delta r = \sqrt{\frac{lr^2}{l + \Delta l} + \frac{\Delta V}{\pi(l + \Delta l)}} - r \quad (3.40)$$

We consider that the volume increase ΔV during the time Δt is driven solely by proliferation so that

$$\Delta V = k_d \beta(t) N(t) V_c \Delta t \quad (3.41)$$

with k_d the proliferation rate, $\beta(t)$ the fraction of proliferative cells over the total number of cells, $N(t)$ the number of cells in the branch, and V_c the volume of a single cell (that, for simplicity, we assume is identical for every cell).

We can approximate a cylindrical branch as a sum of K cell disks of identical width w and radius r , defining each disk as containing N_D cells of individual volume V_c , so that the branch length $l(t)$ can be rewritten as

$$l(t) = K(t) \times w \quad (3.42)$$

and the volume V_D of a cell disk can be written as

$$V_D = w\pi r^2 \quad (3.43)$$

$$= N_D V_c \quad (3.44)$$

$$\implies V_c = \frac{w\pi r^2}{N_D} \quad (3.45)$$

Using Eq. 3.41 and 3.45 in 3.40 we can write

$$\Delta r = \sqrt{\frac{lr^2}{l + \Delta l} + \frac{k_d \beta(t) N(t) V_c \Delta t}{\pi(l + \Delta l)}} - r \quad (3.46)$$

$$\Delta r = \sqrt{\frac{lr^2}{l + \Delta l} + \frac{k_d \beta(t) N(t) \Delta t w \pi r^2}{N_D \pi(l + \Delta l)}} - r \quad (3.47)$$

$$\Delta r = r(t) \left(\sqrt{\frac{l(t)}{l(t) + \Delta l} + \frac{k_d w \beta(t) N(t) \Delta t}{N_D (l(t) + \Delta l)}} - 1 \right) \quad (3.48)$$

Note that in the limit where $\beta(t) = 0$, i.e. there are no proliferating cells in the branch, we find back Eq. 3.28, where the change in radius is solely driven by volume conservation.

With $\frac{l}{l + \Delta l} > 1$ and $\frac{k_d w \beta N \Delta t}{N_D (l + \Delta l)} > 0$ we thus have $\Delta r > 0$ indicating a thickening of the branches.

Rounding

Having established that branches should undergo thickening under the combined effect of volume conservation upon retraction and proliferation, we then turned to the apparition of rounded, bud-like structures at the tip of the branches.

Prior to bud formation, branches in the Extension phase consist of spindle-like cells and possess a spiky protrusion at the tip in front of which MMP can degrade the collagen and allow elongation.

The loss of the spiky protrusions, indicative of the end of the Extension phase can be the result of a phenotype change upon loss of ability to degrade the collagen. Indeed, at the molecular level, we observe a downregulation of MMP14 transcription between Day 7 and Day 13, which indicates a reduction, if not a complete loss, of the organoids ability to produce the MMP necessary to digest the collagen (Fig. 2.9). Moreover, bulk RNA-sequencing revealed hallmarks of a mesenchymal to epithelial transition, with transcription of key mesenchymal genes decreasing after the Extension phase (Fig. 2.20g).

At the physical level, the retraction of the spiky protrusions, and, similarly, the rounding of the branches can be interpreted as a minimisation of the surface area from a cylinder to a sphere due to tissue tension.

The surface tension γ of a film, can be written in energy terms as

$$\gamma = \frac{W}{\Delta A} \quad (3.49)$$

where W is the work (a potential energy) required to increase the surface area by ΔA , due to resisting forces (in a biological tissue, cell-cell adhesion and cell contractility would be analogous to the intermolecular forces in a fluid).¹ Considering two geometrical

¹We note that while a system driven by mechanics should minimise its total potential energy, therefore

3 Budding in pancreatic organoids

objects of the same height and radius: a sphere of radius r , and a cylinder of base radius r and of height $h = 2r$, the surface area² of the sphere is

$$4\pi r^2 \quad (3.50)$$

whereas the surface area of the cylinder is

$$2\pi r(h + r) = 6\pi r^2 \quad (3.51)$$

This explains why fluids, at their lowest energy state, tend to form droplets (i.e. spheres) as it corresponds to their minimum surface area (see Fig. 3.9, adapted from [116]).

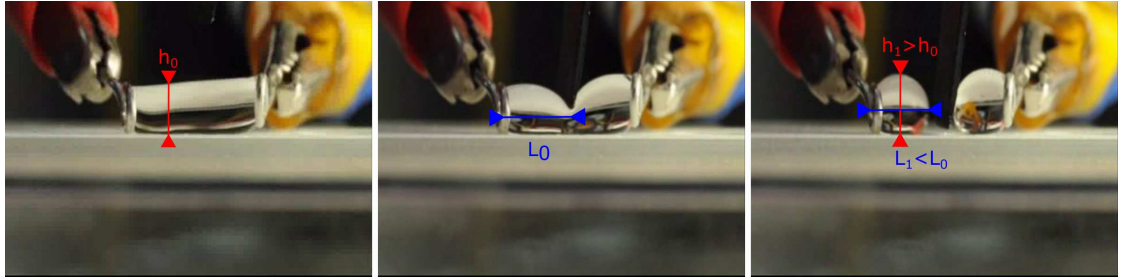


Figure 3.9: Cutting a water cylinder using a super hydrophobic knife, on a super hydrophobic surface. As the length of the droplet decreases from L_0 to L_1 , its height (the "thickness" of the cylinder) proportionally increases from h_0 to h_1 , due to surface tension and de-wetting. Adapted from [116]

Organoids branches are, however, both laterally constrained by the collagen cage that surrounds them, and remain adhering to the collagen fibres at their front, which explains why branched organoids do not form into spheroids during the Thickening phase.

Breakage events in branches in the Extension and Thickening phases lend credence to the hypothesis of a minimisation of surface area driving the budding of cells (Fig. 3.10).

In the Extension phase, thin branches can transiently rupture due to cell-cell adhesions being locally too low to keep migrating cells adhering together, or due to a division event that locally break the connectivity in a single file of cell. Branches are able to recover and reconnect broken parts (Fig. 3.10a) due to cells spatially before and after the break being able to migrate.

In the Thickening phase, this recovery behaviour disappears upon branch breakage (Fig. 3.10b-c). Breakage can similarly occur due to division events breaking the connectivity or due to a branch being locally too thin to withstand the retraction forces. Following the break however, both ends retract on their side and thicken.

leading to a minimisation of surface area, biological systems consuming ATP may, in principle, not follow this total potential energy minimisation due to the active processes keeping the system out of mechanical equilibrium [115]. Such conditions may considerably complicate the modelling.

²Famously shown by Archimedes, and engraved on his tomb, cf. Plutarch, *The Parallel Lives*, *The Life of Marcellus*, Loeb Classical Library edition Vol. V, 1917

Notably, the most distal parts of the branches appear to round up in quasi-spherical structures, matching the predictions of surface area minimisation, as the tissue tension increases while organoids transition from the Extension phase to the Thickening phase.

We note that under the hypothesis of a retraction process driven by e.g. contractile waves generated from the core, the rounding should have stopped upon breakage for the separated cells,

3.2.4 Inhibition experiments

We turned to chemical perturbations, to further challenge the idea of a balance between extension and retraction processes mediating the evolution of branch shape, the switch between the Extension and Thickening phases, and the synchronous thickening and rounding of branches. The results of these experiments are discussed below and summarised in Figure 3.12.

Batimastat - Inhibiting active migration

Ceteris paribus, decreasing the “forward active migration term” during the Extension phase should lead to a stop in the branch elongation and a budding of the branches. To probe this, we performed MMP-inhibition at the Extension phase by adding batimastat (SML0041 - Sigma), a broad spectrum MMP-inhibitor.

Deprived of their mean to digest the collagen in front of them, branches stopped elongating, and started thickening prematurely as evidenced by the plateauing of the projected area and the decrease in the projected perimeter (Fig. 3.12b, f).

In addition to the “retraction” processes still being active, proliferation, unable to contribute to longitudinal branch extension (due to collagen not being degraded), is now contributing to the radial expansion.

Tracking of the area and perimeter of organoids however revealed that a subpopulation appeared unaffected by the batimastat treatment. We explore possible interpretation of this finding in the Discussion section below.

Calyculin A - Increasing contractility

Taking our hypothesis to the extreme, the minimal surface area organoids could reach upon increasing their surface tension would be a sphere (see Eq. 3.49, 3.50, 3.51). Therefore, increasing cell contractility should allow branches to further retract and round up. To test this, we used calyculin A (PHZ1044, ThermoFisher) a myosin phosphatase inhibitor [117, 118, 119, 120], added it during the Extension phase, and observed a striking increase in the contraction and retraction of organoids (Fig. 3.12c,g), with terminal branch segments occasionally retracting into the previous non-terminal branch segment.

This combination of increased contractility and merging contributes to a general rounding of the organoids, whose shapes get closer to a sphere, although they are likely prevented from achieving complete sphericity due to constraints on cell packing, and due to the previously remodelled collagen environment (Fig. 3.12c)

3 Budding in pancreatic organoids

We also found that, qualitatively, upon exposure to calyculin A, organoids with thinner branches tended to display branch fragmentation upon retraction, especially for the tip cells, whereas organoids with thicker branches tended to be more cohesive (Fig. 3.11).

For a thin organoid, if the cell-cell adhesion is not strong enough, then the increase of individual cell contractility can locally lead to breakage events. In contrast, thicker organoids should have higher levels of cell-cell adhesion, if only because the branches are wider at equal E-cadherin levels (but also potentially because they might be more "mature" and thus express higher levels of E-cadherin), thereby preventing the apparition of breaking points and allowing a more homogeneous distribution of the forces over the entirety of the branch.

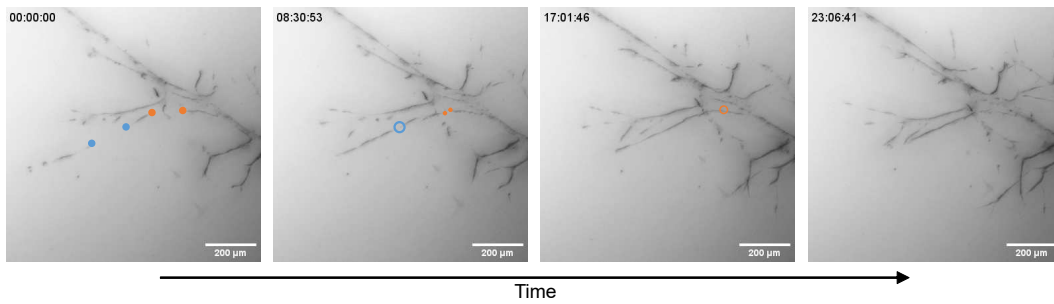
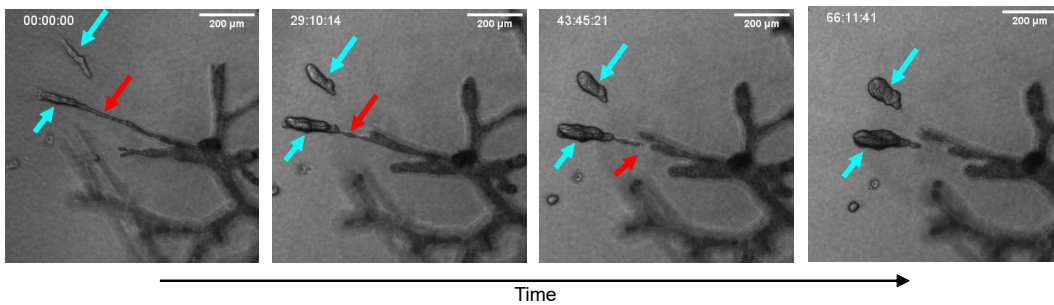
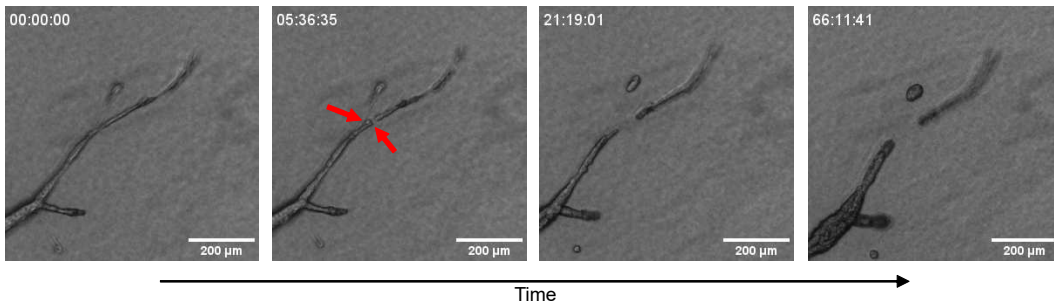
Blebbistatin - Inhibiting contractility

Conversely, we wanted to probe the effects of decreased contractility at the Extension phase, by adding nitro-Blebbistatin (Santa Cruz Biotechnology, sc-212797), an inhibitor of myosin ATPase activity [117, 121]. Treating the organoids with 50 μM nitro-blebbistatin led to a stop of the extension process and to the rounding and retraction of branches, inducing breakage at the tip of the branches, but leading to the apparition of rounded tip structures reminiscent of buds (see Fig. 3.12d, h).

The fact that a phenomenon morphologically similar to budding could occur, despite myosin ATPase activity inhibition, tends to support the hypothesis that budding is not a process driven solely by myosin-mediated contractility.

We believe that 50 μM of nitro-blebbistatin was sufficient to inhibit the myosin ATPase activity required for cell migration, hence the stop in branch extension, but could not prevent the formation of bud-like structure due to the cell-cell adhesion component of surface tension remaining active, as well as to enough cell contractility potentially remaining.

Corroborating this hypothesis, treating the organoids at 250 μM nitro-blebbistatin completely inhibited both the extension but also the thickening and the budding, due to cells rounding up and losing their cohesiveness (Fig. 3.13).

a Recovery event - Broken parts in the Extension phase can fuse back**b** Branch too thin - Breakage during retraction in the Thickening phase**c** Division event - Breakage during retraction in the Thickening phaseFigure 3.10: **Breakage events in the Extension and in the Thickening phases.**

a Time-lapse of a recovery event in the Extension phase, where a branch that had broken in multiple segments is able to fuse back. The filled disks indicate the segments connected ends prior to the breakage events. The non-filled circle indicate the re-connection events, with the last panel showing a fully restored branch. **b** Time-lapse of a breakage event during the Thickening phase, where a locally thinner region in a branch, marked by the red arrow, is not able to withstand the thickening forces and breaks. Note that the terminal structures marked by the cyan arrows are still able to thicken and round up after the breakage event. **c** Time-lapse of a breakage event, where cell division, marked by the red arrow, causes a break in the branch that cannot be recovered from, as the Thickening phase has started. Note that both the broken fragments and the main branch are able to thicken and round up. Scale bars: 200 μm . Bright field images in **a**: minimum projections; in **b**, **c** planes.

3 Budding in pancreatic organoids

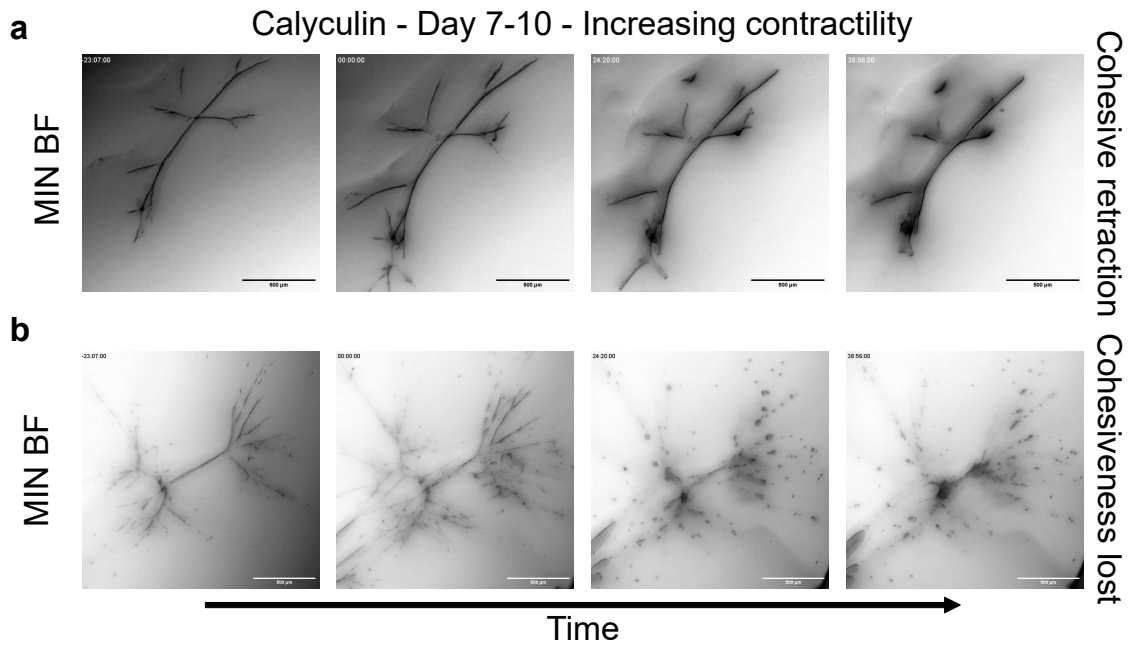


Figure 3.11: **Phenotype dependency - Calyculin.** Upon treatment during the Extension phase with 0.5 nM of calyculin A, qualitatively thicker organoids (pre-drug addition) tend to display a cohesive retraction and thickening pattern (**a**), where thinner organoids tend to display a loss of cohesiveness upon retraction (**a'**). This is consistent with the hypothesis of higher cell-cell adhesion levels in thick organoids. Scale bars: 500 μ m.

3.3 Discussion: on budding

We have shown that the hypothesis of a balance between extension and retraction processes mediating the transition between the Extension and the Thickening phase was supported by observations of increase in molecular players of tissue tension, observations and theoretical considerations regarding the role of proliferation, and chemical perturbations experiments.

In this thesis, we have elected to focus on the form of buds in pancreatic organoids, rather than on their putative function as potentially differentiated acini. Given our use of cancer cells as a model, it was indeed unclear whether one should have expected a differentiation of cells toward a healthy and functional phenotype. Conversely, it is unclear whether cancerous structures should have a “function” in the physiological sense of the term, rather than be a by-product of cancer, encoding its (deregulated) morphological processes.

3.3.1 Organoid population not or less susceptible to batimastat treatment

Quantification of the projected area and perimeter revealed the existence of a population of organoids that did not stop extending upon treatment with 10 μM batimastat (Fig. 3.12b, e).

While the reason for this discrepancy is unclear at the stage of writing, we suggest some hypotheses for future investigation. A first hypothesis could be that 10 μM batimastat is not enough to completely inhibit the extension of organoids that may express more MMP, which possibly suggests the existence of “more invasive” phenotypes. This may be tested simply by increasing the treatment dose. Determining whether there exist observable morphological signs on organoids that can be correlated with a resistance to MMP inhibition could provide important information on the heterogeneity of the population. As a preliminary observation, a subpopulation of organoids appears to form structures with a high number of branches and/or branches remaining thin, well into the general Thickening phase compared to other organoids, which may reflect a more “mesenchymal” and invasive phenotype. A second hypothesis could be that local alterations in the microenvironment, such as denser collagen, may prevent the drug from reaching certain organoids, in a way similar to how the desmoplastic reaction in PDAC generates stroma that may prevent drug penetration. To test this hypothesis, an autofluorescent drug such as doxorubicin could be added to the medium to assess its penetration, as performed in other studies [75].

3.3.2 What drives the change in the molecular players of tension

While we have evidenced that the changes occurring in the expression of molecular players of tension was a driving factor in the apparition of buds, it remains at this stage unclear *why* these changes occur.

Hereafter, we discuss some of the mechanisms that could be at work, and experiments that may evidence them.

Maturation process. Cells could be undergoing a time-dependent maturation process, mediated by a biological clock (at the molecular, transcriptional and/or genetic level).

Clocks precisely regulating morphogenetic events do exist in biology, with the so-called segmentation clock, driving the formation of somites, being one of the most famous examples [122, 123].

A detailed analysis of the transcription profiles and of the proteomics of the system over time could potentially reveal the existence of morphogens controlling the timing.

Crossover. The minimal branching model described in 2.3 spontaneously exhibits a critical timepoint at which a crossover occurs in the competition between cell migration and the elongation-inhibiting proliferation processes, and where the Extension phase stops.

Similar mechanisms may be at play in the Thickening phase, that could trigger a switch in behaviour without requiring a molecular clock running.

Additional modelling efforts focused on the Thickening phase could possibly evidence such timescales.

Nutrient pressure. Nutrients could be another factor influencing the transition between the Extension and the Thickening phase.

Spheroid cultures for instance, classically display necrotic cores due to nutrient depletion, which limits their maximal size [102, 124, 125, 126].

This thesis has mainly considered experiments where multiple cells are seeded in culture wells, thereby giving rise to multiple organoids growing simultaneously in the dish, combined with stray cells that do not form organoids but rather develop as monolayers.

The combined metabolisms of these cellular structures could lead to a change of phenotype, where cells, sensing the limited availability of nutrients, would switch from an invasive, highly proliferative and expanding mode, to a stable, weakly proliferative one.

We note however that the medium was exchanged every two to three days, and that its Phenol red indicator never indicated signs of acidification or basification - remaining pink-red and never turning yellow or bright pink -, which would normally be observed in a starved culture.

As later described in the chapter dedicated to lumen formation (Chap. 4), organoids can display apoptosis in their core regions. It is however unclear whether this is due to starvation and insufficient nutrient penetration or due to other causes.

Perturbing cell-cell adhesion

We have used chemical inhibitors to perturb cell contractility, active cell migration, proliferation (Fig. 3.12), but not yet cell-cell adhesion which should play a pre-eminent role in our model of balance between extension and retraction processes (Fig. 3.8).

Monoclonal antibodies against E-cadherin such as ECCD1 [119] or HECD-1 [120] could be considered, to alter the levels of cell-cell adhesion.

According to our picture of balance between extension and retraction processes, lowering the level of cell-cell adhesion could *a priori* lead to the following scenarios.

3.3 Discussion: on budding

Absent cell-cell adhesion, branch cohesiveness might be lost or lowered, hindering the transmission of forces, and cells may keep migrating for a longer time than they would in untreated conditions, delaying or preventing the onset of the Thickening phase.

If cell contacts are disrupted by the inhibiting agents, branches may alternatively fragment in a fashion similar to when exposed to 250 μM blebbistatin (Fig. 3.13), as the tension of isolated cells might trigger their rounding up, if their phenotype does not revert to a more mesenchymal one.

3 Budding in pancreatic organoids

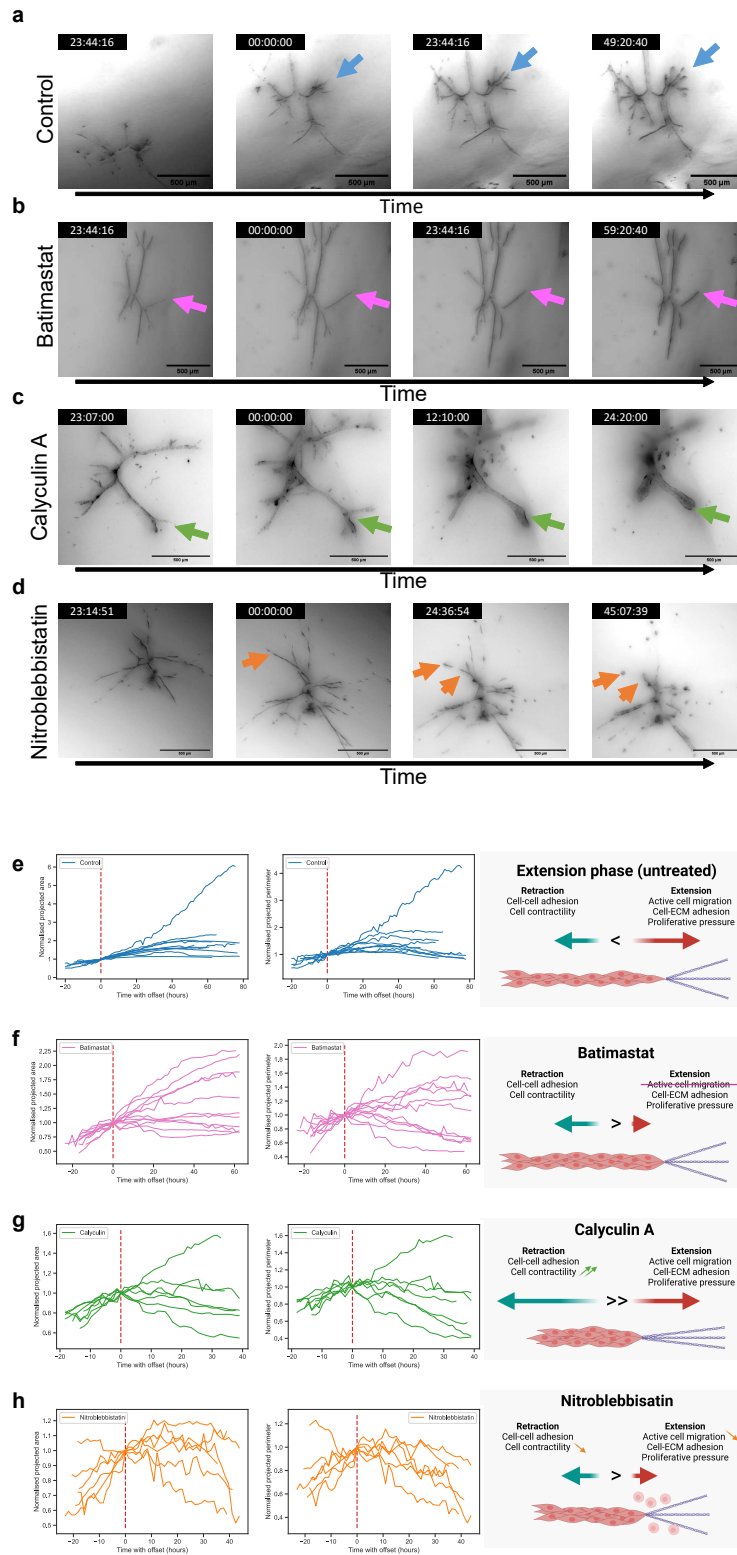


Figure 3.12: *Caption on the next page.*

Figure 3.12: **Perturbation experiments support the surface tension increase hypothesis.** All drugs are added during the Extension phase. **a** Untreated organoid during the transition from the Extension to the Thickening phase, displaying thickening branches and forming terminal end bud-like structures ($N = 10$ organoids). Arrows indicate a branch extending and then thickening and budding. **b** Treatment with $10\ \mu\text{M}$ batimastat stops branch extension and leads to tip rounding ($N = 11$ organoids). **c** Treatment with $0.5\ \text{nm}$ calyculin leads to branch retraction and tip rounding ($N = 7$ organoids). **d** Treatment with $50\ \mu\text{M}$ nitro-blebbistatin prevents branch elongation, and leads to tip rounding with fragmentation of the thinner parts ($N = 6$ organoids). In **b-d**, arrows indicate a branch extending pre-drug addition, that stops and thickens upon drug addition. **e-h** From left to right: evolution of the normalised organoid area, evolution of the normalised organoid perimeter, and schematic view of the corresponding alteration of the forces induced by the treatments, for each condition (top to bottom). Area and parameter are normalised with respect to the value at drug addition time in the plate (the normalised 00:00:00 timepoint), indicated by the vertical red dotted line. Scale bars: $500\ \mu\text{m}$. Microscopy images shown are bright field minimum projections. Schematics in **e, f, g, h** created with BioRender.

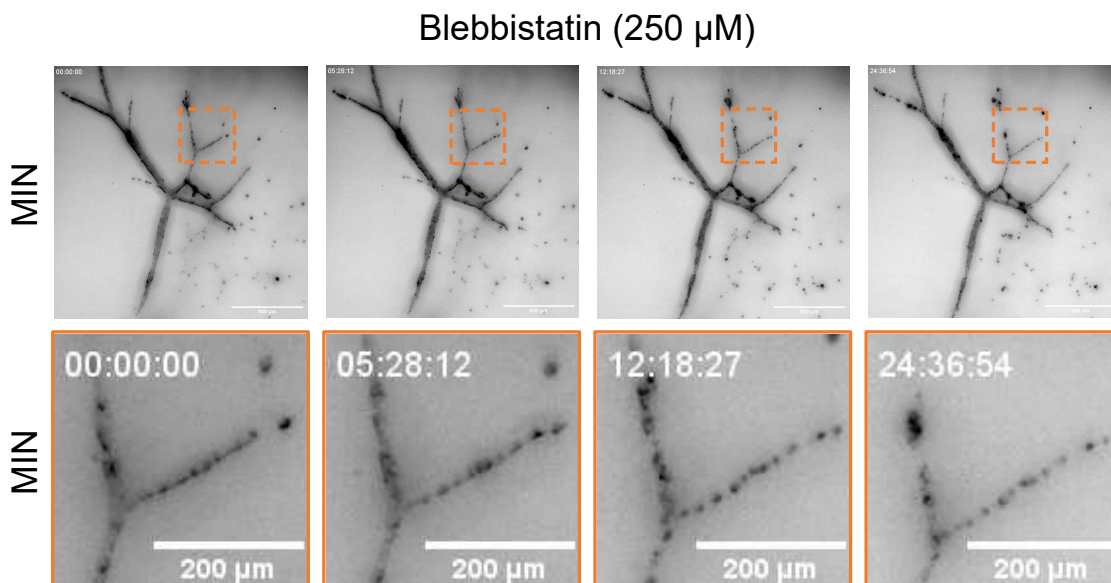


Figure 3.13: **Concentration dependency - Blebbistatin.** Exposure to $250\ \mu\text{M}$ of nitro-blebbistatin during the Extension phase prevents both the extension and the thickening of organoids, by forcing a loss of cohesiveness between the cells, which round up individually. Scale bars: top row $500\ \mu\text{m}$, bottom row $200\ \mu\text{m}$. Bright field images are all minimum projections.

4 Lumen formation in pancreatic organoids

4.1 Focusing on lumen formation - Rationale

We have shown in the previous chapters that branched pancreatic-cancer derived organoids could capture key morphological features of both the healthy and diseased pancreas, such as a branched architecture and terminal end bud-like structures.

The present chapter will focus on the processes of cavity formation (*luminogenesis*) that follow, and lead to the formation a lumen, resembling the hallmark of the functional pancreas and of its precancerous lesions, PanIN, IPMN and MCN.

We will show here that organoids display two orthogonal but complementary ways of forming a lumen: one of them relying on fluid intake for multiple microlumen nucleation, swelling and fusion, and the other one involving the death of a central cell population, thereby hollowing out a cavity.

We demonstrate that the architectural complexity of branched organoids, in combination with the relative ease of their experimental manipulability, allows the emergence and the real-time monitoring of the dynamics of those processes, rarely observed to be playing a role together within the same system.

These results shed further light on the processes of luminogenesis, and deepen our understanding of the early formation of PDAC precancerous lesions.

The results obtained led to a manuscript *Coexisting mechanisms of luminogenesis in pancreatic cancer-derived organoids*, in revision at the time of writing, authored with Marion Raich, under the supervision of Andreas R. Bausch, with the help of Dieter Saur for resources, and Maximilian Reichert for reviewing. Figures used in the submitted manuscript are marked with “Submitted for publication”.

4.2 Hypotheses for lumen formation in pancreatic organoids

4.2.1 Mechanisms of luminogenesis

Lumens, the cavities enclosed by biological tubes, are a major feature in numerous organs, allowing the circulation of crucial compounds through the organism, from arteries carrying blood, to the bronchi in the lungs carrying air, to the gastrointestinal tract carrying nutrients. Lumens are also a major feature of exocrine glands, such as the salivary glands, the mammary glands, or the exocrine pancreas, allowing the proper shuttling of the glands’ products to the target site. In these physiological examples, form is determinant for the proper function of organs.

However, lumens can also emerge in the context of diseases such as cystic fibrosis [127], or in PDAC, where lesions can involve ducts (PanIN, IPMN) and generate large cysts

4 Lumen formation in pancreatic organoids

(MCN) [5, 70]. In the case of diseased organs, the notion of “functionality” for lumen becomes unclear, but their form still emerges as a consequence of pathological processes that provide important insights on the disease [18].

Studying processes of luminogenesis is thus of great importance for both healthy and diseased tissues. Hereafter, we introduce a non-exhaustive list of processes and elements known to contribute to luminogenesis, as an illustration of the diversity of mechanisms observed. Reports have evidenced that the formation of biological *de novo* lumens from rod-like structures often involves one of two classes of processes: processes that rely on cellular rearrangements, without cell death to generate a lumen, and processes that rely on cell death to clear a space inside the rod-like structure to transform it into a tube [33, 49, 128].

The zebrafish for instance, offers numerous examples of cell death-free luminogenesis. In the developing zebrafish pancreas, the hepatopancreatic ductal system transitions from a solid rod-like state to a mono-layered epithelial duct, through a *de novo* lumen formation involving cell rearrangement and cell shape change, without cell death [129].

The lumen of the zebrafish gut form through an accumulation of fluid, mediated by claudins - a family of tight junction proteins -, and Na^+/K^+ -ATPase - that creates an electrochemical gradient allowing the intake of fluid [130].

In the case of the inner ear, the lumen forms as forces generated by mitotic rounding combine with fluid transfers from the epithelium lining to nucleate and fuse cavities [131].

Without a mechanically favourable environment, *e.g.* when cells maintain strong adhesion sites between them pre-lumen formation, fluid can also play an active role in remodelling the architecture of a tissue. In the mouse embryo, pressurised fluid has been reported to fracture the basolateral sides of cells, creating microlumens that further coarsen to form the blastocoel [132].

Lumens can also emerge from the restructuring of the plasma membrane(s) of cells, in particular through the production of apical membrane vesicles, as evidenced in the *C. elegans* secretory cell [133]. Tube formation begins with polarisation that positions the site of the future lumen, before the membrane material reaches the site, organises, and undergoes maturation before terminating [49].

In contrast, the mouse salivary [32] and mammary [50] glands *in vivo*, or 3D mammary acini structures *in vitro* [134], generate a lumen through apoptosis. Crucially, this cell death does not appear to be the consequence of incidental poor access to nutrients, but is rather a full-fledged morphogenetic program for lumen opening [134].

Rarely, systems such as 3D MDCK cysts, have been reported to switch between non-apoptotic and apoptotic mechanisms to form lumens, when their culture conditions are heavily modified (depending on whether they were grown in Matrigel or collagen, and depending on whether cell polarity was promoted) [135].

Polarisation of the tissue can play an important role in fashioning the lumen. In the case of membrane vesicle-based mechanisms, polarity allows the proper directing of vesicle traffic toward the apical side [49, 128].

Interactions between cells and the ECM *via* integrins, transcellular proteins responsible for cell-ECM, have been shown to mediate polarisation, particularly through their

interplays with GTPases : in MDCK cysts, the RhoA-ROCK I-myosin II pathway has been shown to control the orientation of polarity [136], whereas in endothelial cells, Cdc42 and Rac1 GTPases play a major role in lumen formation [137].

The RhoA GTPase is also found to be necessary in the *Drosophila melanogaster* trachea formation, where it mediates the formation of E-cadherin contacts between cells to remodel the apical surface and allow lumen formation. [138, 139].

In 3D MDCK cysts, a combination of Rab-family proteins, Cdc42 and the Par3-aPKC complex leads to polarisation and the formation of the Apical Membrane Initiation Site (AMIS) and the Pre-Apical Patch (PAP) sites, that later give rise to the lumen [140, 141].

Figure 4.1 presents some common mechanisms of luminogenesis in a schematic view.

4.2.2 A Physics view of lumen formation

The role of forces

Considering the experimental diversity of organisms, processes, and molecules for luminogenesis, could physical modelling provide a degree of abstraction that could evidence minimal sets of mechanisms to build a cavity, and that could be leveraged for quantitative descriptions and predictions?

To model luminogenesis from a Physics point of view, one can consider the possible forces exerted during the process. The interested reader may consult the excellent reviews of Navis, Nelson and Bagnat for a detailed overview of the matter [142, 143]. In general, these forces can be generated by cells in the tissue as they remodel - or are being remodelled - and by the fluid in the lumen that creates both hydraulic and osmotic forces.

For lumens forming through tissue rearrangement, forces are required to deform the cells that will become the epithelium lining the cavity. The formation of the salivary gland tube in the *Drosophila* embryo provides an example of multiple rearrangements driven by actomyosin. There, the tube forms through the invagination of cellular placodes in a pit, where cells undergo apical constriction close to the pit - also driving passive intercalations -, and active intercalations away from it [144]. Apoptotic cells may also generate forces (so-called apoptotic forces) that deform their surrounding epithelium by generating an apico-basal myosin II cable that pulls the neighbouring apical surfaces upon cell death [145].

In addition to the intracellular forces generated by actomyosin, the fluid accumulating in the lumen generates hydrostatic pressure through its action against the membrane, which is reflected by Laplace's law (Eq. 4.1) [146]:

$$\Delta P = \gamma \left(\frac{1}{R_1} + \frac{1}{R_2} \right) \quad (4.1)$$

where ΔP is the Laplace pressure (i.e. the difference of pressure across the interface, exterior pressure minus interior pressure), γ is the surface tension, and R_1 and R_2 are the principal radii of curvature. In the case of a sphere, where $R_1 = R_2 = R$, we get

$$\Delta P = \frac{2\gamma}{R} \quad (4.2)$$

Simultaneously, the fluid inside lumens is often not pure water but rather contains a mixture of solutes such as ions and proteins, which, when at a concentration different from the outside, contributes to creating a motion of water from the low concentration to the high concentration side, which is reflected by van't Hoff's law

$$\pi = iRTc \quad (4.3)$$

with π the osmotic pressure, i the van't Hoff factor, R the ideal gas constant, T the absolute temperature, and c the molar solute concentration [146]. Fluid exchanges can there occur through paracellular (going between the cells) and transcellular routes (going through the cells), *via* passive or active processes [38, 146].

We note that while these processes contribute to form and expand the luminal cavity by drawing fluid, they can also further affect the cellular and tissue properties through mechano-hydraulic coupling altering the tension, the shape or the motility of cells [146].

Lastly, evidence of the role of electrostatic forces in lumenogenesis is emerging. For instance, negatively charged sialomucins present on the surface of endothelial cells may contribute to tube formation in blood vessels through electrostatic repulsion [147, 148].

Physical modelling of the system

Analytical and simulation modelling can then be performed, by accounting for these phenomena.

Dasgupta and colleagues have for instance proposed an analytical model of intercellular lumen growth, between two cells, considering the active and passive transport of ions, the passive transport of water *via* hydraulic and osmotic effects, the mechanical contribution of actomyosin distribution, as well as an additional term accounting for leakage along the cleft [149].

Despite the relative simplicity of the system modelled, analytical treatment can already provide¹ important insights. The model for instance predicts a transition between monotonous and oscillatory modes of growth depending on pumping efficiency, and requiring cortical tension to vary in time rather than be fixed.

Simulations can further allow the “weighing” of processes’ contributions against each other, and reveal underlying physical mechanisms. In the case of a multiple lumen system transforming into a single-cavity Le Verge-Serandour and Turlier have evidenced through numerical simulations that a chain of microlumens could coarsen (and/or coalesce)² in a self-similar fashion, following a scaling exponent [150]. This coarsening/coalescing process is driven by hydraulic fluxes existing due to the differences in pressure between the microlumens. Surprisingly, the authors show that the passive differences in osmolarities between the different microlumens do not strongly impact the dynamics of coarsening.

¹At the cost of occasionally fairly involved equations.

²*Coarsening* is defined by the authors as the process where a lumen empties into another, whereas *coalescing* is defined as two lumens merging.

In contrast, active pumping could alter the mode of single lumen formation by promoting a coalescence process, with a separate scaling exponent. Active pumping was also shown to be theoretically capable of spatially biasing the position of the final lumen, which could represent a novel mode of symmetry breaking.

Crucially, these theoretical efforts can yield “phase diagrams” that should be capable of predicting general trends beyond the precise parameters that characterise a single particular experimental system.

Numerical implementations

Implementing tractable simulations is however in itself a challenge. Fuji, Tanida, Hiraiwa and colleagues have written a review of common schemes, along with their respective strengths and weaknesses [151], that we briefly reproduce here.

A first option is to consider a simple lumen morphology (spheres, ellipsoids, etc.), described by a few variables, greatly simplifying the analytical work, and allowing the feasible writing of mechanical balance and conservations laws, and the analytical derivation of steady state equations, as is done for instance in [149] or [150]. The main drawback of this scheme is its limitation to simple shapes, precluding the apparition of more complex morphologies.

A second option leverages vertex models, which represent the cells as three-dimensional polyhedra (or two-dimensional polygons in the simpler version), with tracked vertices moving to minimise a potential function (frequently a surface energy and an interface elastic energy) defined according to the specifics of a system, leading to a rearrangement of junctions, as performed in [152] or [118]. A lumen enclosed within a three-dimensional tissue can then be represented by one or several polyhedra, and possess its own elastic energy term. Those models remain computationally tractable, can sometimes be treated analytically, and can take into account as needed the forces exerted by/in junctions between cells. However, most 3D vertex models assume polyhedra with flat faces, whereas cells in tissues regularly display curved surfaces. The so-called “bubbly vertex model” proposed by Ishimoto and Morishita is a notable attempt at accounting for those more realistic curved shapes [153]. The second important drawback lies in the difficulty of reconciling the discrete computations of vertices positions with continuous variables such as the concentration of *e.g.* osmolytes in solutions, which limits the effects that a vertex-based scheme can model.

A third option can be to consider continuum models such as phase field models. This scheme considers a so-called phase field $u(\vec{r}, t)$ with \vec{r} the space and t the time, with the shape of each cell i described by the component u_i , where $u_i = 1$ inside a cell, and $u_i = 0$ outside. The field evolves over time to minimise a free energy, generally dependent on the shape of the cell, the interactions between cells, and the interactions between cells and external substances, which can be adapted as needed to the particulars of a system. Detailed mathematical formalism can be found for instance in the work of Nonomura for multicellular systems [154], and has been applied to describe the formation of single- or multi-lumens cysts [155]. The main benefit of such models lies in their ability to represent arbitrary cell-shapes and in the possibility to account for continuous variables

such as the luminal pressure or the distribution of molecules and proteins which may influence the dynamics of the system. However, numerical simulations of this model require a mapping of the space with a grid, which increases the computational costs the finer it gets.

Lastly, the Cellular Potts Model is a fourth option that can be considered for modelling. Here, in a generalisation of the Ising spin-model, a lattice is constructed, and a multi-state vector is positioned on each point, that can represent cells, the ECM, a lumen etc. Each point interacts with its neighbours, and the algorithm evolving the system aims to minimise the total energy (expressed as a Hamiltonian) of system, while allowing for thermal fluctuations. The interactions between neighbours can account for numerous effects such as *e.g.* cell-cell interactions, volume constraints, or signalling. Due to the nature of the Hamiltonian, new types of interactions can flexibly be added to the system, and, provided a fine enough lattice, complex shapes can be modelled. However, interfaces can be sensitive to fluctuations due to the lattice-based nature of the modelling.

4.3 Results

4.3.1 Different phenotypes of lumens suggest different processes of luminogenesis

We reported in Chapter 2, section 2.2 that branched organoids developed a single seamless lumen connecting the network of branches. Using high-content long-term imaging to observe organoids prior and during their lumen formation phases, we identified that the endpoint macroscopic lumen emerged from two types of microlumens, that appeared distinct from each other in transmitted light microscopy (Fig. 4.2a-b,d-e).

A first type of microlumen, dubbed “clear microlumens”, appeared highly translucent in bright field microscopy, in contrast to a second type dubbed “dark microlumens” which appeared much less translucent and filled with cells or debris.

We found that organoids could display one type of microlumen preferentially upon lumen formation, with 28.07% of organoids exhibiting a “Clear” phenotype and 47.37% exhibiting a “Dark” phenotype (N = 57) (Fig. 4.2g). Remarkably, we also found that 24.56% of the organoids displayed a “Mixed” phenotype with both clear and dark microlumens visible (Fig. 4.2c, f-g).

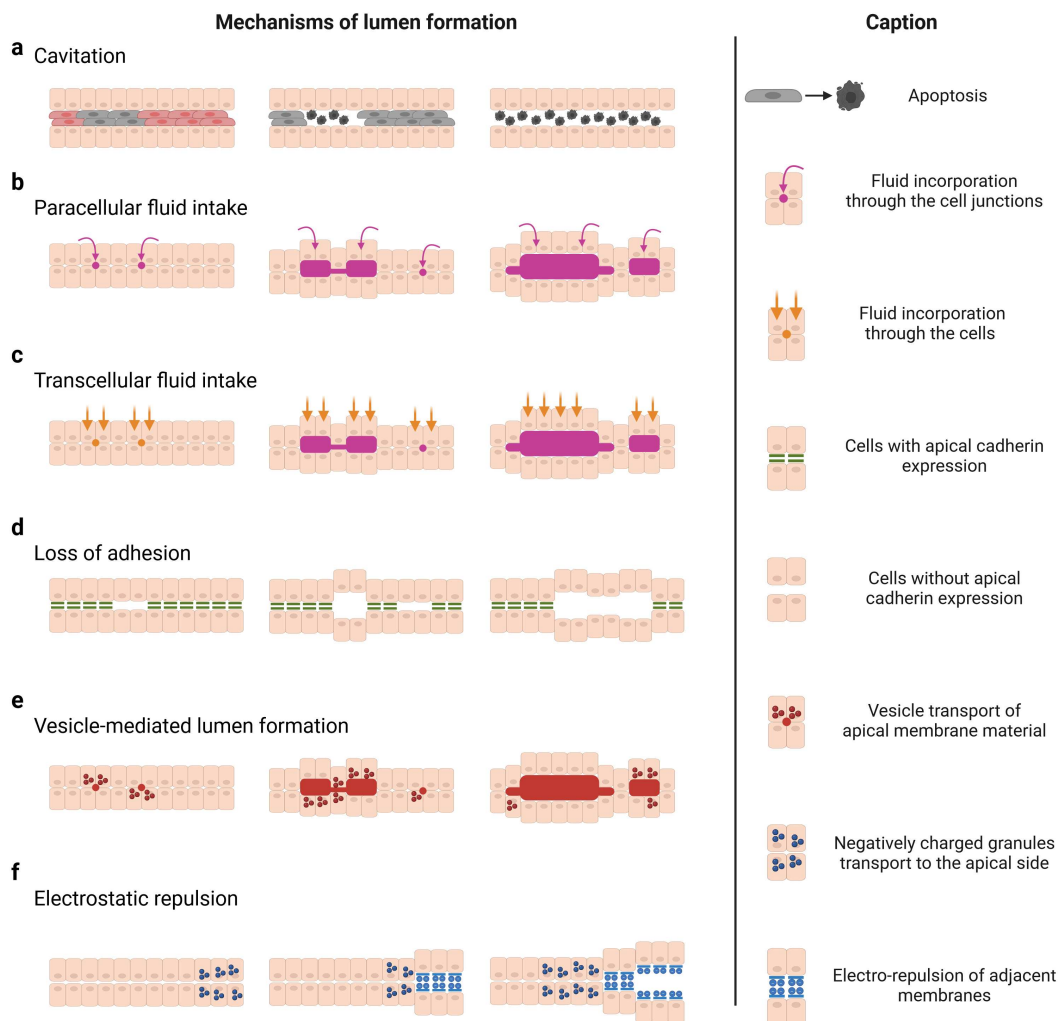


Figure 4.1: **Schematic view of known processes of lumen formation.** For simplicity, all lumens are represented as forming in an organised epithelium. **a** During cavitation, cells at the centre of a cell mass undergo apoptosis and are eliminated. Fluid from the outside can be transferred to the apical side by going through the cell-cell junctions (**b**) or directly through the cells (**c**). **d** Adjacent cells can separate in the case of loss of expression of adhesion molecules (e.g. cadherin) at the apical side. **e** Vesicles containing liquid and membrane molecules can be shuttled to the nascent apical site and provide material for lumen initiation and expansion. Note that this phenomenon can occur at the interface between cells or within cells (see [49]). **f** Upon deposition of similarly charged molecules (e.g. negative mucins) at the apical side of membranes facing each other, electrostatic repulsion can repel the opposing membranes and form a lumen. Created with BioRender.

In light of these different microlumen phenotypes, we set out to investigate whether different luminogenesis mechanisms were involved.

4.3.2 Fluid-based lumen formation: a focus on clear lumens

The translucent appearance of clear microlumens led us to hypothesise that a fluid intake-based mechanism could be driving the nucleation.

Clear microlumens nucleated at different points in space and time in organoids, and progressively increased in size (Fig. 4.3a). Using live imaging, we tracked the swelling profile of nucleating cavities and already established swelling cavities at the time of recording start (that we respectively classified as “Nuc” and “Swe” lumens in Fig. 4.3c, c’ and Fig. 4.6a, see Methods for the type classification).

We measured comparable median swelling rates of respectively $719 \mu\text{m}^2/\text{day}$ and $792 \mu\text{m}^2/\text{day}$ for both nucleating and swelling lumens. Following nucleation, neighbouring microlumens could fuse together, thereby forming a larger cavity (Fig. 4.4), eventually connecting every branch of the organoid together

Live imaging further revealed that this mechanism of clear lumen formation, in addition to contributing to microlumen nucleation, could also form large macrolumens in a subpopulation of organoids which displayed a “blowing up” behaviour (5/57 lumen-forming organoids = 8.77%, Fig. 4.3b).

“Blowup” phenotypes exhibited rates of area expansion superior by an order of magnitude to the rates of non-blowup phenotypes, reaching a median rate of $9919 \mu\text{m}^2/\text{day}$, despite organoids of both types being morphologically similar pre-lumen formation (Fig. 4.3c”, c’’’).

From a translational perspective, it thus appeared that non-blowup phenotypes were morphologically closer to PanIN precancerous lesions, whereas blowup phenotypes were architecturally reminiscent of other lesion types such as IPMN or MCN which involve larger duct dilation [5, 70].

To probe the influence of fluid intake in clear lumen nucleation and growth, we used ouabain (Tocris #1076/100) a Na^+/K^+ -ATPase inhibitor [119, 130, 132]. We observed that applying ouabain before any nucleation event could prevent lumen formation in organoids (Fig. 4.3d-f). However, organoids that had already started nucleating clear or dark lumens could pursue their process of luminogenesis (Fig. 4.3e, Fig. 4.6b-c). This suggests that Na^+/K^+ pumps play a major role in enabling nucleation events, with a decreased importance in lumen growth post-lumen formation. Conversely, treatment with forskolin, a drug known to activate the cAMP-PKA pathway and phosphorylate Cystic fibrosis transmembrane conductance regulator (CFTR) [83, 127] triggered Cl^-/Na^+ influx and promoted the formation of cystic organoids (Fig. 4.4b-c) and prevented the formation of branches when added at day 0. A regulated intake of fluid, temporally and in magnitude, therefore seems key to the formation of branched organoids possessing a single lumen.

Adding fluorescently-labelled dextran (3000 MW Alexa 488, anionic, D34682 Thermofisher) to the medium during the lumen formation phase revealed an accumulation of dextran at the cell-cell junctions and an uptake in the cavities, indicating a contribution

of paracellular intake to luminogenesis (Fig. 4.3g).

In addition to this transversal route of fluid intake, we also noted transfers of fluid along central fault lines in the branches, from established cavities, contributing to the apparition of microlumens and to the elongation of existing lumens. These transfers led to separation of adjacent cells along the longitudinal axis, in a manner highly reminiscent of hydraulic fracturing, with fluid propagating through cracks leading to cavity formation [156].

4.3.3 Cell death-based lumen formation: a focus on dark lumens

The presence of cells and debris inside the dark lumens, which contribute to the lowered translucency compared to clear lumens, suggested that cell death could also contribute to lumen formation.

To probe this, we used fluorescent reporters of caspase-3 (and 7) activity (#10402, #10406 Biotium) and live imaging of organoids during the Thickening and the Lumen Formation phase.

The increasing cleaved caspase-3 signal visible in the centre of branches and in the core of organoids prior to lumen formation, revealed that the observed darkening was correlated with multiple cell death events, occurring “in-place” (*i.e.* without extrusion) at a rate of around hundreds of cells per day (Fig. 4.5b-c).

Furthermore, the position of apoptotic cells, located between the columnar cells forming the epithelial lining of the future lumen, correlated with the position of longitudinally-elongated cells surrounded by cells displaying an increasing apical E-cadherin signal during the Thickening phase (see Chap. 3 and Fig. 3.5). Future work will need to determine whether there exists a direct causality link between the increased E-cadherin signal and the apoptotic events. This signal could for instance indicate crowding, known to be responsible for cell elimination [157], and/or increased stress (and strain) on the central cells that could be transduced into apoptotic signals by mechanosensitive channels [102, 158, 159].

Crucially, we found that clear lumens displayed little-to-no cell death events during luminogenesis (Fig. 4.6c) These observations suggest that hollowing organoids *via* cavitation constitutes an orthogonal but complementary mechanism of lumen formation in PDAC organoids.

Post-lumen opening, we could evidence further cell death events, resulting this time from elimination events that could occur both in the apical direction (Fig. 4.5d) or in the basal direction (Fig. 4.5e, which could be observed even when an apical lumen was open, as shown in Fig. 4.6e).

Due to the plateau observed in the number of cells in organoids during the later stages of development, and the decrease in the number of cells positive for Ki-67 (Fig. 2.10c-e), we suggest that the post-lumen formation cell elimination events could be contributing to tissue homeostasis.

4.3.4 Epithelialisation and polarisation: a focus on the centre of the branches

Transforming branches from a solid rod shape to a hollow one, positioning the future lumens, separating the adjacent cell walls, and maintaining the tissue integrity upon fluid intake involve important changes in the expression and distribution of tissue mechanics-, cell-cell adhesion-, and cell polarity-associated proteins.

We particularly focused on the centre of branches as it stood as the location of fault lines and targeted cell death.

First, we investigated the state of actomyosin, as one of the major actor and hallmark of tissue mechanics. Immunostainings and live imaging revealed high levels of F-actin and non-muscle myosin IIa on a central longitudinal line in branches pre-lumen nucleation (Fig. 4.7a-b, Fig. 3.4). During lumen nucleation, the signal intensity for F-actin remained high at the apical side, providing a clear delineation of the cavities, whereas the non-muscle myosin IIa signal decreased.

Second, we sought to determine if clear cavity nucleation, involving the separation of adjacent cells in the centre of branches, followed a complete loss of cell-cell adhesion, or whether fluid intake could overcome the resistance of preserved adhesion sites. Using a cell line expressing endogeneously-labelled E-cadherin³, we found that cells progressively adopted an epithelial columnar shape and exhibited an increasingly strong E-cadherin signal, notably at the future apical side (Fig. 4.7c-d). In branches thicker than two cells-wide, the central cell population was surrounded by an intense E-cadherin signal, correlating with the position of cells later eliminated by apoptosis during dark lumen (Fig. 4.7e). During lumen nucleation, we observed that instead of a complete loss of apical E-cadherin signal - that could precede and enable cell separation due to loss of adhesion -, E-cadherin was rather displayed inhomogeneously at the apical side, with cells either maintaining a signal or individually losing it (Fig. 4.7e). Upon lumen expansion, cells facing the cavity all gradually lost their apical signal, while maintaining their basal and lateral expression (Fig. 4.7e). This disappearance of apical E-cadherin could be the consequence of a recycling process triggered by the loss of cell-cell contacts at the apical side as the lumens open [160], and a result of PKC family protein-mediated endocytosis of cadherin [161]. Further investigation at high spatial and temporal resolution of E-cadherin dynamics may therefore prove critical for our understanding of the luminogenesis process.

Third, we investigated whether cell polarity was established, corroborating the observed asymmetry in E-cadherin distribution, by determining an apico-basal identity and enabling directed processes such as protein transport [49]. We focused on the spatiotemporal distribution of PKC- ζ , an isoform of aPKC, reported to be a crucial marker and player in the establishment of polarity and luminogenesis across numerous systems, such as the mouse embryonic pancreas [44], the zebrafish gut [130], or MDCK cysts [141]. Pre-lumen nucleation, no specific organisation of the PKC- ζ could be detected (Fig. 4.7e). Upon microlumen nucleation, we evidenced a strong apical PKC- ζ signal lining the cavities, which was maintained as lumen expanded in size (Fig. 4.7e). These

³A kind gift of Prof. Dieter Saur

observations indicate that polarisation is a gradual process, with visible apical actomyosin accumulation at the fault line, preceding lumen formation, and PKC- ζ polarisation appearing concomitantly to cavity opening.

To probe the role of actomyosin on lumen formation we used chemical inhibitors, added during the transition between the Thickening and the Lumen formation phases (Fig. 4.7f-j).

To assess the effects of increased cortical contractility, we used the myosin phosphatase inhibitor calyculin A (Thermofisher PHZ1044) [117, 118, 119]. Similarly to the results reported in Fig. 3.12c, g (where the inhibitor was added at the Extension stage), we found that in organoids with branches still elongating, extension stopped following drug addition, and that thin branches retracted and started forming bud-like structures (Fig. 4.7h). The retraction of branches could lead to a rupture between cells at the tip, attached to the collagen fibres at the front, and cells in the stem of the branch, retracting through the collagen path carved (Fig. 4.7h), was evidence of an increased contractility. Despite this perturbation, organoids largely remained capable of lumen formation (Fig. 4.7f-g, Fig. 4.8a-a').

Aiming to probe the opposite effect of decreased cell contractility, we sought to interfere with myosin activity by using nitroblebbistatin (Santa Cruz Biotechnology sc-212797) a myosin II ATPase inhibitor and ML7 (Santa Cruz Biotechnology sc-200557) a myosin light chain kinase inhibitor [52, 119, 129, 162]. Blebbistatin directly inhibits binding of non-muscle myosin II to actin, while ML7 indirectly interferes with non-muscle myosin II by the inhibition of the myosin light chain kinase activity, blocking the phosphorylation of the regulatory myosin light chains [163, 164, 165].

Blebbistatin treatment led to a marked decrease in lumen formation capability (Fig. 4.7f, Fig. 4.8b), especially in the case of organoids which did not already display some cavities at drug addition time (Fig. 4.7g, Fig. 4.8b'), stressing the importance of myosin activity for lumen formation for PDAC organoids. Thin branches still existing at the Thickening to Lumen formation stage exhibited fragmentation, as was the case when blebbistatin was added at the Extension stage (Fig. 3.12d, h, Fig. 3.13).

Treatment with ML7 (from 10 μ M to 50 μ M) however did not lead to a marked inhibition of luminogenesis, with the observed proportion of non-lumen-forming organoids being comparable between the treated and untreated conditions (Fig. 4.7f-g, Fig. 4.8c-c'). Other upstream factors, independent of the myosin light chain kinase, could thus be active during lumen formation in PDAC organoids, as has been reported in studies investigating the RhoA activity in the healthy pancreas development [52]. While not a luminogenesis inhibiting effect, we observed that treating organoids forming clear lumens with ML7 led to a rapid darkening of the cavities due to massive cell release and death at the apical side (Fig. 4.7j), reminiscent of results reported in the context of endothelial luminogenesis perturbation [166].

4 Lumen formation in pancreatic organoids

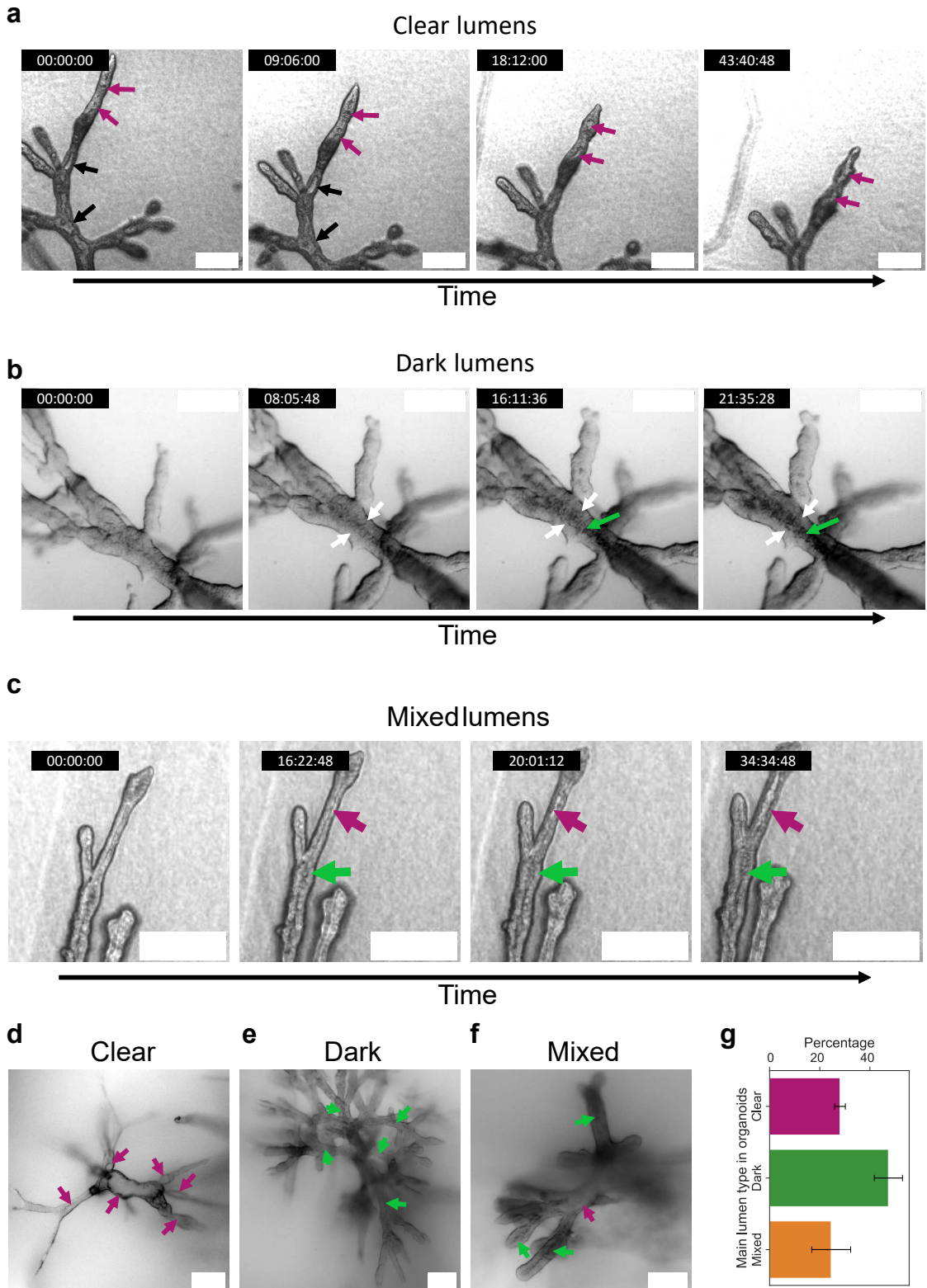


Figure 4.2: *Caption on the next page.*

Figure 4.2: **Coexistence of clear and dark lumens** **a** Close-up view of branches displaying the formation of so-called “clear” lumens, cavities highly translucent in bright field microscopy. Black arrows indicate cavities that had already nucleated and swollen before observation started, while magenta arrows indicate cavities newly nucleated. **b** Close-up view of branches displaying the formation of so-called “dark” lumens, cavities poorly translucent in bright field microscopy. White arrows indicate the epithelial-like wall surrounding the lumen, while green arrows indicate the core of the branch, progressively becoming darker and eventually giving rise to a cavity. **c** Clear (magenta arrow) and dark lumen (green arrow) coexisting next to each other within a branch. **d** Entire organoid with predominantly clear lumens. **e** Entire organoid with predominantly dark lumens. **f** Entire organoid with both clear and dark lumens (resp. magenta and green arrows). **g** Average percentage of organoids with predominantly clear (N=16/57), dark (N=27/57), and mixed lumens (N=14/57 organoids). Error bars indicate the standard error of the weighted mean. Scale bars: 200 μm . Submitted for publication in *Coexisting mechanisms of luminogenesis in pancreatic cancer-derived organoids*.

4 Lumen formation in pancreatic organoids

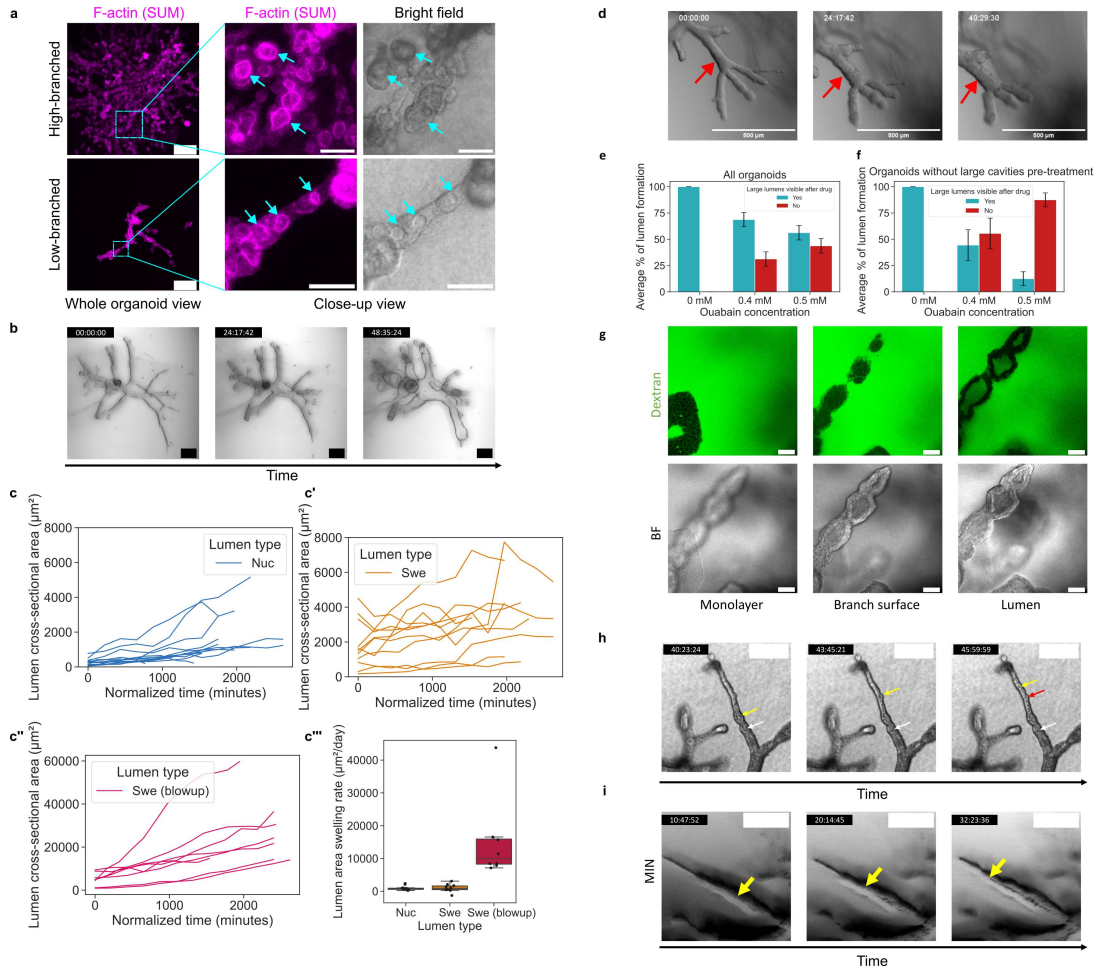


Figure 4.3: *Caption on the next page.*

4.4 Discussion: on luminogenesis

We found that both cell death-based and cell death-free mechanisms could give rise to different types of microlumens, so-called “clear” and “dark” phenotypes, that further expand, merge and converge towards similar structures of single seamless lumens. We note that PDAC organoids first displayed branches and then lumens, whereas, in the developing pancreas, the branched architecture emerges from the microlumens that form first [44]. In further contrast to the developing pancreas, where apoptosis could not be observed during the microlumen formation step [44], PDAC organoids did exhibit a cell death-based mechanism of lumen formation. Such differences may be expected when comparing a healthy and a pathological case, *a fortiori* when comparing them in an *in vivo* setting on one hand, and in an *in vitro* setting on the other hand. Noting those differences is however primordial to understand if and how cancer cells leverage

Figure 4.3: **Fluid intake and fluid transfer contribute to clear lumen formation.** **a** Phalloidin staining of high-branched and low-branched organoids with "clear" microlumens. Summed slice projection shows F-actin lining the microlumens as indicated by the blue arrows. **b** Organoid displaying an extreme cavity swelling behaviour during the lumen formation phase. Evolution of lumens' cross-sectional area over time in **c** "Nuc" (n = 14 lumens, N = 5 organoids), **c'** "Swe" (n = 11 lumens, N = 4 organoids), **c''** blowing up (n = 8 lumens, N = 3 organoids) cases, and estimated rates of swelling shown in box plots **c'''**. Tracks with fusion events between neighbouring cavities are excluded from the computation of the swelling rates. **d** Time-lapse showing that treatment with 0.4 mM ouabain at the Thickening stage, prior to lumen apparition, can prevent further lumen formation. The red arrow indicates the place where a lumen would normally have been expected to form in untreated conditions after more than 40 hours. Drug is added at timepoint 00:00:00, on a Day 11 organoid. Lumen formation post-treatment is quantified in **e** and **f**. **e** considers organoids both with and without already formed cavities pre-treatment (0 mM, N = 18 ; 0.4 mM, N = 16 ; 0.5 mM, N = 16 organoids), whereas **f** considers only organoids that did not display any lumen before treatment (0 mM, N = 8 ; 0.4 mM, N = 9 ; 0.5 mM, N = 8 organoids). Error bars in **e** and **f** indicate the standard error of the weighted mean. **g** Confocal slices showing Dextran Alexa 488 incorporated at the cell-cell junctions in a monolayer, at the branch surface, and inside the lumen. **h** Time-lapse showing the propagation of fluid along a fault line in a branch, in a process reminiscent of hydraulic fracturing. As it propagates, the fluid creates transient microlumens that grow then deflate. The white arrow indicates the position of the fluid's source, the yellow indicates the position of the currently growing microlumen, and the red indicates the position of a deflating microlumen. **i** Time-lapse showing the propagation of a fracture (yellow arrow), along the branch longitudinal axis due to fluid intake. Note that the minimum intensity z-projection causes the inside of the lumen to appear darker than it is in reality. Scale bars: **a** (whole organoid), **b**, **d**, **h**, **i** 200 μm , **a** (close-up), **g** 50 μm . Fluorescence images in **a,d,e**: confocal summed projections; in **f**: confocal slices. Bright field images in **a**, **d**, **g**, **h**: plane; in **b**, **i**: minimum projection. Submitted for publication in *Coexisting mechanisms of luminogenesis in pancreatic cancer-derived organoids*.

developmental processes to form lesions and tumours.

Previous studies had already evidenced the existence of lumen formation processes reliant on fluid intake [119, 130, 156], or on cell death [32, 50, 134], but rarely have the two mechanisms been observed to coexist within the same system, under the same culture conditions. A rare example reported in the literature is the case of the zebrafish inner ear, which was found to leverage both intra-organ fluid redistribution and mechanical

4 Lumen formation in pancreatic organoids

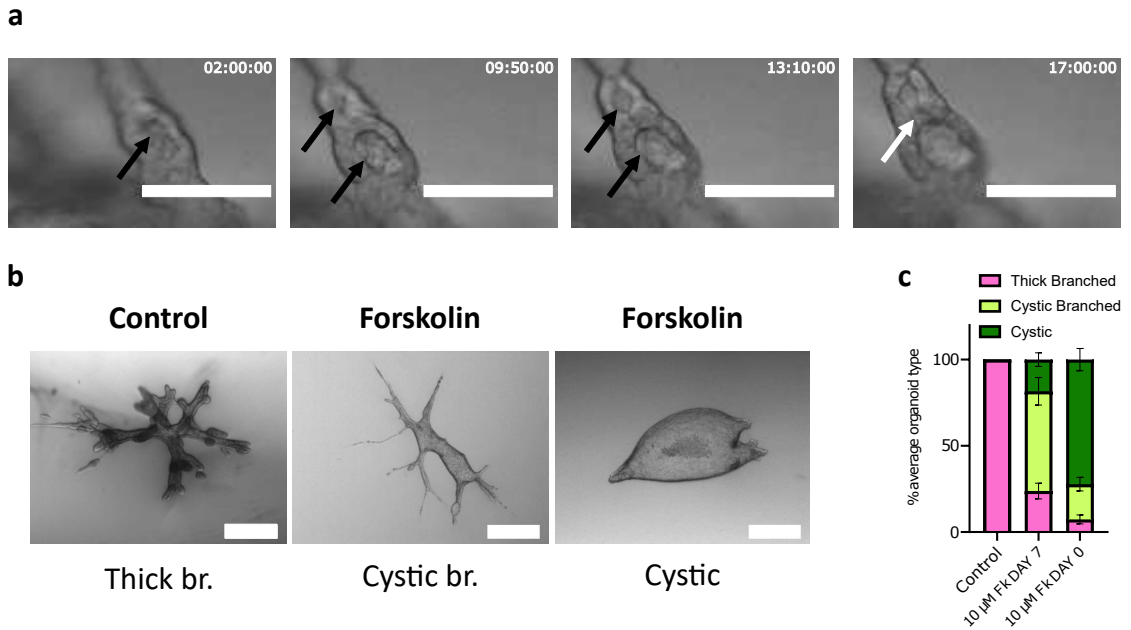


Figure 4.4: **Time-lapse of microlumen nucleation, fusion and influence of forskolin.** **a** The black arrows indicate existing microlumens undergoing swelling at Day 12-13. The two microlumens coalesce in a single lumen shown by the white arrow. **b** Day 13 organoids exposed to 10 μ M forskolin added at seeding time tend to develop cystic shapes. **c** Organoid phenotypes distribution at Day 13, according to the addition day of 10 μ M forskolin. (Control: $n = 159$, Fk from D0: $n=73$, Fk from D7: $n = 101$ organoids), mean \pm sem. Scale bars: **a** 100 μ m, **b** 500 μ m. Forskolin experiment by Aristeidis Papargyriou. Reproduced and adapted from [8].

contractions to form.

One may however ask if the coexistence of multiple luminogenesis processes is truly a rare occurrence, or only rarely observed due to limitations in the experimental systems.

Indeed, *in vitro* organoids studies have largely focused on spheroidal structures [93, 102, 103, 124, 167, 168, 169], which, while recapitulating key biological hallmarks, remain (over)simplified versions of the organ or tumour of interest, particularly from an architectural standpoint. Those simplified structures may thus lack the complexity that would allow multiple luminogenesis mechanisms to coexist.

Conversely, *in vivo* studies of entire organisms, while preserving the architecture of the organ of interest, may be faced with the opposite problem of an overwhelming complexity making it difficult to isolate the contributions of individual processes. Experimental imaging challenges, and off-target effects of chemical perturbations can further complicate the identification of mechanisms.

We argue in this thesis that architecturally-faithful organoids fill the gap between *in vitro* oversimplified structures and highly complex *in vivo* studies. Being architecturally

more complex than spheroids, branched PDAC organoids may display more than one dominant luminogenesis mechanism, while still remaining experimentally more tractable than a whole organism, permitting the disentangling of multiple processes' contributions.

The heterogeneity in branched organoids structures, while often thought of as a drawback [15], can instead be leveraged as a tool to understand how a particular lumen formation process might become dominant over the other, or in which conditions both cell-death-based and cell-death-free processes can coexist.

From a molecular standpoint, we found that the cell rearrangements leading towards the apparition of a lining epithelium were correlated with actomyosin dynamics, suggesting an important role for force generation.

Supporting this hypothesis, the perturbation of myosin activity with blebbistatin (Fig. 4.7f-g,i, Fig. 4.8b-b') led to a reduction in the lumen formation efficiency. Reports in the developing embryonic murine pancreas [52], or in the zebrafish hepatopancreatic ductal system formation [129] have evidenced that blebbistatin could perturb proper lumen formation, causing disruptions, gaps, and loops in the luminal network. The specific action of myosin II in PDAC organoid luminogenesis, among its many identified roles [110, 136, 170, 171], still remains unclear at the stage of writing. Its reported function in driving cell shape changes and rearranging cells [129], may prove to be crucial in light of the epithelialisation and polarisation that we observed during the transition between the Thickening and the Lumen formation phases (Fig. 4.7a-e).

Upon lumen opening, the non-muscle myosin IIa appeared to decrease, possibly indicative of a reduction in actomyosin active stresses [171], whereas at the apical side, the important presence of F-actin may reflect a stabilisation role for actin in the lumen, allowing the accumulation of fluid while preserving tissue integrity.

Crucially though, neither of the calyculin, nitroblebbistatin or ML7 treatments led to the collapse of pre-existing lumens upon drug addition, suggesting that once lumens are established, cortical tension is not the sole component responsible for lumen shape stability, corroborating results obtained in MDCK spheroids [172]. The formation of epithelial walls surrounding the cavity, the pressure of the incorporated fluid, or other features such as a possible preferred apical domain size [172], could contribute to withstand those treatments, and thus represent promising targets for future perturbation studies.

This study has, at the time of writing, not yet fully shed light on the role of PKC proteins (especially PKC- ζ) in organoids. Other studies however suggested that PKC- ζ could play a crucial role as an apical determinant, directing proteins precursors to microlumens [49].

For completeness' sake, we note that in our lumen formation inhibition experiment using ouabain to target $\text{Na}^+\text{-K}^+$ ATPase (Fig. 4.3d-f), we primarily sought to prevent fluid intake. However, some reports [119, 173] have evidenced that ouabain could also interfere with the formation and the function of tight junctions. It is therefore possible that the inhibition of lumen formation could be the result, not of cells being unable to bring fluid to the apical side, but potentially of cells being unable to keep fluid at the apical side, due to immature tight junctions. High-magnification, high-resolution imaging of cell-cell junctions would therefore prove valuable in following studies, in

4 Lumen formation in pancreatic organoids

conjunction with the imaging of potential para- and transcellular routes for fluid intake such as claudins [174] and aquaporins [175].

In addition to these dual mechanisms of lumenogenesis, we have also reported the existence of cell elimination events directed towards the basal or the apical sides. We suggest that these events contribute to homeostasis in the organoid tissue, following the apparition of the lining epithelium facing the lumens. Mechanically, the epithelialisation of cells, switching to a columnar shape, and enriched in F-actin and E-cadherin, should result in a stiff, crowded tissue, in which only one of two daughter cells can remain following a division event (Fig. 4.7a-b, e).

If the environment proves too stiff to be deformed by the forces generated during division, cells can undergo apoptosis if the mitosis is not cancelled, with a disassembly of the mitotic spindle and a re-integration of the chromosomes [176]. Crowding in tissues has further been reported to induce extrusion (or delamination) of live cells to maintain a constant cell number [157, 177]. Studying the precise timing and conditions of caspase activation in future experiments should therefore prove instructive. Lastly, E-cadherin can, at the molecular level, promote homeostasis through a reprogramming of the cell cycle and the cell migration properties [178]. This could contribute to explaining the decrease in the Ki-67-positive cell population that we reported, with cells in the thicker regions, notably the organoids cores, being the first to cease proliferating (Fig. 2.10 c-e). What, if anything, governs the direction of elimination, remains unclear at the time of writing. Investigating whether the apical-side release of dark cells that follows ML7 treatment (Fig. 4.7j) stems from mechanical changes in the tissue induced by the myosin light chain kinase inhibition and/or by the induction of apoptosis inside the luminal cavities [179] could offer some insights on the role of mechanics and signalling in cell elimination in organoids.

Studying the balance between the different mechanical components such as the cell contractility, the cell-cell adhesion and the cell-ECM adhesion could however provide a potential mechanics-based explanation.

While it remains difficult at this stage to identify in advance which type of lumen is going to be formed in an organoid, follow-up studies combining sequencing data with detailed live imaging of fluorescently-labelled proteins of interest and morphological criteria, may be able to determine a rationale.

We suggest that developing ways to access the content of organoids' lumens in real-time represent the next major step for our understanding the lumenogenesis process. Dynamic fluorescent sensors responding to changes in *e.g.* osmolarity or pH could allow a "contactless" observation of the luminal content, while careful microneedle insertion could allow the collection of internal fluid samples or the injection of perturbing agents. Alternatively, changing approaches and engineering the environment in the manner of a microfluidic chip with inlets and outlets for an organoid, as attempted by Eric Waschkau in his thesis [180], could allow accessing and manipulating the lumens [181, 182].⁴

Branched PDAC organoids thus constitute a promising system for the study of lumino-

⁴This however represents a change of philosophy, from self-organising organoids to designed organs-on-a-chip [183]

genesis processes and for the events that lead to the establishment and development of precancerous lesions.

4.5 Perspectives: post-lumen formation

This work has so far primarily focused on the mechanisms that lead to the formation of lumens, being one of the key morphological hallmarks of branched PDAC organoids.

As part of the perspectives for future research, we will briefly introduce here some phenomena of interest observed post-lumen formation. In particular, we will present some early findings on functionality in lumens and the formation of pearl-like structures.

4.5.1 Known roles of lumens post-formation in other systems

While this thesis is primarily focused on the processes of development that lead to lumen formation, it should be stressed that lumens, once formed, can in turn contribute further to developmental process, by providing and transmitting both mechanical (through hydraulics) and biological (through the transport or accumulation of molecules) cues. Chan and Hiiragi's have for instance reviewed this emerging role of lumens in signalling [184].

At the physical level, the build-up of fluid in the lumens leads to an increase in hydrostatic pressure which can further remodel the tissue by altering cytoskeleton properties. For instance, cystic domes growing from 2D cell layers have been shown to exhibit a property called superelasticity where, heterogeneously, some cells can undergo heavy deformations (up to a 1000 % change in area), while other cells do not deform, and tension at the tissue-level remain constant [185]. This behaviour is made possible as stretching - due to pressure increase - contributes to a dilution of the cytoskeletal components, which in turns leads to a softening of the cell. In the mouse blastocyst, the accumulation of fluid leads to an increase in cortical tension, which, leads to a maturation of the tight junctions, establishing a feedback loop that regulates the size of the embryo [119]. Through mechanotransduction, mechanical cues can thus be converted to biological signalling, via various players such as cadherins (with β -/ α - catenin and vinculin [111, 113, 186, 187]), integrins [188], stretch-activated channels such as Piezo1 [111, 157], or the YAP/TAZ proteins [189] to name a few.

In addition to their role in mechanical signalling, lumens can also serve as niches for biochemical signalling. To build the lateral line of zebrafish - a sensory system monitoring changes in the motion of water -, mechanosensory organs need to be formed periodically. This process occurs in a migrating epithelium - the primordium -, in which microlumens can develop, and locally concentrate the FGF morphogen, thereby sharply restricting its activity to neighbouring cells [190]. This group of cell affected by FGF signalling then stabilise and form the rosettes that constitute the sensory organs. Similarly, microlumens in the forming mouse blastocyst were shown to localise FGF4, and actively depositing this growth factor via injection in those cavities promoted cell fate specification [191].

4.5.2 Functionality in formed lumens

Could, and do, lumen play a role after their formation in organoids, or are they simply a topological feature that emerges from self-organisation processes? In the exocrine pancreas, lumens would normally functionally provide an avenue along which digestive enzymes could travel from the acini to the duodenum. We may then ask whether lumens in organoids could also potentially fulfil a transport role, despite organoids being closed structures without an “exit” toward which a putative molecule of interest could be shuttled. We will show below that, indeed, lumens could internally shuttle fluids and material, and present hallmarks of stability such as a mucin coating on the apical side, and a degree of retention of internal fluid.

Shuttling material

After lumen nucleation and initial swelling, and the connection of branches in the organoids, we sought to observe if lumens could potentially communicate between them.

We could observe events where in a “chain” of large cavities connected by clefts, fluid could propagate, as evidenced by the sequential swelling and deflating of lumens (Fig. 4.10a). Furthermore, by labelling cell nuclei using SiRDNA (Spirochrome SPY650-DNA SC501), we could detect that cells floating in the lumens - following cavitation or extrusion events - could also be shuttled from one spot to another (Fig. 4.10b). Dark lumens, despite initially containing numerous floating cells from the branch central population that detached from the lining epithelium, were also progressively cleared over time as cells degraded (Fig. 4.9).

As lumens emerge at different timepoints, newly forming cavities contribute to restructuring the existing hydraulic network and should therefore lead to a re-equilibration of the hydrostatic and the osmotic pressures. In addition, oscillations in the size of cavities, potentially triggered by local leakage [119, 168], could further trigger fluid exchanges in the network.

These observations indicate that, in addition to passive diffusion along the luminal network, faster fluid transfers may also contribute to the internal transport function of lumens. To further investigate this process, obtaining real-time 3D movies of the entire organoids with labelled particles in the lumens would allow the precise monitoring of fluid transfer dynamics.

Accumulating molecules

Although leaks may transiently occur in the organoids, lumen need to be capable of stably retaining most of their putative payload for them to be functional.

We have shown that dextran (3000 MW, Alexa 488) added in the culture medium could accumulate in lumens via a paracellular route (Fig. 4.3g).

We found that molecules of different sizes (3000 MW and 10000 MW) could accumulate stably in the lumen (Fig. 4.11a-b), likely due to tight junctions maintaining a degree of sealing from the inside to the outside (Fig. 4.11c).

By adding differently labelled dextrans at different timepoints, we found that lumens in the same organoids could locally accumulate different molecules, which could provide the possibility for cavities to act as niches for various growth factors (Fig. 4.11d), as was reported in other systems [184, 190].

Apical protection

Lastly, to perform their transport function, lumens may require a protective layer on their apical side. Indeed, in the exocrine pancreas, ductal cells secrete mucus in the lumen to prevent the digestive enzymes from damaging the organ [44].

To highlight the functionalisation of lumens, we examined the distribution of Mucin 1 (MUC1), a mucin known to play a key role in the protection of the lumen and its lining epithelium in the developing and adult pancreata, and a marker of precancerous lesions lumens [5, 46, 70, 192].

We report that pre-lumen formation but following cell epithelialisation and the apparition of a central F-actin fault line, MUC1 granules started to appear in cells (Fig. 4.12). At nucleation and upon lumen expansion, MUC1 could now be found at the apical side of microlumens, co-localising with the F-actin and correlating in space and time with the apparition of the PKC- ζ apical signals (Fig. 4.12b).

Importantly, the expression of mucin at the apical side was distinctly restricted to areas where lumen had already opened and polarised, suggesting that lumen formation is a prerequisite for mucin accumulation at the central side (Fig. 4.12d). Cyst-like organoids exhibited polarised lumens with strong apical mucin expression, resembling precancerous lesions such as large IPMN and MCN [5, 70] (Fig. 4.12e). We reported that the mucin 1 expression correlated spatially and temporally with the presence of PKC- ζ at the apical side, mimicking the lining found in PDAC precancerous lesions. While the relevance of MUC1 as a key clinical marker of PDAC is debated [192], it nonetheless remains an important luminal marker and an indicator of potential functionality [47].

Furthermore, mucins, bearing negative charges, were reported to initiate lumen formation in murine blood vessels [147], and in both human and mouse embryos [148], due to the electrostatic repulsion of adjacent cell membranes, potentially representing an additional mean of lumenogenesis for PDAC organoids. Probing this hypothesis could be realised in future studies by attempting to neutralise the charges borne by mucins, adding for instance protamine sulfate to the medium [147]. Another strategy to test the electrostatic repulsion mechanism could be to prevent mucin granule formation, by inhibiting interleukin-13 - known to play a major role mucin overproduction in asthma -, using a recently developed peptide called SP9 [193, 194].

4.5.3 Pearl-like structure formation

When grown for 24 days, we noticed that organoids occasionally developed pearl-like structures (Fig. 4.13).

While it remains unclear at the time of writing whether those peculiar shapes fulfil a biological role, those structures might provide important insights on the physical

properties of organoids and their evolution over time.

These observations of quasi-periodic structures appeared, at first glance, reminiscent of the so-called Plateau-Rayleigh instability (for short “P-R instability” also called “pearling instability”), named after the physicists Joseph Plateau [195] (after observations from Savart [196]) who experimentally reported on the instability of cylinders of fluids, and Lord Rayleigh who provided a mathematical description of it.

A daily occurrence of this phenomenon is for instance visible when the stream of water falling from a tap goes from a smooth column of fluid, to displaying “pearls” and eventually collapsing in droplets at its tip.

Fluid cylinders are indeed inherently unstable, and upon perturbation, pearling can manifest when the following criterion is matched:

$$\lambda > 2\pi r_0 \tag{4.4}$$

where λ is the wavelength of the perturbation on the fluid cylinder, and r_0 is the radius of the unperturbed jet. In this case, the perturbation can grow and lead to the deformation of the column of fluid, up to a critical point where it breaks in droplets.

For a complete derivation of this result, including the more involved calculus steps, the reader can refer to Chapter 23 of *Microfluidics: Modelling, Mechanics and Mathematics* by Bastian E. Rapp [197]. A further analytical and numerical study for the case of interfaces exhibiting anisotropies can also be found in the work of Graessel, Bächer and Gekle [198] for example.

While the initial observations and theory of the P-R instability came from a relatively simple system, namely a column of water either free-falling or projected as a jet in air [195, 196], the phenomenon has also been reported to exist in biological systems.

In 1994, Roy Bar-Ziv and Elisha Moses found that, upon perturbing a lipid membrane bilayer tube using optical tweezers, they could create an instability that propagated at constant velocity from the point of application of the tweezers, generating peristaltic shapes through a Plateau-Rayleigh instability [199]. Pearling could also appear in lipid tubes when anchoring polymers were added on their surface [200].

The P-R instability could also be found in cells and in tissues. Cells treated with Latrunculin A (LatA), an actin-disrupting drug, exhibited numerous radial protrusions at low LatA concentration, and displayed pearling when the LatA concentration was raised [201]. This phenomenon was, for its linear regime, explained through a competition between the rigidity of the actin skeleton (lowered upon exposure to LatA) and the tension to which the protrusions are subject (arising from adhesion to the substrate or ECM). In blood vessels, treatment with angiotensin II, a vasoconstrictive agent, was shown to generate periodic peristaltic shapes⁵[202]. This process was reversible, and removing the drug caused the blood vessels to recover they normal cylindrical aspect. From a translational perspective, this example is particularly enlightening, as it demonstrates that in the case of hypertension, abnormal vessel shapes may emerge not due to the high blood pressure mechanically deforming the vessels beyond a breaking point, but rather due to instabilities growing and propagating.

⁵Elegantly described as “sausage-strings”.

4.5 Perspectives: post-lumen formation

As a last illustration of P-R instability in cells, axons in neurons may display pearl-like shapes following diseases or trauma due to disruptions in the cytoskeleton or to stretching altering the tension [203], consistently with the findings of [201]. Osmotic perturbations were shown to be capable of inducing pearling, reversibly when the shock was “gentle” enough, and a model accounting for the regulation of both volume and membrane tension displayed good agreement for the experimental data [203].

The above examples thus paint a picture of the Plateau-Rayleigh instability being a feature of some important pathological cases in biology, that can reveal profound changes in the physical properties of the cells.

In the case of PDAC organoids, early comments on the potential application of the P-R instability framework on pearling can be found in the work of Sangwon Lee, a Master student that I supervised [204].

4 Lumen formation in pancreatic organoids

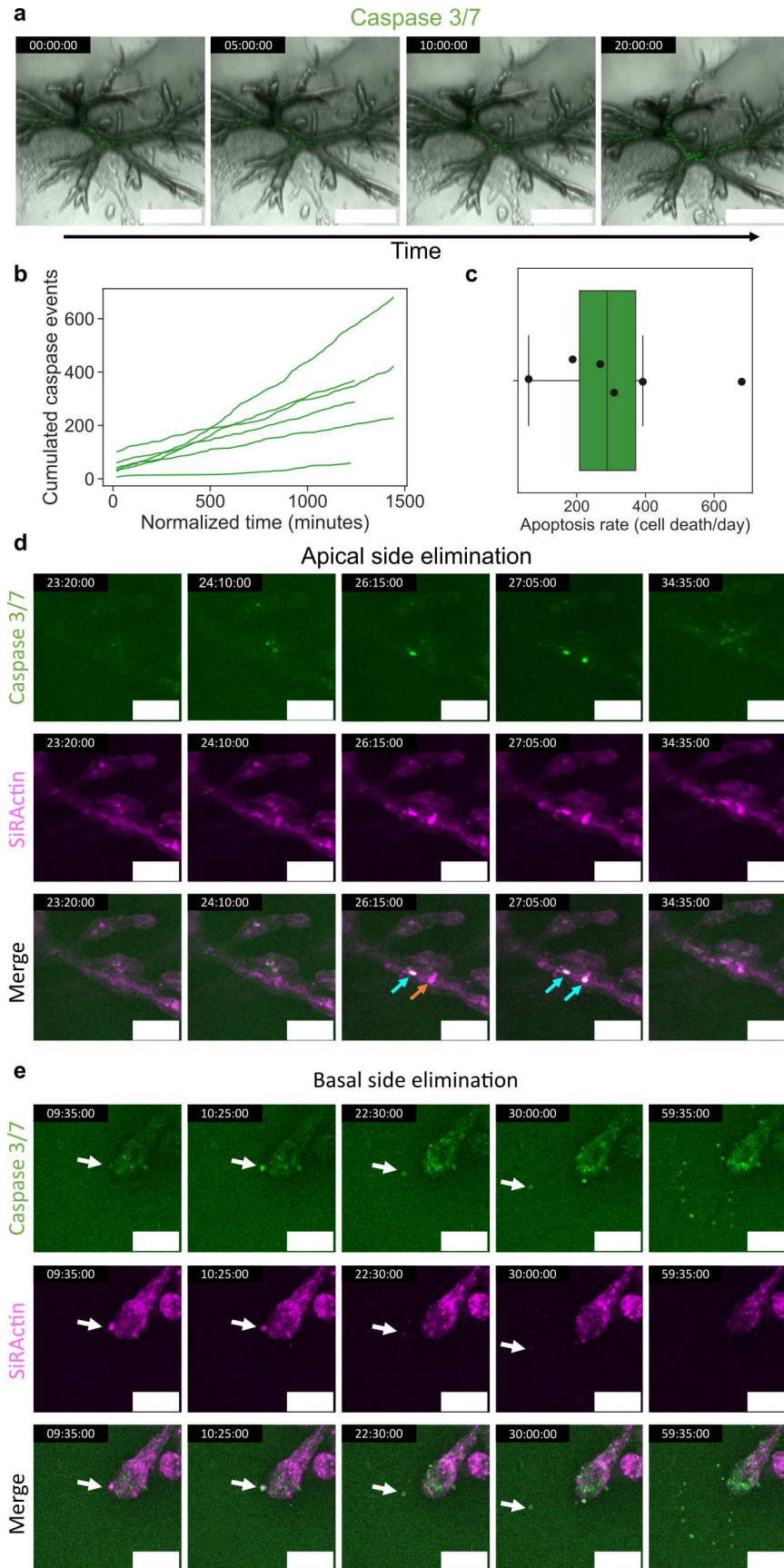


Figure 4.5: *Caption on the next page.*

Figure 4.5: **Apoptosis contributes to dark lumen formation *via* cavitation, and to cell elimination in the apical and basal directions.** **a** Summed slice projection time-lapse of an organoid labelled with NucView Caspase-3 Enzyme Substrate showing apoptotic events (in green) leading to the formation of dark lumens in the core and in the branches. **b** Cumulated caspase events detected in whole organoids during dark lumen formation (N = 6 organoids), and corresponding apoptosis rate **c**. **d** Time-lapse of a cell elimination event, from the epithelium to the apical side, post-lumen formation, visible through Caspase 3/7 activity (green) and strong increase in the actin signal (magenta, labelled with SiR-actin). Orange arrows indicate cells being eliminated displaying an increased actin signal but no caspase signal yet, while cyan arrows indicate the presence of both an increased actin signal and of caspase activity. **e** Time-lapse of a cell elimination event, from the epithelium to the basal side, post-lumen formation, visible through Caspase 3/7 activity (green) and strong increase in the actin signal (magenta, labelled with SiR-actin). The white arrow tracks the same cell over time. Scale bars: **a**: 500 μm , **d**, **e**: 100 μm . Fluorescent images in **a**, **d**, **e** are confocal summed projections. Submitted for publication in *Coexisting mechanisms of luminogenesis in pancreatic cancer-derived organoids*.

4 Lumen formation in pancreatic organoids

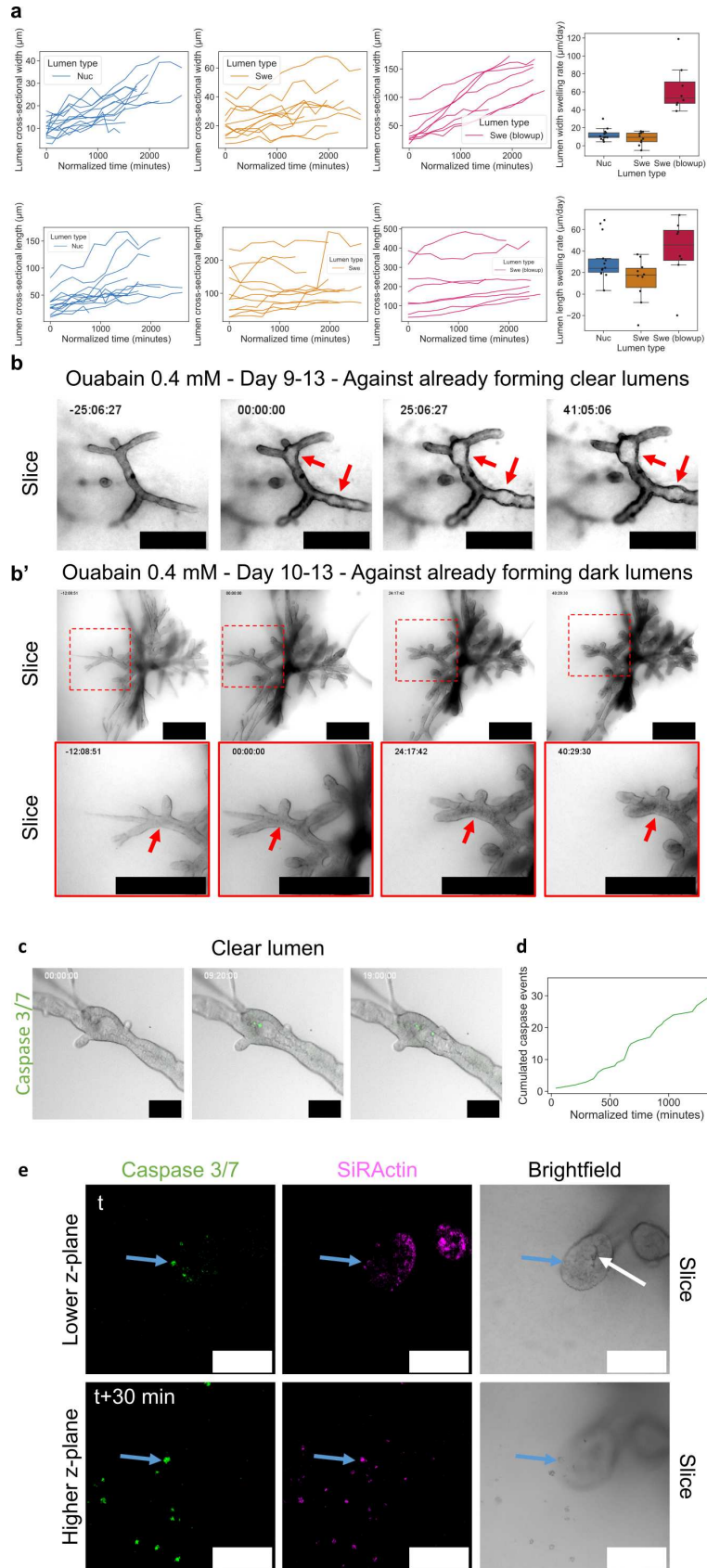


Figure 4.6: *Caption on the next page.*

Figure 4.6: **Supporting measurements for clear and dark lumens.** **a** For the clear lumens tracked in Fig. 4.3, evolution of the cavities width (minor axis of the fitted polygon, top), and length (major axis of the fitted polygon, bottom), and corresponding box plots of the estimated rates of change (“Nuc”: $n = 14$ lumens, $N = 5$ organoids; “Swe”: $n = 11$ lumens, $N = 4$ organoids; “Swe (blowup)”: $n = 8$ lumens, $N = 3$ organoids). Treatment during the Thickening to Lumen formation phase with 0.4 mM ouabain may fail to prevent lumen formation and development for two phenotypes: in **b**, organoids that had already nucleated clear lumens appear to be able to continue increasing their size; in **b'**, organoids that had already initiated the formation of dark lumens can continue their apoptosis process (bottom row shows a close up view of a dark lumen continuing its formation even after ouabain addition). Drug addition was considered as timepoint 00:00:00, and negative time values denote periods prior to drug addition. **c** Time-lapse of a clear lumen in an organoid labelled with NucView Caspase-3 Enzyme Substrate, showing very few apoptotic events occurring. Confocal slices. The corresponding cumulated counting of apoptotic events is shown in **d**. **e** Example of basal-side elimination shown in Fig. 4.5e, with apoptotic events, F-actin and bright field channels being shown. The blue arrow tracks a cell being expelled on the basal side, while the white arrow indicates an apical lumen. This implies that the presence of an apical lumen does not systematically force all elimination events to occur towards the apical side. Scale bars: **b**, **b'** 500 μm , **c**, **e** 100 μm Fluorescent images in **d**, **g**: confocal slices. Bright field images in **f**, **g**: planes. Submitted for publication in *Coexisting mechanisms of luminogenesis in pancreatic cancer-derived organoids*.

4 Lumen formation in pancreatic organoids

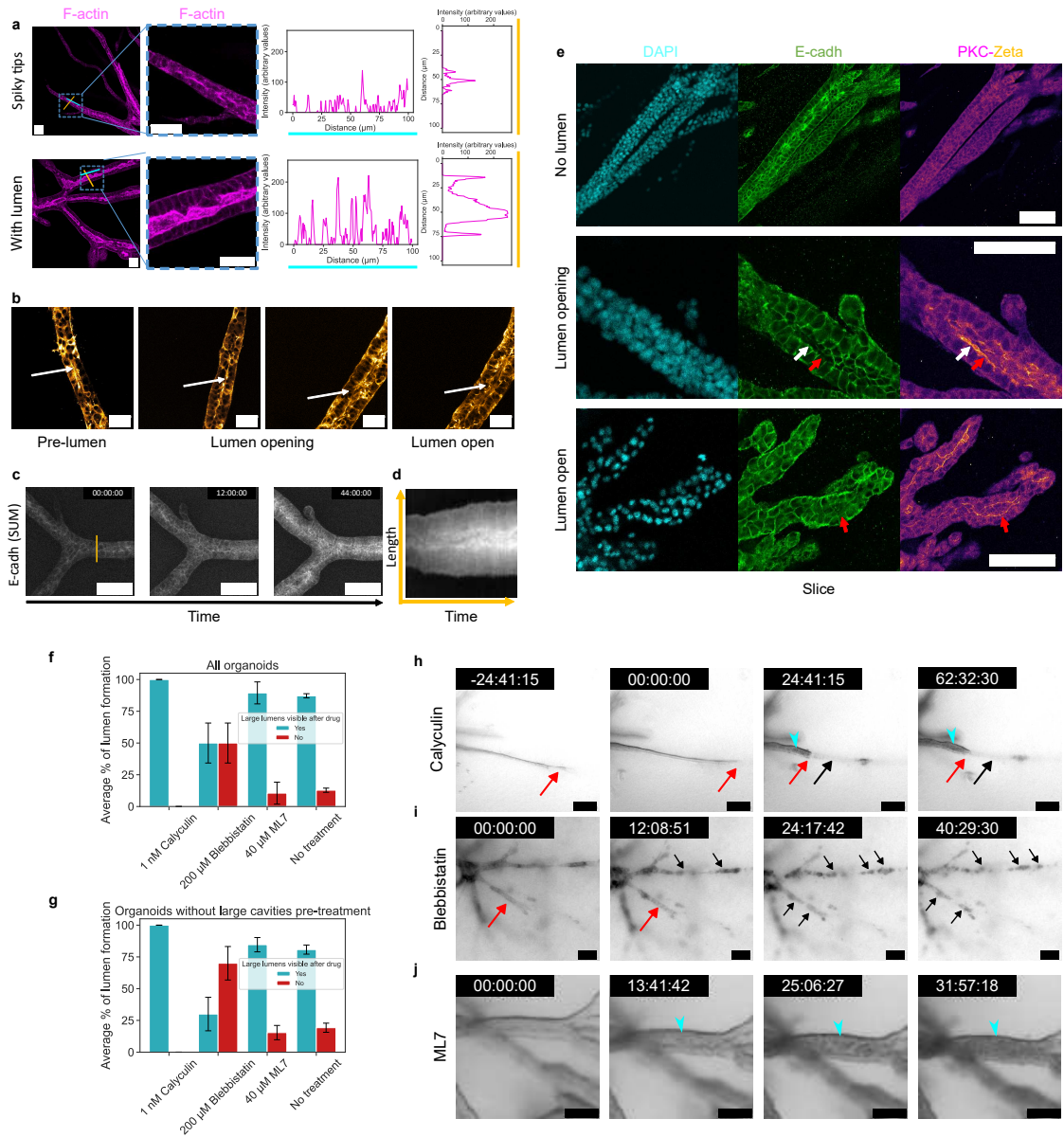


Figure 4.7: *Caption on the next page.*

Figure 4.7: **Organoids undergo progressive epithelialisation and polarisation along the central (fault) line.** **a** From left to right: F-actin organisation in a Phalloidin Alexa 633-stained organoid, closeup, longitudinal actin intensity profile along the cyan line, transversal actin intensity profile along the orange line. Top: organoid pre-Thickening. Bottom: organoid post-Thickening. **b** From left to right: Distribution fluorescent signal in organoids, overexpressing GFP-tagged non-muscle myosin IIa, pre-, during, and post-lumen opening. White arrow indicates the central line of the branch along which the lumen nucleate. **c** Time-lapse of E-cadherin distribution in an endogenously-labelled organoid during the Thickening phase, showing a global increase. The corresponding kymograph taken along the orange line is shown in **d**. **e** Top to bottom: Evolution of the E-cadherin and PKC- ζ distribution pre-, during-, and post-lumen opening. The white arrow indicates a cell where the apical side still expresses both E-cadherin and PKC- ζ , while the red arrow indicates a cell where the apical side is polarised with PKC- ζ but has lost its E-cadherin signal. Microscopy images shown are all confocal slices except for **c** which shows summed projections. **f** Average percentage of lumen formation in organoids treated at the Thickening-to-Lumen formation phase with calyculin, nitroblebbistatin, ML7, or untreated (resp. N= 8, 14, 19, 39 organoids) at various concentrations. Both organoids with and without large cavities prior to drug addition are quantified in **f**. A similar analysis restricted to organoids that did not display large lumens before drug addition is shown in **g** (with resp. N= 7, 10, 13, 26 organoids). Further concentrations are explored in Fig. 4.8. Error bars indicate the standard error of the weighted mean. Drug is added at timepoint 00:00:00 in **h-j**. **h** Calyculin treatment - shown here at 1 nM - on a phenotype still in extension at drug addition time, stops the branch extension and trigger the formation of bud-like structures as the increased contractility leads to a rupture between tip cells that remain attached to collagen fibres in front of them and cells at the back (red arrow) that retract along the path previously digested in collagen (black arrow). The cyan arrowhead indicate a lumen forming post treatment. **i** Blebbistatin treatment - shown here at 150 μ M - can trigger the fragmentation of branches in thin-branched phenotypes, with individual cells rounding up. Red arrows indicate intact branches, black arrows indicate broken branches. **j** ML7 treatment - shown here at 50 μ M - can trigger a rapid filling of clear lumens, with dark cells, as indicated by the cyan arrowhead. Scale bars: **a, b** 50 μ m; **c, e, i, j** 100 μ m; **h** 200 μ m. Submitted for publication in *Coexisting mechanisms of luminogenesis in pancreatic cancer-derived organoids*.

4 Lumen formation in pancreatic organoids

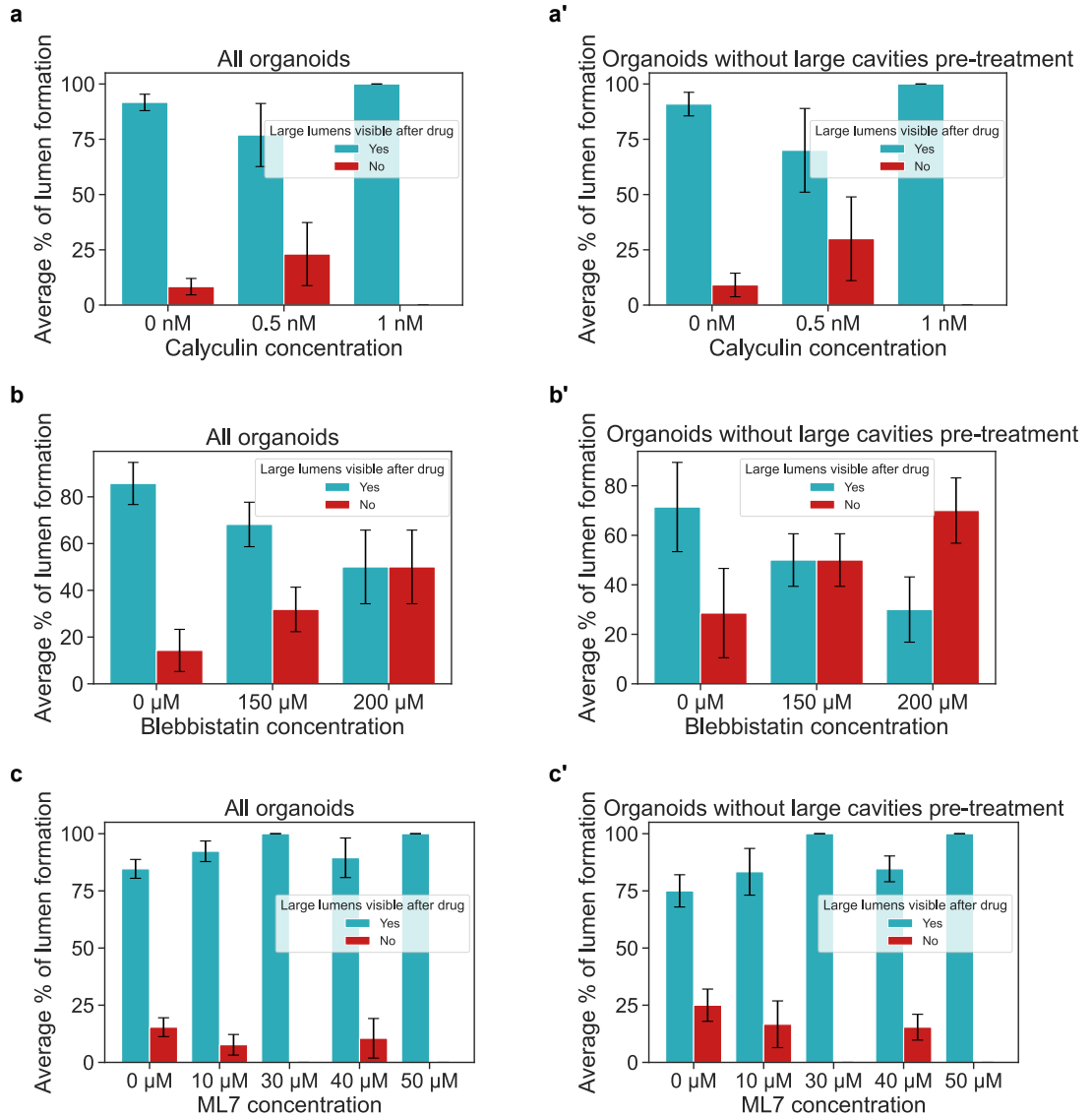


Figure 4.8: Effect of perturbations of actomyosin dynamics on lumen formation Average percentage of lumen formation in organoids treated at the Thickening-to-Lumen formation phase with nitroblebbistatin, ML7 or calyculin (resp. **a**, **b**, **c**) at various concentrations. Both organoids with and without large cavities prior to drug addition are quantified in **a**, **b** and **c**. A similar analysis restricted to organoids that did not display large lumens before drug addition is shown in **a'**, **b'** and **c'**. Sample sizes: **a** Calyculin - 0 nM : N = 12 ; 0.5 nM : N = 13 ; 1 nM : N = 8 organoids. **a'** Calyculin - 0 nM : N = 11 ; 0.5 nM : N = 10 ; 1 nM : N = 7 organoids. **b** Blebbistatin - 0 μ M : N = 14 ; 150 μ M : N = 22 ; 200 μ M : N = 14 organoids. **b'** Blebbistatin - 0 μ M : N = 7 ; 150 μ M : N = 14 ; 200 μ M : N = 10 organoids. **c** ML7 - 0 μ M : N = 13 ; 10 μ M : N = 12 ; 30 μ M : N = 20 ; 40 μ M : N = 19 ; 50 μ M : N = 12 **c'** ML7 - 0 μ M : N = 8 ; 10 μ M : N = 6 ; 30 μ M : N = 5 ; 40 μ M : N = 13 ; 50 μ M : N = 3. Submitted for publication in *Coexisting mechanisms of luminogenesis in pancreatic cancer-derived organoids*.

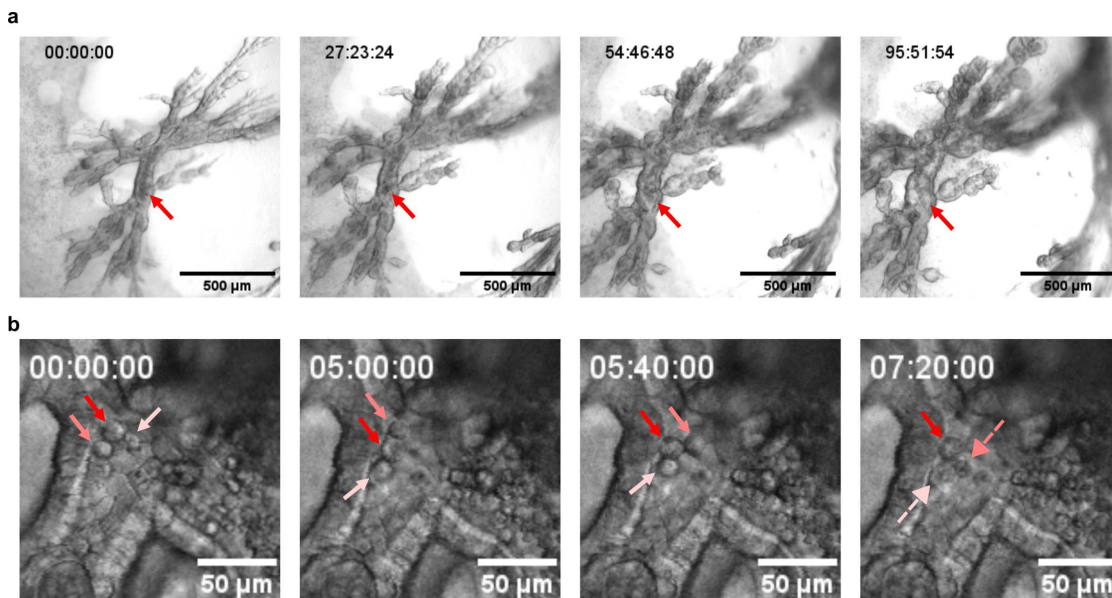


Figure 4.9: **Clearing of cells in cavities.** **a** Dark lumens filled with apoptotic cells become progressively clearer over time as fluid is further incorporated in the cavities, and as floating cells degrade. **b** Closeup view of a cavity with floating cells inside, marked by solid arrows. As fluid circulates through the cavity, cells are being displaced. In the last panel, two of the tracked cells, marked by dashed arrows undergo degradation, with their membranes losing their integrity. Scale bars: **a** 500 μm , **b** 50 μm . Submitted for publication in *Coexisting mechanisms of luminogenesis in pancreatic cancer-derived organoids*.

4 Lumen formation in pancreatic organoids

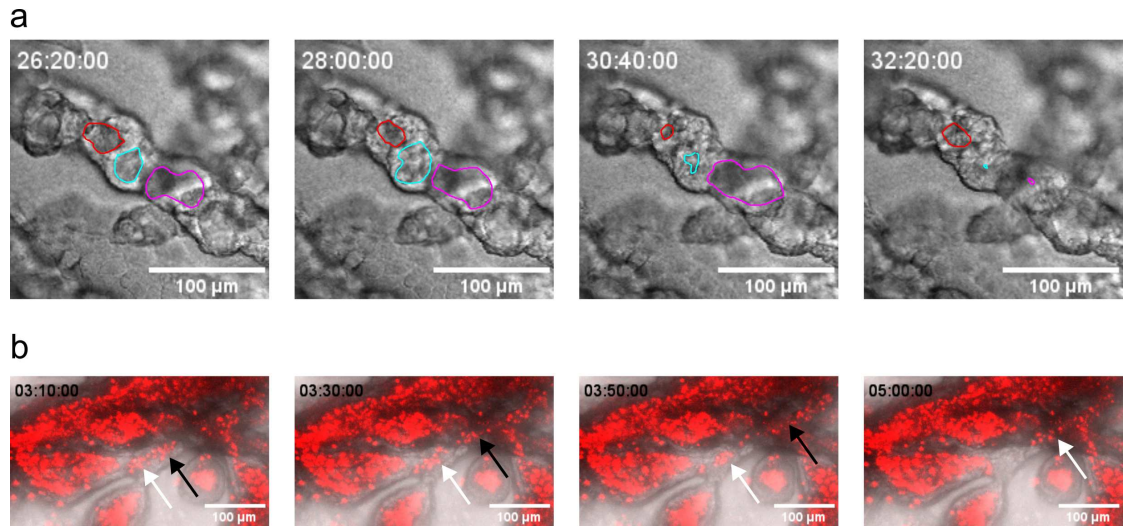


Figure 4.10: **Transport of fluid and materials in lumens.** **a** Fluid exchange between consecutive lumens, delineated in red, cyan and magenta. From panel 1 to 2, the red lumen transfers its content to the cyan one, deflating as a result. From panel 2 to 3, the cyan lumen transfers its content to the magenta lumen. In panel 4, the magenta lumen has emptied its content to the next lumen in the chain, and the red lumen is swelling again due to further fluid intake. **b** Floating cells in the lumens, with nuclei labelled with SiRDNA (red). The white and black arrows track groups of cells being progressively shuttled from a bud-like structure, towards the core of the organoid. Scale bars: 100 μm .

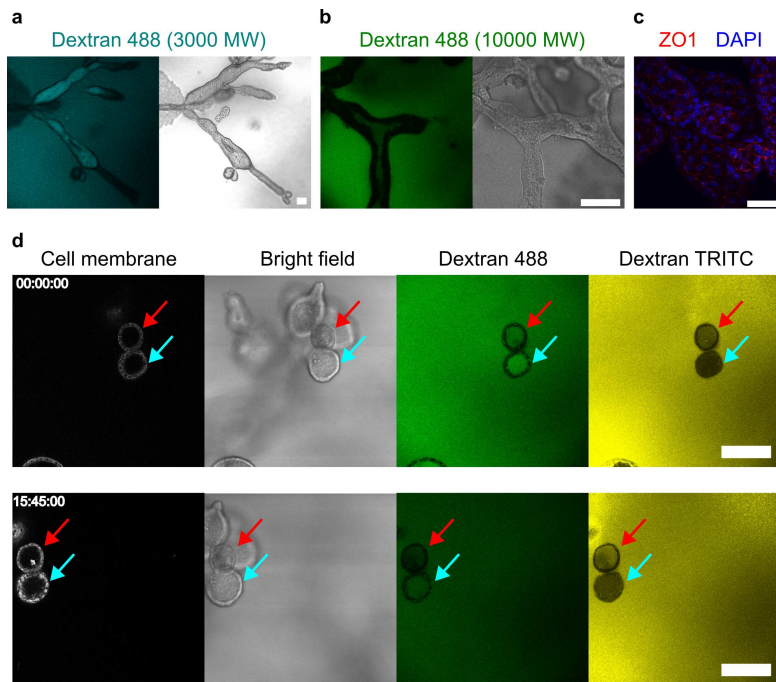


Figure 4.11: **Lumens can retain molecules** Dextran Alexa 488 3000 MW **a**, and Dextran Oregon Green 488 10000 MW **b**, added at $200 \mu\text{g.mL}^{-1}$, accumulating in lumens upon overnight incubation at Day 13-14. Confocal slices. **c** Staining of DAPI (blue) and ZO-1 (red), a protein associated with tight-junctions. Maximum projection of a confocal stack. **d** Organoids were incubated overnight with Dextran 488 3000 MW (green) in the medium at day 13. The medium was exchanged at day 14, and replaced with medium containing Dextran tetramethylrhodamine (TRITC) 3000 MW (yellow) before imaging. The cyan arrow, indicates a lumen that contains Dextran 488 but not TRITC, whereas the red arrows points to a lumen containing both dextrans (top row), indicating that organoids can locally concentrate molecules differently. 15 hours later, we observed that the lumen pointed by the cyan arrow still contained Dextran 488, and started incorporating Dextran TRITC. In the lumen marked by the red arrow, we found the intensity of the Dextran 488 signal to be decreasing, while the TRITC signal increased. Dextrans added at $200 \mu\text{g.mL}^{-1}$. Scale bars: **a**, **b**: $100 \mu\text{m}$; **c**: $50 \mu\text{m}$, **d**: $200 \mu\text{m}$. **a**, **b**, **c** reproduced and adapted from [8].

4 Lumen formation in pancreatic organoids

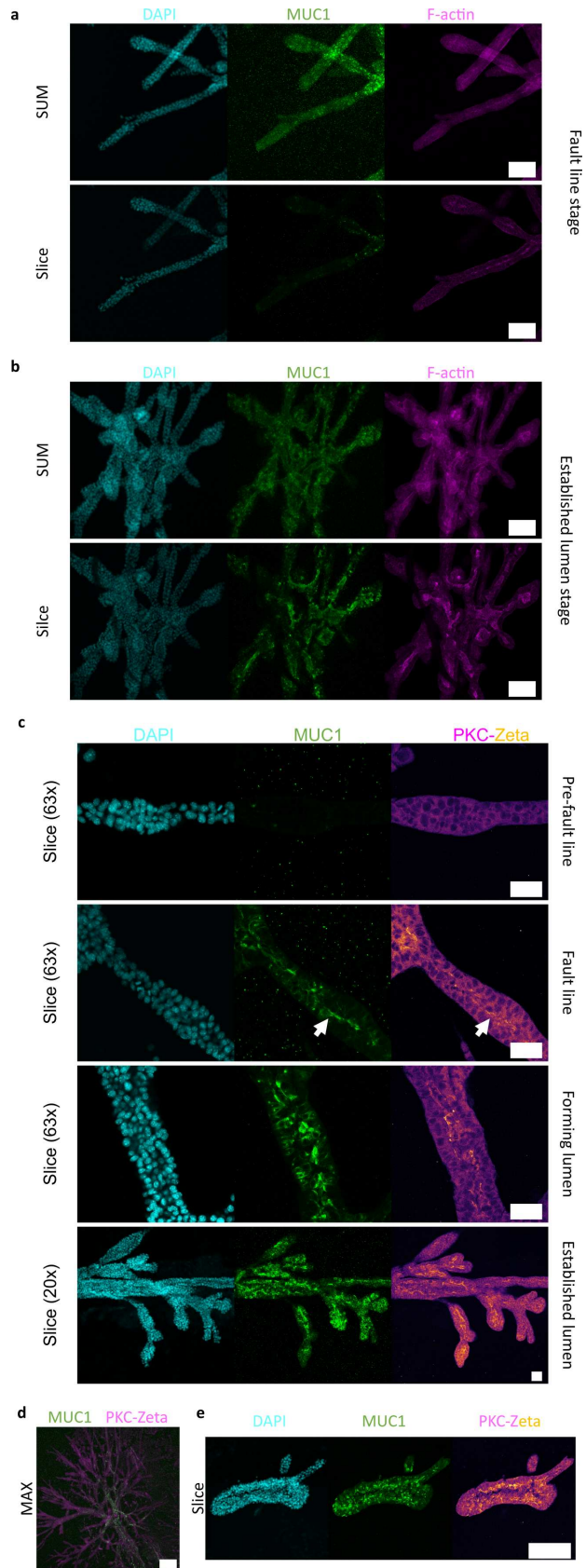


Figure 4.12: *Caption on the next page.*

Figure 4.12: **Mucin distribution.** **a** Staining of DAPI, Mucin (MUC1) and F-actin in an organoid pre-lumen formation, along a forming fault line. Top: summed slice z-projection. Bottom: z-slice. **b** Staining of DAPI, MUC1 and F-actin in an organoid with an established lumen. Top: summed slice z-projection. Bottom: z-slice. **c** Stainings of DAPI, MUC1 and PKC- ζ in organoids, from top to bottom: pre-fault line apparition, after fault line formation but pre-lumen formation, during lumen formation, and after lumen-formation, indicating the progressive apical polarisation. **d** Staining of MUC1 and PKC- ζ indicating the restriction of strong MUC1 expression to the core region of an organoid where the lumen has formed. **e** Staining of DAPI, MUC1 and PKC- ζ in a cyst-like organoid, showing strong apical polarisation and mucin expression. Scale bars: **a, b** 100 μm , **c** 50 μm ., **d, e** 200 μm . Fluorescent images are all confocal-acquired and either slices, summed projections (SUM) or maximum intensity projections (MAX). Submitted for publication in *Coexisting mechanisms of luminogenesis in pancreatic cancer-derived organoids*.

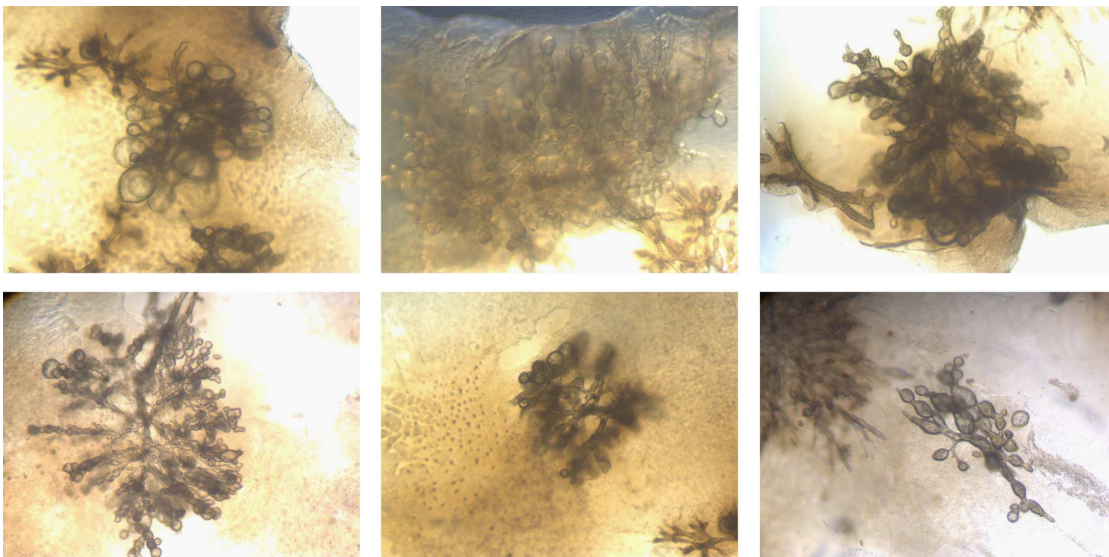


Figure 4.13: **Pearl-like structures in organoids at day 24.**

5 Materials and methods

General notes

We reproduce here part of the “Materials and methods” sections used in the articles “*Spatiotemporal dynamics of self-organized branching in pancreas-derived organoids*” [8] and “*Coexisting mechanisms of luminogenesis in pancreatic cancer-derived organoids*” (submitted at the time of writing).

5.1 Ethics declaration

For the endogenous mouse model [89] and the orthotopic transplantation model, mice were euthanized in compliance with European guidelines for the care and use of laboratory animals. In detail, animals were euthanized when a palpable abdominal mass above 1.5 cm, ascites, signs of sickness, or a weight loss of > 15% of body weight were detected. Mice were monitored on a daily basis regarding general health status as well as body weight, and housed under specific-pathogen-free conditions. Animal studies were approved by the Institutional Animal Care and Use Committees of Technische Universität München (Regierung von Oberbayern, Munich, Germany).

5.2 Mouse background

For the endogenous mouse model [89], mice were maintained on *C57Bl/6;129S6/SvEv* mixed background, and female and male mice were randomly submitted to respective tumor cohorts. For the generation of double-mutants, pancreas-specific Cre lines were intercrossed with *Kras^{G12D}-Panc* (PK mice). For the orthotopic transplantation, female athymic nude mice, aged between 7 and 9 weeks, with NU(NCr)-*Foxn1^{nu}* background (Charles River) were used.

5.3 Cells and organoids manipulations

5.3.1 Two-dimensional (2D) cell culture of PDAC cells

Primary tumour cells were collected from genetically engineered mouse models of pancreatic cancer: *Ptf1a^{Cre/+}; Kras^{G12D/+}* (KC mice)[89] or *Pdx1^{Cre/+}; Kras^{G12D/+}; TP53 Δ HO* (KPC mice). For 2D cultures, cells were seeded in 75 cm² flasks with a cell culture medium[89] composed of Dulbecco’s Modified Eagle’s Medium (DMEM)—high glucose (Sigma D6429) supplemented with 10% v/v Fetal Bovine Serum (FBS, Sigma F7524)

5 Materials and methods

and optional 1x Penicillin/Streptomycin (all from Thermo Fisher Scientific). The medium was fully exchanged every two to three days. At confluence, cells were passaged using 0.05% Trypsin-EDTA (Sigma T3924). Cells were cultured in incubators at 37 °C, under a humidified atmosphere supplemented with 5% CO₂.

Identically to PDAC cells, Phoenix ECO cells, a gift of Carsten Grashoff, were cultured with DMEM - high glucose (Sigma D6429) supplemented with 10% v/v FBS and 1% Penicillin-Streptomycin (Sigma P4333) in an incubator with a 80% humidity and 5% CO₂ atmosphere, at 37°C.

For the stable expression of fluorescent markers, retroviral transduction as well as CRISPR/Cas9 transfection was performed with same primary tumour cells. Retroviral transfection of PDAC cells was implemented during a 8 day protocol using a generated retroviral plasmid for GFP-tagged non-muscle myosin IIA. At day 1, Phoenix ECO cells were seeded in a 175 cm² flasks. Having reached a confluency of 50 to 60% (day 2), Phoenix ECO cells were transfected using Mirus TransIT-X2® Dynamic Delivery System (VWR MIRUMIR-6000) as described in the manufacturer protocol. Media exchange was performed after 24 hours (day 3) of incubation. Simultaneously, PDAC cells were seeded in a 75 cm² flask. Virus was harvested after 48 hours (day 4) from Phoenix ECO cells and sterile filtered (0.45 µm pore size). Supplemented with 7.5 µg/ml polybrene (Sigma TR-1003-G) the virus conditioned media was added to the PDAC cells and incubated for 24 hours. This was repeated at day 5. After 48 hours of incubation with virus conditioned media, media was exchanged for PDAC cells with fresh DMEM - high glucose (Sigma D6429) supplemented with 10% v/v FBS (Sigma F7524) and 1% Penicillin-Streptomycin (Sigma P4333). After 72 hours cells were passaged as previously described. Selection of fluorescently labeled cells was implemented by antibiotic resistance, using Geneticin Selective Antibiotics (Thermo Fisher 10131035) and FACS sort with BD Aria Fusion. A CRISPR/Cas9 system was used to endogeneously label E-cadherin in the used primary tumour cells.

5.3.2 Organoid preparation

Collagen-grown organoids were prepared by adapting a previously-described protocol [94]. Cells cultured in 2D were first detached using trypsin, and a series of dilution was performed to reach a concentration of 500 cells/mL in medium.

Gels were prepared by mixing gently together the cell suspension, cell culture medium, neutralizing solution (550 mM HEPES in 11x PBS), and collagen type I (rat tail, 354236 Corning), for a collagen concentration of 1.3 mg/mL. Gels were incubated for 1h to 1h30 at 37 °C to polymerise, and were then gently detached from the sides and bottom of the culture dish using a pipette tip, before being covered by additional cell culture medium.

For Matrigel-grown organoids, cells were mixed with growth factor-reduced Matrigel (Corning), seeded as domes or rectangular gels and were allowed to polymerise for 1h at 37 °C.

For both types of organoids, medium was exchanged every two days.

Organoids were cultured in ibidi µ-Slide 2-wells (80286), ibidi µ-Plate 24 Well (82426) or Sarstedt 24-well (83.3922).

5.3.3 Cloning and retroviral transfection

The GFP-tagged non-muscle myosin IIA plasmid for transfection was generated using restriction enzymes and PCR reaction to amplify the fragments for Gibson Assembly. The backbone was digested using BamHI and Sall in combination with the plasmid pTK93_Lifeact-mCherry, which was a gift from Iain Cheeseman (Addgene plasmid # 46357) [205]. The CMV promoter was extracted from mRuby-LC-Myosin-N-7, a gift from Michael Davidson (Addgene plasmid # 55871), the myosinIIA-GFP from Myosin-IIA-GFP was a gift from Matthew Krummel (Addgene plasmid # 38297) [206], the IRES sequence from pQCXIP-mCherry-Halo-YAP1 was a gift from Yutaka Hata (Addgene plasmid # 128336) [207], and the Neomycin resistance from mRuby-LC-Myosin-N-7 was a gift from Michael Davidson (Addgene plasmid # 55871).

The following PCR primers were used:

CMV promoter:

Forward 5'-GGAGTTCCGCGTTACATAACTTACG-3'

Reverse 5'-GTTCACTAAACCAGCTCTGCTTATAT-3'

Myosin-IIA-GFP:

Forward 5'-CTACCGGTCGCCACCATGG-3'

Reverse 5'-CTGATTATGATCAGTTATCTAGAAGCG-3'

IRES:

Forward 5'-CCGTCTTTTGGCAATGTGAGGG-3'

Reverse 5'-TTATCATCGTGTTTTTCAAAGGAAA-3'

Neomycin:

Forward 5'-ATGATTGAACAAGATGGATTGCACGC-3'

Reverse 5'-CCCCAGAGTCCCGCTCAGAAG-3'

5.3.4 Chemical perturbations

Unless explicitly mentioned otherwise, all the drug concentrations listed in this thesis are given considering exclusively the volume of medium added to the culture well, and excluding the volume of the gel.

We made this choice to standardise the volume of chemicals added. Hydrogels can trap liquid, thereby affecting their volume. Depending on the quality of the pipetting during a medium exchange, the quantity of liquid remaining in the soaked gel can vary, which renders the estimation of gel volume impractical.

To perturb mitosis, aphidicolin (Sigma A4487) was used at 2 $\mu\text{g.mL}^{-1}$ (concentration in medium) for live imaging. To inhibit matrix metallo proteinases (MMP) activity, batimastat (Sigma SML0041) at 10 μM was used. To induce organoid swelling by Cl^-/Na^+ influx, we used Forskolin (Sigma F6886) at 10 μM . To act on the Rho-GTPase pathways and inhibit MYOII, the Y-27632 Rock inhibitor (Biomol 10005583) was used at 5 μM . For live imaging, unless mentioned otherwise, drugs were added immediately prior setting up samples for imaging.

In the perturbations experiments performed in Chap. 3 using batimastat, calyculin and nitro-blebbistatin, organoids were cultured in μ -Plate 24-wells (ibidi 82426). Or-

5 Materials and methods

ganoids were live-imaged for approximately 24 hours prior to drug addition, to control for the presence of the hallmarks of the desired developmental phase to perturb, before introducing the drug to the culture well and resuming the live imaging.

For the ouabain, calyculin A, nitroblebbistatin, and ML7 experiments performed in Chap. 4, the presence of lumens in organoids after treatment was determined by visually assessing the planes of bright field z-stacks recordings over time. We recorded whether organoids were displaying cavities prior to drug addition, after drug addition, as well as the type of lumens predominantly formed (clear or dark).

In Fig. 4.3, Fig. 4.7, Fig. 4.6, Fig. 4.8, we excluded from our analysis the organoids that were fragmented or did not exhibit hallmarks of the Thickening to Lumen formation phase with thick and budding branches (e.g. organoids with very thin branches remaining in an Extension phase-like phenotype). Organoids that, reached a phenotype that could allow lumen formation following drug addition, were included in the analysis. Based on our criteria, organoids were observed for two to three days following drug addition to quantify the lumen formation capability. The “No treatment” data shown in Fig. 4.7f-g pools together the untreated organoids shown in Fig. 4.8a-c’.

5.3.5 Immunofluorescent staining

Organoids were washed and fixed using 4% paraformaldehyde (Sigma 158127) for 15 minutes at room temperature (RT). Cells were permeabilised using 0.2% Triton X-100 (Sigma T87787) in PBS (Roth 0890.1) for 10 minutes at RT and blocked overnight at 4 °C using 10% goat (Sigma G6767) or donkey serum (Sigma D9663)/0.1% Bovine Serum Albumin (BSA) (Roth 8076.2). Cells were then labelled with primary antibodies diluted in 0.1% BSA and incubated overnight at 4 °C. Afterwards, secondary antibodies diluted in 0.1% BSA were added and incubated at least two hours at RT in the dark.

Antibodies and fluorescent markers used are shown in Tables 5.1, 5.2, 5.3.

Name	Target	Conjugation	Catalogue	Supplier	Dilution
Phalloidin	F-actin	Alexa 488	A12379	Invitrogen	1:250
Phalloidin	F-actin	Alexa 633	A22284	Invitrogen	1:250
SiR-actin	F-actin	Silicon Rhodamine	SC001	Spirochrome	100 nM
NucView 488 Caspase-3 Substrate	Caspase-3/7 activity	NucView 488 dye	10402	Biotium	5 μ M
NucView 530 Caspase-3 Substrate	Caspase-3/7 activity	NucView 530 dye	10406	Biotium	5 μ M

Table 5.3: **Additional fluorescent probes.**

Epitope [Clone]	Conjugation	Host	Catalogue #	Supplier	Dilution
E-cadherin [24E10]	-	Rabbit	3195S	Cell Signaling	1:50
PKC-Zeta	Alexa 647	Mouse	sc17781	Santa Cruz Biotechno- logy	1:50
Phosphorylated Myosin Light Chain 2 [E2J8F]	-	Rabbit	95777S	Cell Signaling	1:200
Mucin 1	-	Rabbit	ab15481	Abcam	1:150
N-cadherin [13A9]	-	Mouse	14215	Cell Signaling	1:100
Krt 19	-	Rat	Troma III	DSHB	1:100
Ki67	-	Rabbit	ab15580	Abcam	1:300
α 6 Integrin [GOH3]	-	Rat	sc19622	Santa Cruz Biotechno- logy	1:150
Laminin	-	Rabbit	L9393	Sigma	1:100
ZO1 [ZO1-1A12]	-	Mouse	339194	Invitrogen	1:100
α SMA [1A4(asm- 1)]	-	Mouse	MA5-11547	Thermo Fisher Scientific	1:100
Caspase 3	-	Rabbit	9662	Cell Signaling	1:100
Cytokeratin 7 [EPR17078]	-	Rabbit	ab181598	Abcam	1:100

Table 5.1: **Primary antibodies.**

5.4 Imaging

5.4.1 Microscopes

Confocal imaging was performed on a Leica DMI8 confocal microscope (software LAS X version 3.5.7.23225) or Leica TCS SP5 II confocal microscope (software LAS AF version 2.6.3.8173), and bright field imaging was performed on a Leica Thunder DMI8 Thunder microscope (software LAS X version 3.7.5.24914). For live sample imaging, samples were kept at 37°C and under a 5% atmosphere using an ibidi Stage Top Incubation System (ibidi 10722). A list of objectives is shown in Table 5.4.

5 Materials and methods

Host/Isotype	Species reactivity	Conjugation	Catalogue #	Supplier	Dilution
Goat	Rabbit	Alexa 488	A11034	Invitrogen	1:250
Goat	Rat	Alexa 594	A11007	Thermo Fisher Scientific	1:250
Donkey	Rabbit	Alexa 546	A10040	Thermo Fisher Scientific	1:250
Goat	Mouse	Alexa 546	A11030	Thermo Fisher Scientific	1:250

Table 5.2: **Secondary antibodies.**

Objective name	Magnification	Numerical Aperture	Immersion	Microscope
HC PL FLUOTAR	10x	0.30	DRY	Leica SP8
HC PL FLUOTAR	10x	0.45	DRY	Leica SP8
HC PL APO CS2	20x	0.75	DRY	Leica SP8
HC PL APO CS2	40x	1.10	WATER	Leica SP8
HC PL APO CS2	63x	1.30	GLYC	Leica SP8
N PLAN	5x	0.12	DRY	Leica Thunder
HC PL FLUOTAR	10x	0.32	DRY	Leica Thunder
HC PL FLUOTAR L	10x	0.40	DRY	Leica Thunder
HC PL APO	40x	1.30	OIL	Leica Thunder

Table 5.4: **Objective list.**

5.5 Live imaging

5.5.1 General live imaging parameters

Live-cell imaging Live imaging was performed using a Leica TCS SP5 II confocal microscope (software LAS AF version 2.6.3.8173) and a Leica DMI8 confocal microscope (software LAS X version 3.5.5.19976). Live-imaged samples were kept at 37 °C in a 5% CO₂ atmosphere using an ibidi Stage Top Incubation System (ibidi 10722). For live imaging, cell nuclei were labelled using SiRDNA (Spirochrome SPY650-DNA SC501) for a minimum of 3 h before measurement at 1-2 $\mu\text{g}\cdot\text{mL}^{-1}$ (concentration in collagen + medium volume). To avoid potential interference due to phenol red when imaging with SiRDNA, we used Dulbecco’s Modified Eagle’s Medium—high glucose no phenol red (Thermofisher 21063-029) + 1:10 Fetal Bovine Serum (Sigma F0804), hereafter described as the “observation medium”. Plasma membranes were labelled using CellMask Deep Red (Thermofisher C10046) at 0.1%.

5.6 Image analysis tools

Images were analysed using ImageJ (ver. 1.54f)[208], ilastik (ver. 1.3.3) [209] and Arivis Vision4D (ver. 4.0.0).

3D image reconstruction was conducted with Imaris (8.2.0, Oxford Instruments).

Images were drift corrected using the TurboReg, StackReg [210] and HyperStackReg [211] plugins for ImageJ.

5.7 Data analysis

Investigators were not routinely blinded during analysis.

Python (ver. 3.7.10) with the *seaborn* (ver. 0.11.1), *SciPy* (ver. 1.6.2) package were used to analyse numerical data and produce graphs. 95% confidence intervals were computed via 1000 bootstrap iterations through the *seaborn* package. The python *stats* `linregress` function was used to perform linear regression fits.

Graphpad Prism (ver. 9.0.2) and R (ver. 4.0.4) were used for additional statistical analysis. Wolfram Mathematica 10 was used for analyses and simulations of the minimal biophysical model.

5.7.1 Estimation of organoid size

In Chap. 2, the sizes of control collagen-grown and Matrigel-grown organoid were determined using ilastik Object Classification routine to segment bright field images and extract the major-axis of automatically fitted ellipses. In the case of fragmented phenotypes induced by treatment with batimastat, the major axis was measured by manually fitting an ellipse using ImageJ.

In Chap. 3 bright field time-lapse images acquired on a Leica Thunder microscope at 5x 0.12 NA organoids images were projected as minimum z-projections using ImageJ and then processed using a manually-trained deep learning segmentation routine on Arivis Vision4D.

5.7.2 Bead branch tracking

To monitor the deformation field generated by organoids in the ECM, fluorescent beads (Fluoresbrite YG Microspheres 3.00 μm , Poly- sciences 17155-2) were added at cell seeding time in the non-polymerized collagen mixtures. Branch tips and fluorescent beads located in a cone in front of active tips were manually tracked using ImageJ “Manual tracking” plugin on confocal live imaging full stacks or with maximum projections when the organoid growth remains in focus.

5.7.3 Ki67 to DAPI ratio estimate

Immunostaining pictures of organoids stained against DAPI and Ki67 at 10x magnification were used to estimate the ratio of Ki67-positive to DAPI-positive cells over time.

5 Materials and methods

Coloured jpg images for each channel were converted to grayscale using ImageJ. The Cell Density Counting routine of ilastik was then used to analyse each channel dataset separately. A subset of cells was labelled before running the algorithm and manual corrections were performed as needed to refine the detection. As the ilastik Cell Density Counting routine tends to overestimate the cell numbers at early time points for DAPI and Ki67, and at late time points for Ki67, we also performed a fully manual counting to correct the data points showing aberrant orders of magnitude, using ImageJ Cell Counter. Ratios are computed for each organoid by dividing the number of counted Ki67-positive cells by the number of detected cells in the DAPI channel. To assess the effect of batimastat and Y-27632 on the proliferative capabilities of organoids, organoids were treated continually, starting at seeding time with either of the drug, fixed at day 7 or 13, stained against DAPI and Ki67, and compared to non-treated organoids also stained against DAPI and Ki67 at the same timepoints. To estimate the number of DAPI- and Ki67-positive cells, we used the Cell Density Counting routine of ilastik. The channels were processed separately. In addition, the day 7 and day 13 images were processed separately. Manual and semi-automatic measurements are shown in Fig. 5.1.

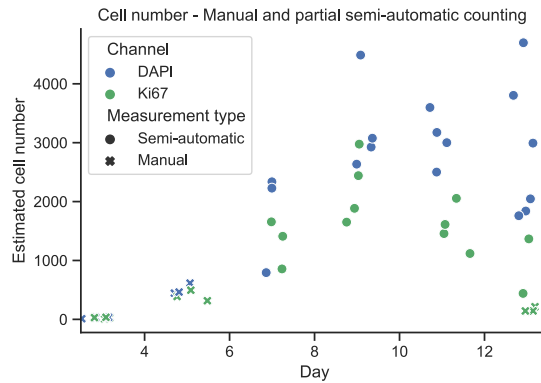


Figure 5.1: DAPI (blue) and Ki67-positive (green) cell numbers estimated from maximum projections using manual or semi-automated counting, at day 3, 5, 7, 9, 11, and 13 ($n = 24$ organoids). Reproduced and adapted from [8].

5.7.4 Cell nuclei number determination

Cell numbers were estimated using maximum projection images of DAPI-stained organoids. For the semi-automatic counting, projections were loaded in ilastik and processed using the Cell Density counting routine: a subset of the nuclei data was manually labelled before running the density estimation algorithm. Iterations of manual corrections were performed as needed to refine the detection. We also performed a fully manual counting of a subset of the same maximum projections, up to day 9, using the Cell Counter plugin of ImageJ to ascertain the order of magnitude given by the ilastik algorithm.

5.7.5 Branch thickness measurement (live)

For the dynamic branch thickness measurements, we used ImageJ line drawing tool on bright field channel movies acquired with confocal microscopy. We measured the tip width by drawing a line 30 μm behind the branch tip. When the branch possesses a spiky phenotype, we ignore the leading protrusion and measure the width 30 μm behind the beginning of the protrusion. The “body” measurements are measured using the same protocol, but at a distance of 100 μm .

5.7.6 Branch thickness measurement (static)

For static branch thickness measurement, we used ImageJ line drawing tool on summed projections images of organoids stained with CellMask (Thermofisher C10046) at 0.05%, acquired with confocal microscopy. We measured the terminal branch width by drawing a line 30 μm behind the branch tip. When the branch possessed a spiky invasive protrusion at the tip, we ignored the leading protrusion and measured the width 30 μm behind the beginning of the protrusion. During the Onset phase, to account for nascent terminal branches that are <30 μm long, we measure the width at the base of the terminal branch, close to the branching point. The “body” measurements are measured using the same protocol, but at a distance of 100 μm of the terminal branch tip. We also measure the width of non-terminal branches “after a branching point”, at a distance of 100 μm after the base of the “Y” shape defined by two branches meeting each other.

5.7.7 Branch length measurement (live)

For the dynamic branch length measurements, we used ImageJ line drawing tool on the bright field channel acquired with confocal microscopy. We measure the branch length by drawing a segmented line starting from the tip of a branch, including the leading spiky protrusion if there is one, and going up to the nearest branching point. When plotting all branch lengths on the same graph, we normalized the time by setting zero as the first frame in which a branch is tracked.

5.7.8 Branch counting (static)

Organoids at different timepoints were fixed and stained with Cell- Mask at 0.05% to label their plasma membranes. Confocal microscopy was used to acquire z-stacks, which were then reconstructed in three dimensions and analysed on Imaris. A “branch” was defined as the segment between a “tip” and a branching point (in this case a so-called “terminal branch”), or between two branching points (in this case a so-called “non-terminal branch”), and manually labelled.

5.7.9 Branching event counting

Branching events were manually counted on live imaging confocal stacks using ImageJ. We consider the leading 6 cells of a branch. True- Yes: indicates that a branching

event was preceded by a proliferation event. True-No: indicates that a branching event occurred without being preceded by a proliferation event. False-Yes: indicates that a proliferation event occurred but was not followed by a branching event.

5.7.10 Collagen reflection microscopy

Collagen fibres were imaged using the Reflection mode of a SP5 II confocal microscope and of a Leica DMI8 confocal microscope, with the 488 nm laser line. To visualize the collagen architecture surrounding the organoids while avoiding auto-fluorescence artefacts from the cell membranes when using reflection microscopy, we incubated live organoids with Triton-X 100 diluted at 10% in PBS for a minimum of 1 h in order to degrade the cell membrane. Organoids were then washed one time with PBS, fixed for 15 min in 4% PFA at room temperature, and washed again four times with PBS for a total of 20 min. Organoids were either stored at 4 °C in PBS or imaged immediately. We used CellMask, a plasma membrane staining dye, at 0.1%, to ensure that the cell membranes were properly degraded.

5.7.11 Intensity profiles and kymographs

Line intensity profiles were obtained using the “Plot Profile” tool of ImageJ on z-slice images, following a thresholding step.

For kymographs, z-stacks were first z-projected as Sum Slices projections and drift-corrected. A 100 μm long and 50 μm wide line was then drawn in the region of interest and kymographs were obtained using the KymoResliceWide plugin for ImageJ [212] using the “Intensity across width: Average” and “Ignore image calibration” options selected.

5.7.12 Lumen type identification

To determine the type of lumens formed in organoids, bright field optical stacks of live-imaged organoids were analysed, with multiple focal planes reviewed. To discriminate between lumens nucleating via central cell apoptosis (dark lumens) and lumens nucleating via fluid intake (clear lumens) later filled with post-lumen formation cell elimination - which can both appear as dark cavities in bright field - live imaging was started during the Thickening phase of the majority of the organoids, pre-lumen formation, to monitor the entire lumen formation process.

5.7.13 Lumen morphometrics

To quantify the evolution of clear lumen geometries over time, we looked for the middle cross-sectional plane of lumens on bright field z-stacks and manually segmented the lumens using the Polygon tool from ImageJ.

Due to inter- and intra-organoid heterogeneity, cavities could start forming at different timepoints between and within organoids. We labelled cavities that we could segment from their nucleation point onward as “Nuc” (for “nucleating”), whereas cavities that had already nucleated and grown before the start of imaging were labelled as “Swe” (for

“swelling”). In case a tracked microlumen fused with a neighbouring cavity, we recorded the event and labelled it additionally as “fus” (for “fusing”). In the case of organoids displaying a “blowing up” phenotype, we delineated virtual boundaries around swelling cavities to capture the increase in the minor axis, even in the case of fusing or connected cavities. This results in an under-estimation of the real area of blowing up lumens.

Swelling rates were approximated through linear regression, excluding tracks that contained fusion events between microlumens.

5.7.14 Apoptotic event counting

Apoptotic cells in organoids were labelled using a fluorescent caspase-3/7 activity reporter (#10402 and #10406 Biotium) and we performed live imaging during the period spanning the Thickening and the Lumen formation phases. Apoptotic events were detected using Arivis Vision4d *Blob Finder* routine on the fluorescent signal. Rates of apoptosis were estimated by fitting a linear function to the cumulated apoptosis events detected curves. The apoptosis event counting was limited to 24 hours to avoid as much as possible counting the cell death events occurring post-lumen formation.

5.7.15 Figure preparation

Images were assembled using Inkscape v1.3.

Appendix

1 Permissions, data availability, and authors contributions

1.1 Permissions

Permission to re-use the content authored and published in *Nature Communications*[8] is granted according to the “Authors reuse” terms of the journal¹. Figures marked as “Submitted for publication in *Coexisting mechanisms of luminogenesis in pancreatic cancer-derived organoids*” have been submitted, at the time of writing, to a journal allowing the re-use of previously published images, provided the original publication is cited. Upon publication of the manuscript, this thesis will be amended with the proper reference.

Re-use of figure 0.2 is covered under the Creative Commons Attribution 3.0 Unported licence². Adaptation of Figure 3.9, adapted from [116], is covered under PLOS One Creative Commons Attribution 4.0 International (CC BY) licence³.

1.2 Availability of data, materials, and code

Source data used to generate the published graphs in this manuscripts are available on Zenodo repositories with the DOI 10.5281/zenodo.6577226 and 10.5281/zenodo.11060358. Additional data, such as confocal or bright field stacks, that support the findings of this thesis are available upon request.

1.3 Contribution of authors to collaborative figures

Figures resulting from a collaboration and/or that have led to a multi-author publication are labelled accordingly in their respective captions. This section details the role of each contributor for each of the collaborative figures.

Abbreviations: Andreas R. Bausch: ARB; Edouard Hannezo: EH; Hans Carlo Maurer: HCM; Rupert Öllinger: RÖ; Aristeidis Papargyriou: AP; Roland Rad: RR; Marion K. Raich: MKR; Samuel Randriamanantsoa: SR; Maximilian Reichert: MR; Dieter Saur: DS; Katja Steiger: KS Giulia Zecchin: GZ;

Figures and panels that do not appear in the list below are, unless mentioned in their caption, the results of SR’s experiments and analysis. ARB contributed to the overall supervision of this thesis. MR contributed to the co-supervision for the project

¹<https://www.nature.com/nature-portfolio/reprints-and-permissions/permissions-requests> - Accessed 30/11/2023

²<https://creativecommons.org/licenses/by/3.0/deed.en>

³<https://creativecommons.org/licenses/by/4.0/>

Appendix

described in Chapter 2. Please note that all contributions are also mentioned in the publications ([8] and soon to be published *Coexisting mechanisms of luminogenesis in pancreatic cancer-derived organoids*) “Author contributions” sections.

- Fig. 2.2: AP performed the imaging and stainings for **a**, **b**. SR analysed the data and produced graph **c**.
- Fig. 2.3: AP cultured the organoids. KJ performed the histology.
- Fig. 2.5: AP produced the organoid samples. SR analysed the data.
- Fig. 2.7: AP performed the stainings and imaging of **c**, **d**. SR performed the stainings and imaging of **a**, **b**.
- Fig. 2.9: AP isolated the RNA. RÖ and RR performed the RNA-seq. HCM analysed the RNA-seq data.
- Fig. 2.10: AP stained and imaged the samples in **c**. SR performed the experiments, imaging and analysis of **a**, **b**, **d**, **e**.
- Fig. 2.11 Data in **a**, **a'**, **b**, **c** was acquired in collaboration between SR and GZ, and analysed in collaboration with EH.
- Fig. 2.13, 2.14, 2.15: data was acquired by SR, and analysed in collaboration with EH.
- Fig. 2.16: SR collected the data. EH developed the theoretical model. SR and EH validated together the model.
- Fig. 2.17: EH performed the simulations in **a-e**, **g**. SR performed the experiments in **f**, **h**.
- Fig. 2.18: SR performed the experiments in **a**, **d**. Data was analysed in collaboration between SR and EH.
- Fig. 2.19: AP performed the imaging in **a**, **b**, collected and analysed data in **c**. Samples for **d** were acquired by AP, analysed by SR, and plotted by AP.
- Fig. 2.20: AP isolated the RNA. RÖ and RR performed the RNA-seq. HCM analysed the RNA-seq data. For **h**, AP and SR acquired the data and analysed it.
- Fig. 2.21: AP isolated the RNA. RÖ and RR performed the RNA-seq. HCM analysed the RNA-seq data.
- Fig. 3.2: MKR designed the YFP-Caax 9591 cell line, and performed the experiment and imaging.
- Fig. 3.3: MKR designed the myosin IIA GFP-tagged 9591 cell line, and performed the experiment and imaging.

- Fig. 3.6: GZ collected the data, SR analysed it.
- Fig. 4.4: AP performed and analysed the forskolin treatment experiment in **b**, **c**.
- Fig. 4.7: MKR generated and imaged the myosin IIA-GFP-tagged 9591 cell line in **b**. The E-cadherin-mNeonGreen-tagged 9591 cell line was a gift from the lab of DS. Rest of the experiments, imaging and analysis performed by SR.

2 Experimental challenges brought by branching PDAC organoids

This section is meant to highlight a number of challenges inherent to the organoid model system, its culture protocols, its imaging, its analysis.

As published studies rarely stress the practical difficulties faced in the experimentation phase, it is important to document in this thesis the challenges encountered for the sake of potential readers attempting to continue this project or undertake similar experiments.

The issues presented hereafter are generally applicable both to the study of branching processes, and to the study of the budding and luminogenesis processes.

The reader will find in the Materials and Methods chapter (Chapter 5) a description of the protocols and tools used for the various imaging and analyses presented.

2.1 The question of heterogeneity and reproducibility in organoid culture: problems and opportunities

Organoids, either in the form of spheroids or as more elaborate structures, leverage the morphogenetic processes of the stem, embryonic, or cancer cells they derive from. Due to their *in vitro* condition however, organoids lack part of the guiding cues and constraints that are present *in vivo*, and that normally lead to the formation of well-defined structures [15]. Instead, organoid cultures are subject to a high degree of stochasticity, that may pose an issue of reproducibility [15, 213, 214]. However, given the actual heterogeneity in diseases, and the heterogeneity in the response to treatments, having organoids that capture these differences may prove crucial [21, 215].

A multitude of mechanisms *in vitro* may influence organoid development, such as the matrix type [96, 97, 216], stiffness [217], structure [218], the tissue geometry [182], or the cell heterogeneity [66, 68, 69], in addition to the inherent stochasticity of some processes such as the decisions to proliferate or branch [8, 54, 219]. Despite the considerable progress made in identifying those factors, integrating all these elements and their relative influence to determine *a priori* the type of structure that will emerge from the developmental process remains an extremely complex task.

The diversity of phenotypes emerging from the system presented in this thesis has thus considerably complicated both the qualitative and the quantitative analysis of organoid development, as relying on chance was sometimes needed to observe in real time the dynamics of phenotypes that could differ in their size, their number of branches, their cystic or not shape, their type of lumens, etc.

Developing protocols allowing for the selection of particular phenotypes thus appears crucial to simplify the testing of hypotheses in future experiments. A detailed transcriptomic analysis of the different phenotypes may further help to rationalise the link to the observed biophysical events.

Picking already-formed organoids exhibiting properties of interest, and expanding them through re-seeding might constitute a worthy avenue for narrowing the heterogeneity in development when experimentally needed.

2.2 Imaging challenges

Beyond the difficulties stemming from the phenotypical heterogeneity in organoid culture, imaging constitutes an additional challenge.

Indeed, PDAC organoids are highly three-dimensional and can reach millimetres in height which requires a large objective distance. Moreover, the gels are floating in the wells, adding a supplementary “dead” distance to cover for the objective, that is particularly problematic for high-magnification objectives that tend to possess short working distances.

Organoids may furthermore drift over the course of imaging, which requires interrupting the measurement for recentring, or post-experiment algorithmic corrections (if the drift is manageable).

Drift could be mitigated by reducing the volume of medium in the wells, but reducing the amount of medium excessively may lead to an insufficient nutrient supply, altering the development dynamics or causing the organoids to die.

2.3 Analysis challenges

As stated above, the heterogeneity in organoid culture complexifies the analysis of experiments. When treating organoids with a drug, should the difference in phenotypes be considered in the reporting statistics? When setting up a limited number of positions for confocal live imaging, should an experimentalist prioritise imaging similar-looking organoids and thus run the risk of committing “cherry-picking”, or elect to image different-looking organoids and thus run the risk of not being able to discern stereotypical behaviours.⁴

Similarly, knowing the heterogeneity of organoid culture, should an experimentalist consider the different organoids growing in a single well as different replicates? How about organoids growing in a multi-well? How about organoids cultured on different days?

Another challenge lies in the fact that a considerable fraction of the analysis has (or had) to be performed manually. For novel experiments in particular, the parameter to measure is not necessarily obvious, and drug treatment may indeed have effects that

⁴Note that in an ideal world with infinite resources, infinite microscope time, infinite contract duration, and infinite patience, the ideal experimentalist can overcome this challenge by imaging as many times as needed. Such conditions however rarely manifest in practice.

are not easily detectable via automated analysis, or where automating the analysis is difficult.

Unevenness in image quality due to experimental differences in height of the floating gels, size of organoids, presence of a cell monolayer obscuring part or entirety of organoids, or inhomogeneities in the collagen structure and brightness, sometimes further compounded by differences in microscope, settings, experimentalists, can be challenging for image analysis algorithms.

The variability in organoid shapes makes “averaging” properties difficult, and potentially dangerous if done carelessly, as it may obfuscate important differences between phenotypes.

Fortunately, the development of fluorescent markers (exogenously added or endogenously expressed), is making the automation of quantitative analysis possible, notably by allowing the segmentation of illuminated structures of interest.

In conjunction with the recent emergence of deep learning-based tools such as *ilastik* and *Arivis* that can analyse structures painted by the user - without having to specify explicitly the features that characterise them - and generalise on unlabelled datasets, future studies will certainly prove more quantitative than the preliminary work reported in this thesis.

Automated analysis, when properly performed, allows the processing of a large number of samples, the standardisation of measurements, and may pick up subtle variations in images that could otherwise go unnoticed to the experimentalist.

Automated analysis may also help lower the human errors that may appear when working on large datasets, although it should be noted that deep learning models are not entirely free of biases, as they rely on training datasets that are ultimately labelled by a human. Making the bias *systematic* rather than *random* probably constitutes an improvement overall.

Lastly, the fact that PDAC organoids were embedded in a matrix makes a number of experiments difficult. In particular, the quantification of material properties such as the viscoelasticity of organoids or the strength of cell-cell adhesion could not (at the time of writing) be tested through the traditional means of micropipette aspiration for example [220], as inserting the pipette would damage the matrix. Similarly, lumens in organoids could not be accessed from the outside, which made the real time analysis of their content impossible [119].

However, the work presented in this thesis represents only a preliminary step in the study of PDAC organoids. Future experiments such as careful deformation of organoids using microneedles without ECM destruction, or embedding of organoids inside a microfluidic chip to open access to the inner lumen, should provide crucial quantitative data. Likewise, microneedles could allow careful penetration inside the lumens for the analysis of their content and osmolarity.

For lumen content analysis, fluorophores with emissions dependent on an environmental parameter of interest could be considered. To study the pH of the intra-luminal fluid for instance, pH-dependent fluorophores such as quantum dots, metal nanoclusters or carbon-based nanosensors could be deployed [221].

3 Additional methods

This section contains, for completeness, a description of methods that were used by collaborators to obtain results published in [8].

3.1 Two-dimensional (2D) cell culture of pancreatic ductal cells (PDCs)

The healthy adult pancreatic ductal cells (PDCs) were cultured as described in [222].

Briefly, cells were seeded on collagen coated plates (a 3mL collagen type I layer (2.31 mg/mL) on a tissue culture dish), and were grown in PDC medium: DMEM/F-12 (Thermo Fisher Scientific), 5 mg/mL D-glucose (Sigma Aldrich), 0.5% ITS premix (Corning), 5% Nu-Serum (Corning), 1x Penicillin/Streptomycin (Thermo Fisher Scientific), 25 µg/mL Bovine Pituitary Extract (Thermo Fisher Scientific), 100 ng/mL Cholera Toxin (Sigma Aldrich), 1 µM Dexamethasone (Sigma Aldrich), 10mM Nicotinamide (Sigma Aldrich), 100 µg/mL Primocin (Invivogen) and 20 ng EGF (R&D systems). Media changes were performed every 48 h and upon 80-85% confluency the collagen was further digested for 15 min at 37 °C with 1.5mg/mL Collagenase Type 4 (Worthington) diluted in DMEM/F-12. Cold PBS was then added, and the mixture was centrifugated. The cell pellet was then trypsinized and Soybean Trypsin Inhibitor (STI) was used to quench the effect of trypsin. Afterwards, 10000 cells were seeded into collagen gels (as described in “Organoid preparation” (5.3.2)).

3.2 Orthotopic implantation into mice

Mice were anaesthetised using MMF (5 mg/kg midazolam, 500 µg/kg medetomidine, 50 µg/kg fentanyl) and after a small abdominal incision the spleen was exposed by gentle pull. 2500 cells were carefully injected into the pancreas using a microlitre syringe with a 27-gauge needle. Thereafter, the incision was closed and MMF anaesthesia was antagonized by injecting AFN (750 µg/kg atipamezole, 500 µg/kg flumazenil, 1.2 mg/kg naloxone). Mice were monitored postoperatively on a daily basis regarding general health status as well as bodyweight. After 2-3 weeks, mice were sacrificed, and tumour tissue was harvested and fixed with 4% PFA.

3.3 Histology

Organoids were fixed as described above in 4% PFA. For orthotopically implanted tumours, tissues were fixed in formalin (10%) overnight, dehydrated, and embedded in paraffin. Hematoxylin and eosin (H&E) staining was performed as previously published[23].

Briefly, paraffin-embedded sections were de-waxed in xylene (two times, 5 min each), and rehydrated first in isopropanol (2 times, 5min each), and then in decreasing ethanol concentrations (at 96% two times, 2min each, and at 70% two times, 2min each). Sections were rinsed with distilled water for 25 s, and were stained with Mayer’s Hematoxylin for 8 min. Sections were then rinsed in tap water for 10 min, before applying a 1% alcoholic solution of eosin for counterstaining, for 4 min. Following this, the slides were passed in

ethanol (96%, 30 s), isopropanol (2 times, 25 s each), and xylene (2 times, 1 min 30 s each).

For the immunofluorescence of tissue and organoid sections, slides were first deparaffinized, then immersed into unmasking solution (Vector Laboratories) for 10 min at 360 V in a microwave, and afterwards washed sequentially with dH₂O and DPBS and blocked (0.5% BSA/0.5% Triton-X 100 in DPBS) for 1 h at room temperature. Primary antibody diluted in blocking solution was added for overnight incubation. Next, slides were washed 3x with DPBS and secondary antibodies were incubated for 1 h at room temperature and DAPI was used for staining the nuclei.

3.4 RNA-isolation

Cells grown in 2D cultures were directly collected in RLT buffer with β -Mercaptoethanol, while the 3D organoids were first digested for 12-15 min at 37 °C with 1.5 mg/mL Collagenase Type 4 (Worthington) in DMEM supplemented only with Penicillin/Streptomycin until complete matrix digestion. The organoids then were washed once with DPBS and further collected in RLT buffer with β -Mercaptoethanol until further use. Before the RNA isolation, we homogenized the cells/organoids lysates using QIAshredder (Qiagen). Total RNA was isolated using the RNeasy Plus Micro Kit (Qiagen) according to the manufacturer's instructions, with the addition of a 15min on column DNA digestion step using RNase-Free DNase set (Qiagen).

3.5 RNA-sequencing

Library preparation for bulk-sequencing of poly(A)-RNA was done as described previously [223]. Briefly, barcoded cDNA of each sample was generated with a Maxima RT polymerase (Thermo Fisher) using oligo-dT primer containing barcodes, unique molecular identifiers (UMIs) and an adapter. Ends of the cDNAs were extended by a template switch oligo (TSO) and full-length cDNA was amplified with primers binding to the TSO-site and the adapter. NEB UltraII FS kit was used to fragment cDNA. After end repair and A-tailing, a TruSeq adapter was ligated and 3'-end-fragments were finally amplified using primers with Illumina P5 and P7 overhangs. In comparison to Parekh et al. [223], the P5 and P7 sites were exchanged to allow sequencing of the cDNA in read1 and barcodes and UMIs in read2 to achieve a better cluster recognition. The library was sequenced on a NextSeq 500 (Illumina) with 63 cycles for the cDNA in read1 and 16 cycles for the barcodes and UMIs in read2. Data was processed using the published Drop-seq pipeline (ver. 1.0) to generate sample- and gene-wise UMI tables. Reference genome (GRCm38) was used for alignment [224].

Transcript and gene definitions were used according to the GENCODE Version M25. Heatmaps shown display the log₂ fold change.

3.6 Statistical analysis of gene expression data

High-throughput gene expression data from the conditions indicated in the text were carried out using the R environment for statistical computing [225] (v4.0.4). Differential

Appendix

gene expression analysis Genome-wide differential gene expression analysis for RNA-Seq count data was carried out using a negative binomial generalised linear model as implemented in the DESeq2 R package[226] to test for differentially expressed genes between experimental conditions.

For dispersion estimates we considered the following covariates: cell line, genotype, dimension (2D, 3D), extracellular matrix composition (none, collagen, Matrigel) and time (7days, 13 days). For individual comparisons, a false discovery rate (FDR) <0.1 was considered significant. Gene set enrichment analysis Gene set enrichment analysis (GSEA) was carried out on individual differential gene expression signatures between two conditions as represented using the fgsea R package [227] and using Wald statistics as gene-level statistics. Gene sets were retrieved from the MSigDb v7.3[228, 229]. Enrichment results for select pathways were illustrated using custom R code. For select pathways, leading edge genes were illustrated between two conditions after scaling all rows to have mean 0 and variance 1 (Z-score transformation) using the *heatmap* R package[230].

Bibliography

- [1] American Cancer Society. American Cancer Society. Cancer Facts & Figures 2020, 2020.
- [2] Aleksandra Adamska, Alice Domenichini, and Marco Falasca. Pancreatic Ductal Adenocarcinoma: Current and Evolving Therapies. *International Journal of Molecular Sciences*, 18(7):1338, jun 2017.
- [3] Natalia Juiz, Abdessamad Elkaoutari, Martin Bigonnet, Odile Gayet, Julie Roques, Rémy Nicolle, Juan Iovanna, and Nelson Dusetti. Basal-like and classical cells coexist in pancreatic cancer revealed by single-cell analysis on biopsy-derived pancreatic cancer organoids from the classical subtype. *The FASEB Journal*, 34(9):12214–12228, 2020.
- [4] Victoria M Wang, Rute M M Ferreira, Jorge Almagro, Theodore Evan, Nathalie Legrave, May Zaw Thin, David Frith, Joana Carvalho, David J Barry, Ambrosius P Snijders, Eleanor Herbert, Emma L Nye, James I Macrae, and Axel Behrens. CD9 identifies pancreatic cancer stem cells and modulates glutamine metabolism to fuel tumour growth. *Nature Cell Biology*, 21(November), 2019.
- [5] Olca Basturk, Seung-Mo Hong, Laura D. Wood, N. Volkan Adsay, Jorge Albores-Saavedra, Andrew V. Biankin, Lodewijk A.A. Brosens, Noriyoshi Fukushima, Michael Goggins, Ralph H. Hruban, Yo Kato, David S. Klimstra, Günter Klöppel, Alyssa Krasinskas, Daniel S. Longnecker, Hanno Matthaei, G. Johan A. Offerhaus, Michio Shimizu, Kyoichi Takaori, Benoit Terris, Shinichi Yachida, Irene Esposito, and Toru Furukawa. A revised classification system and recommendations from the Baltimore consensus meeting for neoplastic precursor lesions in the pancreas. *American Journal of Surgical Pathology*, 39(12):1730–1741, 2015.
- [6] V Adsay, M Mino-Kenudson, T Furukawa, O Basturk, G Zamboni, G Marchegiani, C Bassi, R Salvia, G Malleo, S Paiella, CL Wolfgang, H Matthaei, GJ Offerhaus, M Adham, MJ Bruno, MD Reid, A Krasinskas, G Klöppel, N Ohike, T Tajiri, KT Jang, JC Roa, P Allen, Castillo C Fernández-del, JY Jang, DS Klimstra, RH Hruban, and Members of Verona Consensus Meeting 2013. Pathologic evaluation and reporting of intraductal papillary mucinous neoplasms (IPMNS) of the pancreas and other tumoral intraepithelial neoplasms of pancreatobiliary tract: Recommendations of Verona consensus meeting. *Ann. Surg.*, 263(1):162–177, 2016.
- [7] Ashley L. Kiemen, Alicia M. Braxton, Mia P. Grahn, Kyu Sang Han, Jaanvi Mahesh Babu, Rebecca Reichel, Ann C. Jiang, Bridgette Kim, Jocelyn Hsu, Falcone Amoa, Sashank Reddy, Seung Mo Hong, Toby C. Cornish, Elizabeth D.

Bibliography

- Thompson, Peng Huang, Laura D. Wood, Ralph H. Hruban, Denis Wirtz, and Pei Hsun Wu. CODA: quantitative 3D reconstruction of large tissues at cellular resolution. *Nature Methods*, 19(11):1490–1499, 2022.
- [8] Samuel Randriamanantsoa, Aristeidis Papargyriou, Carlo Maurer, Katja Peschke, Maximilian Schuster, Giulia Zecchin, Katja Steiger, Rupert Öllinger, Dieter Saur, Christina Scheel, Roland Rad, Edouard Hannezo, Maximilian Reichert, and Andreas R. Bausch. Spatiotemporal dynamics of self-organized branching in pancreas-derived organoids. *Nature Communications*, 2022.
- [9] World Health Organization. Cancer, 2022.
- [10] Simiao Chen, Zhong Cao, Klaus Prettner, Michael Kuhn, Juntao Yang, Lirui Jiao, Zhuoran Wang, Weimin Li, Pascal Geldsetzer, Till Bärnighausen, David E. Bloom, and Chen Wang. Estimates and Projections of the Global Economic Cost of 29 Cancers in 204 Countries and Territories from 2020 to 2050. *JAMA Oncology*, 9(4):465–472, 2023.
- [11] National Institute of Health. Estimates of Funding for Various Research, Condition, and Disease Categories (RCDC), 2023.
- [12] American Cancer Society. 2023 Cancer Facts and Figures, 2023.
- [13] Mark S Duxbury, Stanley W Ashley, and Edward E Whang. Inhibition of pancreatic adenocarcinoma cellular invasiveness by blebbistatin: a novel myosin II inhibitor. 313:992–997, 2004.
- [14] Toshiro Sato, Robert G. Vries, Hugo J. Snippert, Marc Van De Wetering, Nick Barker, Daniel E. Stange, Johan H. Van Es, Arie Abo, Pekka Kujala, Peter J. Peters, and Hans Clevers. Single Lgr5 stem cells build crypt-villus structures in vitro without a mesenchymal niche. *Nature*, 459(7244):262–265, 2009.
- [15] Madeline Lancaster, Takanori Takebe, and Madeline Lancaster. Advances in Organoid Technology: Hans Clevers, Madeline Lancaster, and Takanori Takebe. *Cell Stem Cell*, 20(6):759–762, 2017.
- [16] C. Greggio, F. De Franceschi, M. Figueiredo-Larsen, S. Gobaa, A. Ranga, H. Semb, M. Lutolf, and A. Grapin-Botton. Artificial three-dimensional niches deconstruct pancreas development in vitro. *Development*, 140(21):4452–4462, 2013.
- [17] Meritxell Huch, Paola Bonfanti, Sylvia F. Boj, Toshiro Sato, Cindy J.M. Loomans, Marc Van De Wetering, Mozhdeh Sojoodi, Vivian S.W. Li, Jurian Schuijers, Ana Gracanin, Femke Ringnalda, Harry Begthel, Karien Hamer, Joyce Mulder, Johan H. Van Es, Eelco De Koning, Robert G.J. Vries, Harry Heimberg, and Hans Clevers. Unlimited in vitro expansion of adult bi-potent pancreas progenitors through the Lgr5/R-spondin axis. *EMBO Journal*, 32(20):2708–2721, 2013.

- [18] Sylvia F Boj, Chang-il Hwang, Lindsey A Baker, Iok In, Christine Chio, Dannielle D Engle, Vincenzo Corbo, Myrthe Jager, Mariano Ponz-sarvise, Tobiloba Oni, Kenneth H Yu, Ruben Van Boxtel, Meritxell Huch, Keith D Rivera, John P Wilson, Abram Handly-santana, Christine M Ardito-abraham, Michael Ludwig, Michael E Feigin, O Daniel, Ela Elyada, Brinda Alagesan, Giulia Biffi, Georgi N Yordanov, Bethany Delcuze, Brianna Creighton, Kevin Wright, Youngkyu Park, Folkert H M Morsink, I Quintus Molenaar, Inne H Borel Rinkes, Edwin Cuppen, Yuan Hao, Ying Jin, Isaac J Nijman, Christine Iacobuzio-donahue, Steven D Leach, Darryl J Pappin, Molly Hammell, David S Klimstra, Olca Basturk, Ralph H Hruban, George Johan Offerhaus, Robert G J Vries, Hans Clevers, and David A Tuveson. Organoid Models of Human and Mouse Ductal Pancreatic Cancer. *Cell*, 160:324–338, 2015.
- [19] Laura Broutier, Amanda Andersson-Rolf, Christopher J. Hindley, Sylvia F. Boj, Hans Clevers, Bon Kyoung Koo, and Meritxell Huch. Culture and establishment of self-renewing human and mouse adult liver and pancreas 3D organoids and their genetic manipulation. *Nature Protocols*, 2016.
- [20] Leticia Moreira, Basil Bakir, Priya Chatterji, Zahra Dantes, Maximilian Reichert, and Anil K. Rustgi. Pancreas 3D Organoids: Current and Future Aspects as a Research Platform for Personalized Medicine in Pancreatic Cancer. *Cmgh*, 5(3):289–298, 2018.
- [21] Hervé Tiriach, Pascal Belleau, Dannielle D. Engle, Dennis Plenker, Astrid Deschênes, Tim D.D. Somerville, Fieke E.M. Froeling, Richard A. Burkhardt, Robert E. Denroche, Gun Ho Jang, Koji Miyabayashi, C. Megan Young, Hardik Patel, Michelle Ma, Joseph F. Lacombe, Randze Lerie D. Palmaira, Ammar A. Javed, Jasmine C. Huynh, Molly Johnson, Kanika Arora, Nicolas Robine, Minita Shah, Rashesh Sanghvi, Austin B. Goetz, Cinthya Y. Lowder, Laura Martello, Else Driehuis, Nicolas Lecomte, Gokce Askan, Christine A. Iacobuzio-Donahue, Hans Clevers, Laura D. Wood, Ralph H. Hruban, Elizabeth Thompson, Andrew J. Aguirre, Brian M. Wolpin, Aaron Sasson, Joseph Kim, Maoxin Wu, Juan Carlos Bucobo, Peter Allen, Divyesh V. Sejpal, William Nealon, James D. Sullivan, Jordan M. Winter, Phyllis A. Gimotty, Jean L. Grem, Dominick J. Dimaiio, Jonathan M. Buscaglia, Paul M. Grandgenett, Jonathan R. Brody, Michael A. Hollingsworth, Grainne M. O’kane, Faiyaz Notta, Edward Kim, James M. Crawford, Craig Devoe, Allyson Ocean, Christopher L. Wolfgang, Kenneth H. Yu, Ellen Li, Christopher R. Vakoc, Benjamin Hubert, Sandra E. Fischer, Julie M. Wilson, Richard Moffitt, Jennifer Knox, Alexander Krasnitz, Steven Gallinger, and David A. Tuveson. Organoid profiling identifies common responders to chemotherapy in pancreatic cancer. *Cancer Discovery*, 8(9):1112–1129, 2018.
- [22] Else Driehuis, Arne Van Hoeck, Kat Moore, Sigrid Kolders, Hayley E. Francies, M. Can Gulersonmez, Edwin C.A. Stigter, Boudewijn Burgering, Veerle Geurts, Ana Gracanin, Gergana Bounova, Folkert H. Morsink, Robert Vries, Sylvia Boj,

Bibliography

- Johan Van Es, G. Johan A. Offerhaus, Onno Kranenburg, Mathew J. Garnett, Lodewyk Wessels, Edwin Cuppen, Lodewijk A.A. Brosens, and Hans Clevers. Pancreatic cancer organoids recapitulate disease and allow personalized drug screening. *Proceedings of the National Academy of Sciences of the United States of America*, 116(52):26580–26590, 2019.
- [23] Zahra Dantes, Hsi-Yu Yen, Nicole Pfarr, Christof Winter, Katja Steiger, Alexander Muckenhuber, Alexander Hennig, Sebastian Lange, Thomas Engleitner, Rupert Öllinger, Roman Maresch, Felix Orben, Irina Heid, Georgios Kaisis, Kuangyu Shi, Geoffrey Topping, Fabian Stögbauer, Matthias Wirth, Katja Peschke, Aristeidis Papargyriou, Massoud Rezaee-Oghazi, Karin Feldmann, Arlett P G Schäfer, Raphela Ranjan, Clara Lubeseder-Martellato, Daniel E Stange, Thilo Welsch, Marc Martignoni, Güralp O Ceyhan, Helmut Friess, Alexander Herner, Lucia Liotta, Matthias Treiber, Guido von Figura, Mohamed Abdelhafez, Peter Klare, Christoph Schlag, Hana Algül, Jens Siveke, Rickmer Braren, Gregor Weirich, Wilko Weichert, Dieter Saur, Roland Rad, Roland M Schmid, Günter Schneider, and Maximilian Reichert. Implementing cell-free DNA of pancreatic cancer patient-derived organoids for personalized oncology. *JCI Insight*, 5(15), aug 2020.
- [24] Darren Gilmour, Martina Rembold, and Maria Leptin. From morphogen to morphogenesis and back. *Nature*, 541(7637):311–320, 2017.
- [25] Ray Keller. Physical Biology Returns to Morphogenesis. *Science*, 338(October):201–204, 2012.
- [26] D’Arcy Wentworth Thomson. *On Growth and Form*. Cambridge University Press, Cambridge, 1st edition, 1917.
- [27] D’Arcy Wentworth Thomson. *On Growth and Form*. Cambridge University Press, Cambridge, 2nd edition, 1942.
- [28] François Graner and Daniel Riveline. ‘The forms of tissues, or cell-aggregates’: D’arcy thompson’s influence and its limits. *Development (Cambridge)*, 144(23):4226–4237, 2017.
- [29] Claudio Collinet and Thomas Lecuit. Programmed and self-organized flow of information during morphogenesis. *Nature Reviews Molecular Cell Biology*, 22(4):245–265, 2021.
- [30] Philipp J. Keller. Imaging Morphogenesis: Technological Advances and Biological Insights. *Science*, 340, 2013.
- [31] Jaime A. Espina, Marilia H. Cordeiro, and Elias H. Barriga. Tissue interplay during morphogenesis. *Seminars in Cell and Developmental Biology*, 147(March):12–23, 2023.

- [32] Tina Jaskoll and Michael Melnick. Submandibular gland morphogenesis: Stage-specific expression of TGF- α /EGF, IGF, TGF- β , TNF, and IL-6 signal transduction in normal embryonic mice and the phenotypic effects of TGF- β 2, TGF- β 3, and EGF-r null mutations. *The Anatomical Record*, 256(3):252–268, nov 1999.
- [33] Deborah J Andrew and Andrew J Ewald. Morphogenesis of epithelial tubes: Insights into tube formation, elongation and elaboration. *Cell*, 341(1):34–55, 2011.
- [34] Tony Y-C Tsai, Mateusz Sikora, Peng Xia, Tugba Colak-Champollion, Holger Knaut, Carl-Philipp Heisenberg, and Sean G Megason. An adhesion code ensures robust pattern formation during tissue morphogenesis. *Science (New York, N.Y.)*, 370(6512):113–116, 2020.
- [35] Takashi Miura. Models of lung branching morphogenesis. *Journal of Biochemistry*, 157(3):121–127, 2015.
- [36] Anette Funfak, Latifa Bouzahir, Emilie Gontran, Nicolas Minier, Pascale Dupuis-Williams, and Samy Gobaa. Biophysical Control of Bile Duct Epithelial Morphogenesis in Natural and Synthetic Scaffolds. *Frontiers in Bioengineering and Biotechnology*, 7(December):1–11, 2019.
- [37] Hendrik A. Messal, Silvanus Alt, Rute M.M. Ferreira, Christopher Gribben, Victoria Min Yi Wang, Corina G. Cotoi, Guillaume Salbreux, and Axel Behrens. Tissue curvature and apicobasal mechanical tension imbalance instruct cancer morphogenesis. *Nature*, 566(7742):126–130, 2019.
- [38] Mohammad Iqbal Choudhury, Morgan A. Benson, and Sean X. Sun. Trans-epithelial fluid flow and mechanics of epithelial morphogenesis. *Seminars in Cell and Developmental Biology*, 131(April):146–159, 2022.
- [39] Dagmar Iber and Denis Menshykau. The control of branching morphogenesis. *Open Biology*, 3(SEP), 2013.
- [40] Katharine Goodwin and Celeste M Nelson. Branching morphogenesis. *Development*, 147, 2020.
- [41] Edouard Hannezo, Colinda L.G.J. Scheele, Mohammad Moad, Nicholas Drogo, Rakesh Heer, Rosemary V. Sampogna, Jacco van Rheenen, and Benjamin D. Simons. A Unifying Theory of Branching Morphogenesis. *Cell*, 171(1):242–255.e27, 2017.
- [42] Ignacio Bordeu, Lemonia Chatzeli, and Benjamin D. Simons. Inflationary theory of branching morphogenesis in the mouse salivary gland. *Nature Communications*, 14(1):1–11, 2023.
- [43] Edouard Hannezo and Benjamin D. Simons. Multiscale dynamics of branching morphogenesis. *Current Opinion in Cell Biology*, 60:99–105, 2019.

Bibliography

- [44] Lydie Flasse, Coline Schewin, and Anne Grapin-Botton. Pancreas morphogenesis: Branching in and then out. *Current Topics in Developmental Biology*, 143:75–110, 2021.
- [45] Mette Christine Jørgensen, Jonas Ahnfelt-Rønne, Jacob Hald, Ole D. Madsen, Palle Serup, and Jacob Hecksher-Sørensen. An illustrated review of early pancreas development in the mouse. *Endocrine Reviews*, 28(6):685–705, 2007.
- [46] Alethia Villasenor, Diana C Chong, Mark Henkemeyer, and Ondine Cleaver. Epithelial dynamics of pancreatic branching morphogenesis. *Development*, 4305:4295–4305, 2010.
- [47] Anne Christine Hick, Jonathan M. Van Eyll, Sabine Cordi, Céline Forez, Lara Passante, Hiroshi Kohara, Takashi Nagasawa, Pierre Vanderhaeghen, Pierre J. Courtoy, Guy G. Rousseau, Frédéric P. Lemaigre, and Christophe E. Pierreux. Mechanism of primitive duct formation in the pancreas and submandibular glands: A role for SDF-1. *BMC Developmental Biology*, 9(1):1–17, 2009.
- [48] Leilani Marty-Santos and Ondine Cleaver. Pdx1 regulates pancreas tubulogenesis and E-cadherin expression Pdx1 regulates pancreas tubulogenesis and E-cadherin expression. pages 101–112, 2016.
- [49] Sara Sigurbjörnsdóttir, Renjith Mathew, and Maria Leptin. Molecular mechanisms of de novo lumen formation. *Nature Reviews Molecular Cell Biology*, 15(10):665–676, 2014.
- [50] R C Humphreys, M Krajewska, S Krnacik, R Jaeger, H Weiher, S Krajewski, J C Reed, and J M Rosen. Apoptosis in the terminal endbud of the murine mammary gland: a mechanism of ductal morphogenesis. *Development*, 122(12):4013–4022, 1996.
- [51] Gokul Kesavan, Fredrik Wolfhagen Sand, Thomas Uwe Greiner, Jenny Kristina Johansson, Sune Kobberup, Xunwei Wu, Cord Brakebusch, and Henrik Semb. Cdc42-Mediated Tubulogenesis Controls Cell Specification. *Cell*, 139(4):791–801, 2009.
- [52] D. Berfin Azizoglu, Caitlin Braitsch, Denise K. Marciano, and Ondine Cleaver. Afadin and Rhoa control pancreatic endocrine mass via lumen morphogenesis. *Genes and Development*, 31(23-24):2376–2390, 2017.
- [53] Kristin M. Petzold, Heike Naumann, and Francesca M. Spagnoli. Rho signalling restriction by the RhoGAP Stard13 integrates growth and morphogenesis in the pancreas. *Development (Cambridge)*, 140(1):126–135, 2013.
- [54] Magdalena K. Sznurkowska, Edouard Hannezo, Roberta Azzarelli, Steffen Rulands, Sonia Nestorowa, Christopher J. Hindley, Jennifer Nichols, Berthold Göttgens, Meritxell Huch, Anna Philpott, and Benjamin D. Simons. Defining

- Lineage Potential and Fate Behavior of Precursors during Pancreas Development. *Developmental Cell*, 46(3):360–375.e5, 2018.
- [55] Jean-francois Darrigrand, Anna Salowka, Alejo Torres-cano, Rafael Tapia-rojo, Tong Zhu, Sergi Garcia-manyes, Francesca M Spagnoli, Jean-francois Darrigrand, Anna Salowka, Alejo Torres-cano, Rafael Tapia-rojo, and Tong Zhu. Article Acinar-ductal cell rearrangement drives branching morphogenesis of the murine pancreas in an IGF / PI3K-dependent manner Article Acinar-ductal cell rearrangement drives branching morphogenesis of the murine pancreas in an IGF / PI3K-dependent mann. *Developmental Cell*, pages 1–13, 2024.
- [56] Sapna Puri and Matthias Hebrok. Dynamics of embryonic pancreas development using real-time imaging. *Developmental Biology*, 306(1):82–93, 2007.
- [57] Shaohe Wang, Rei Sekiguchi, William P. Daley, and Kenneth M. Yamada. Cell and matrix dynamics in branching morphogenesis. *Journal of Cell Biology*, 216(3):559–570, 2017.
- [58] Svend Bertel Dahl-Jensen, Siham Yennek, Lydie Flasse, Hjalte List Larsen, Dror Sever, Gopal Karremore, Ivana Novak, Kim Sneppen, and Anne Grapin-Botton. Deconstructing the principles of ductal network formation in the pancreas. *PLoS Biology*, 16(7):1–25, 2018.
- [59] Jurij Dolenšek, Marjan Slak Rupnik, and Andraž Stožer. Structural similarities and differences between the human and the mouse pancreas, 2015.
- [60] M. I. Kairaluoma, M. Ståhlberg, and H. Kiviniemi. Pancreatic resection for carcinoma of the pancreas and the periampullary region in patients over 70 years of age. *British Journal of Surgery*, 74:116–118, 1987.
- [61] Taylor A. Sohn, Charles J. Yeo, John L. Cameron, Leonidas Koniaris, Sunjay Kaushal, Ross A. Abrams, Patricia K. Sauter, Joann Coleman, Ralph H. Hruban, and Keith D. Lillemoe. Resected Adenocarcinoma of the Pancreas - 616 Patients: Results, Outcomes, and Prognostic Indicators. *Journal of Gastrointestinal Surgery*, 4(6):567–579, 2000.
- [62] Johns Hopkins Medicine. Whipple Procedure.
- [63] Ning Zhang, Ying Yin, Sheng Jie Xu, and Wei Shan Chen. 5-Fluorouracil: Mechanisms of resistance and reversal strategies. *Molecules*, 13(8):1551–1569, 2008.
- [64] H A 3rd Burris, M J Moore, J Andersen, M R Green, M L Rothenberg, M R Modiano, M C Cripps, R K Portenoy, A M Storniolo, P Tarassoff, R Nelson, F A Dorr, C D Stephens, and D D Von Hoff. Improvements in survival and clinical benefit with gemcitabine as first-line therapy for patients with advanced pancreas cancer: a randomized trial. *Journal of clinical oncology : official journal of the American Society of Clinical Oncology*, 15(6):2403–2413, jun 1997.

Bibliography

- [65] Stuart Noble and Karen L. Goa. Gemcitabine. *Drugs*, 54(3):447–472, 1997.
- [66] Ashton A. Connor and Steven Gallinger. Pancreatic cancer evolution and heterogeneity: integrating omics and clinical data. *Nature Reviews Cancer*, 22(3):131–142, 2022.
- [67] N. Volkan Adsay, Olca Basturk, Michelle Bonnett, Nihal Kilinc, Aleodor A. Andea, Jining Feng, Mingxin Che, Michael R. Aulicino, Edi Levi, and Jeanette D. Cheng. A proposal for a new and more practical grading scheme for pancreatic ductal adenocarcinoma. *American Journal of Surgical Pathology*, 29(6):724–733, 2005.
- [68] Natalia Anahi Juiz, Juan Iovanna, and Nelson Duseti. Pancreatic cancer heterogeneity can be explained beyond the genome. *Frontiers in Oncology*, 9(APR):1–8, 2019.
- [69] Xiphias Ge Zhu and Kivanc Birsoy. Deciphering cellular heterogeneity of pancreatic. 21(November):1305–1306, 2019.
- [70] Ralph H Hruban, Kyoichi Takaori, David S Klimstra, N Volkan Adsay, Jorge Albores-Saavedra, Andrew V Biankin, Sandra A Biankin, Carolyn Compton, Noriyoshi Fukushima, Toru Furukawa, Michael Goggins, Yo Kato, Gunter Kloppel, Daniel S Longnecker, Jutta Luttges, Anirban Maitra, G Johan A Offerhaus, Michio Shimizu, and Suguru Yonezawa. An Illustrated Consensus on the Classification of Pancreatic. *The American Journal of Surgical Pathology*, 28(8):977–987, 2004.
- [71] M. Distler, D. Aust, J. Weitz, C. Pilarsky, and Robert Grützmann. Precursor lesions for sporadic pancreatic cancer: PanIN, IPMN, and MCN. *BioMed Research International*, 2014, 2014.
- [72] T. J. Puls, Xiaohong Tan, Catherine F. Whittington, and Sherry L. Voytik-Harbin. 3D collagen fibrillar microstructure guides pancreatic cancer cell phenotype and serves as a critical design parameter for phenotypic models of EMT. *PLoS ONE*, 12(11):1–25, 2017.
- [73] Friederike V. Opitz, Lena Haeberle, Alexandra Daum, and Irene Esposito. Tumor microenvironment in pancreatic intraepithelial neoplasia. *Cancers*, 13(24), 2021.
- [74] Hadi T. Nia, Lance L. Munn, and Rakesh K. Jain. Physical traits of cancer. *Science*, 370(6516), 2020.
- [75] Kenneth P Olive, Michael a Jacobetz, Christian J Davidson, Aarthi Gopinathan, Dominick McIntyre, Davina Honess, Basetti Madhu, Mae a Goldgraben, Meredith E Caldwell, David Allard, Kristopher K Frese, Gina DeNicola, Christine Feig, Chelsea Combs, Stephen P. Winter, Heather Ireland-Zecchini, Stefanie Reichelt, William J Howat, Alex Chang, Mousumi Dhara, Lifu Wang, Felix Rückert, Robert Grützmann, Christian Pilarsky, Kamel Izeradjene, Sunil R Hingorani, Pearl Huang, Susan E Davies, William Plunkett, Merrill Egorin, Ralph H

- Hruban, Nigel Whitebread, Karen McGovern, Julian Adams, Christine Iacobuzio-Donahue, John Griffiths, and David a Tuveson. Inhibition of Hedgehog Signaling Enhances Delivery of Chemotherapy in a Mouse Model of Pancreatic Cancer. *Science*, 324(June):1457–61, 2011.
- [76] Jesse Gore and Murray Korc. Pancreatic Cancer Stroma: Friend or Foe? *Cancer Cell*, 25(6):711–712, 2014.
- [77] Andrew D. Rhim, Paul E. Oberstein, Dafydd H. Thomas, Emily T. Mirek, Carmine F. Palermo, Stephen A. Sastra, Erin N. Dekleva, Tyler Saunders, Claudia P. Becerra, Ian W. Tattersall, C. Benedikt Westphalen, Jan Kitajewski, Maite G. Fernandez-Barrena, Martin E. Fernandez-Zapico, Christine Iacobuzio-Donahue, Kenneth P. Olive, and Ben Z. Stanger. Stromal elements act to restrain, rather than support, pancreatic ductal adenocarcinoma. *Cancer Cell*, 25(6):735–747, 2014.
- [78] Berna C. Özdemir, Tsvetelina Pentcheva-Hoang, Julienne L. Carstens, Xiaofeng Zheng, Chia Chin Wu, Tyler R. Simpson, Hanane Laklai, Hikaru Sugimoto, Christoph Kahlert, Sergey V. Novitskiy, Ana DeJesus-Acosta, Padmanee Sharma, Pedram Heidari, Umar Mahmood, Lynda Chin, Harold L. Moses, Valerie M. Weaver, Anirban Maitra, James P. Allison, Valerie S. LeBleu, and Raghu Kalluri. Depletion of carcinoma-associated fibroblasts and fibrosis induces immunosuppression and accelerates pancreas cancer with reduced survival. *Cancer Cell*, 25(6):719–734, 2014.
- [79] Elisabete C. Costa, André F. Moreira, Duarte de Melo-Diogo, Vítor M. Gaspar, Marco P. Carvalho, and Ilídio J. Correia. 3D tumor spheroids: an overview on the tools and techniques used for their analysis. *Biotechnology Advances*, 34(8):1427–1441, 2016.
- [80] Kayla Duval, Hannah Grover, Li Hsin Han, Yongchao Mou, Adrian F. Pegoraro, Jeffery Fredberg, and Zi Chen. Modeling physiological events in 2D vs. 3D cell culture. *Physiology*, 32(4):266–277, 2017.
- [81] Caleb Jensen and Yong Teng. Is It Time to Start Transitioning From 2D to 3D Cell Culture? *Frontiers in Molecular Biosciences*, 7(March):1–15, 2020.
- [82] Meritxell Huch, Juergen A Knoblich, Matthias P Lutolf, and Alfonso Martinez-Arias. The hope and the hype of organoid research. *Development*, 144(6):938–941, mar 2017.
- [83] Sylvia F. Boj, Annelotte M. Vonk, Marvin Statia, Jinyi Su, Robert R.G. Vries, Jeffrey M. Beekman, and Hans Clevers. Forskolin-induced swelling in intestinal organoids: An in vitro assay for assessing drug response in cystic fibrosis patients. *Journal of Visualized Experiments*, 2017(120):1–12, 2017.

Bibliography

- [84] Eyal Karzbrun, Aditya Kshirsagar, Sidney R. Cohen, Jacob H. Hanna, and Orly Reiner. Human brain organoids on a chip reveal the physics of folding. *Nature Physics*, 14(5):515–522, 2018.
- [85] Denise Serra, Urs Mayr, Andrea Boni, Ilya Lukonin, Markus Rempfler, Ludivine Challet Meylan, Michael B. Stadler, Petr Strnad, Panagiotis Papasaikas, Dario Vischi, Annick Waldt, Guglielmo Roma, and Prisca Liberali. Self-organization and symmetry breaking in intestinal organoid development. *Nature*, 2019.
- [86] B. Buchmann, Lisa K Engelbrecht, Pablo Fernández, F.P. Hutterer, M K Raich, C H Scheel, and A. R. Bausch. Mechanical plasticity of collagen directs branch elongation in human mammary gland organoids. *Nature Communications*, pages 1–10, 2021.
- [87] Benedikt Buchmann. *The role of plastic collagen remodeling during structure formation of human mammary gland organoids*. PhD thesis, Technische Universität München, 2021.
- [88] Ana Ivonne Vazquez-Armendariz and Susanne Herold. From Clones to Buds and Branches : The Use of Lung Organoids to Model Branching Morphogenesis Ex Vivo. *Frontiers in Cell and Developmental Biology*, 9(March):1–8, 2021.
- [89] Sebastian Mueller, Thomas Engleitner, Roman Maresch, Magdalena Zukowska, Sebastian Lange, Thorsten Kaltenbacher, Björn Konukiewitz, Rupert Öllinger, Maximilian Zwiebel, Alex Strong, Hsi Yu Yen, Ruby Banerjee, Sandra Louzada, Beiyuan Fu, Barbara Seidler, Juliana Götzfried, Kathleen Schuck, Zonera Hassan, Andreas Arbeiter, Nina Schönhuber, Sabine Klein, Christian Veltkamp, Mathias Friedrich, Lena Rad, Maxim Barenboim, Christoph Ziegenhain, Julia Hess, Oliver M. Dovey, Stefan Eser, Swati Parekh, Fernando Constantino-Casas, Jorge De La Rosa, Marta I. Sierra, Mario Fraga, Julia Mayerle, Günter Klöppel, Juan Cadiñanos, Pentao Liu, George Vassiliou, Wilko Weichert, Katja Steiger, Wolfgang Enard, Roland M. Schmid, Fengtang Yang, Kristian Unger, Günter Schneider, Ignacio Varela, Allan Bradley, Dieter Saur, and Roland Rad. Evolutionary routes and KRAS dosage define pancreatic cancer phenotypes. *Nature*, 554(7690):62–68, 2018.
- [90] Chris S Hughes, Lynne M Postovit, and Gilles A Lajoie. Matrigel: A complex protein mixture required for optimal growth of cell culture. *PROTEOMICS*, 10(9):1886–1890, may 2010.
- [91] Takuya Sugiyama, Cecil M. Benitez, Amar Ghodasara, Lucy Liu, Graeme W. McLean, Jonghyeob Lee, Timothy A. Blauwkamp, Roeland Nusse, Christopher V.E. Wright, Guoqiang Gu, and Seung K. Kim. Reconstituting pancreas development from purified progenitor cells reveals genes essential for islet differentiation. *Proceedings of the National Academy of Sciences of the United States of America*, 110(31):12691–12696, 2013.

- [92] Paola Bonfanti, Estelle Nobecourt, Masaya Oshima, Olivier Albagli-Curiel, Veerle Laurysens, Geert Stangé, Mozhdeh Sojoodi, Yves Heremans, Harry Heimberg, and Raphael Scharfmann. Ex Vivo Expansion and Differentiation of Human and Mouse Fetal Pancreatic Progenitors Are Modulated by Epidermal Growth Factor. *Stem Cells and Development*, 24(15):1766–1778, apr 2015.
- [93] A. Grapin-Botton. Three-dimensional pancreas organogenesis models. *Diabetes, Obesity and Metabolism*, 18:33–40, 2016.
- [94] J. R. Linnemann, H. Miura, L. K. Meixner, M. Irmeler, U. J. Kloos, B. Hirschi, H. S. Bartsch, S. Sass, J. Beckers, F. J. Theis, C. Gabka, K. Sotlar, and C. H. Scheel. Quantification of regenerative potential in primary human mammary epithelial cells. *Development*, 142(18):3239–3251, 2015.
- [95] Christopher B. Raub, Vinod Suresh, Tatiana Krasieva, Julia Lyubovitsky, Justin D. Mih, Andrew J. Putnam, Bruce J. Tromberg, and Steven C. George. Noninvasive assessment of collagen gel microstructure and mechanics using multi-photon microscopy. *Biophysical Journal*, 92(6):2212–2222, 2007.
- [96] Jiranuwat Sapudom and Tilo Pompe. Biomimetic tumor microenvironments based on collagen matrices. *Biomaterials Science*, 6(8):2009–2024, 2018.
- [97] Benedikt Buchmann, Pablo Fernández, and Andreas R Bausch. The role of nonlinear mechanical properties of biomimetic hydrogels for organoid growth The role of nonlinear mechanical properties of biomimetic hydrogels for organoid growth. 021401(June), 2021.
- [98] Chrisostomi Gialeli, Achilleas D Theocharis, and Nikos K Karamanos. Roles of matrix metalloproteinases in cancer progression and their pharmacological targeting. *The FEBS Journal*, 278(1):16–27, jan 2011.
- [99] Anna M Knapinska, Christie-Anne Estrada, and Gregg B Fields. Chapter Nine - The Roles of Matrix Metalloproteinases in Pancreatic Cancer. In Raouf A Khalil, editor, *Matrix Metalloproteinases and Tissue Remodeling in Health and Disease: Target Tissues and Therapy*, volume 148 of *Progress in Molecular Biology and Translational Science*, pages 339–354. Academic Press, 2017.
- [100] Boris I. Shraiman. Mechanical feedback as a possible regulator of tissue growth. *Proceedings of the National Academy of Sciences of the United States of America*, 102(9):3318–3323, 2005.
- [101] Alberto Puliafito, Lars Hufnagel, Pierre Neveu, Sebastian Streichan, Alex Sigal, D. Kuchnir Fygenon, and Boris I. Shraiman. Collective and single cell behavior in epithelial contact inhibition. *Proceedings of the National Academy of Sciences of the United States of America*, 109(3):739–744, 2012.

Bibliography

- [102] Fabien Montel, Morgan Delarue, Jens Elgeti, Laurent Malaquin, Markus Basan, Thomas Risler, Bernard Cabane, Danijela Vignjevic, Jacques Prost, Giovanni Cappello, and Jean François Joanny. Stress clamp experiments on multicellular tumor spheroids. *Physical Review Letters*, 107(18):1–4, 2011.
- [103] Morgan Delarue, Jean François Joanny, Frank Jülicher, and Jacques Prost. Stress distributions and cell flows in a growing cell aggregate. *Interface Focus*, 4(6), 2014.
- [104] Morgan Delarue, Jörn Hartung, Carl Schreck, Pawel Gniewek, Lucy Hu, Stephan Herminghaus, and Oskar Hallatschek. Self-driven jamming in growing microbial populations. *Nature Physics*, 12(8):762–766, 2016.
- [105] Sebastian J Streichan, Christian R Hoerner, Tatjana Schneidt, Daniela Holzer, and Lars Hufnagel. Spatial constraints control cell proliferation in tissues. *Proceedings of the National Academy of Sciences*, 111(15):5586–5591, apr 2014.
- [106] Svend Bertel Dahl-Jensen, Manuel Figueiredo-Larsen, Anne Grapin-Botton, and Kim Sneppen. Short-range growth inhibitory signals from the epithelium can drive non-stereotypic branching in the pancreas. *Physical Biology*, 13(1), 2016.
- [107] Christine Lang, Lisa Conrad, and Dagmar Iber. Organ-Specific Branching Morphogenesis. *Frontiers in Cell and Developmental Biology*, 9(June):1–17, 2021.
- [108] Mehmet Can Uçar, Dmitrii Kamenev, Kazunori Sunadome, Dominik Fatchet, Francois Lallemand, Igor Adameyko, Saida Hadjab, and Edouard Hannezo. Theory of branching morphogenesis by local interactions and global guidance. *Nature Communications*, 12(1):6830, 2021.
- [109] S Ehrig, B Schamberger, C M Bidan, A West, C Jacobi, K Lam, P Kollmannsberger, A Petersen, P Tomancak, K Kommareddy, F D Fischer, P Fratzl, and John W C Dunlop. Surface tension determines tissue shape and growth kinetics. (September):1–9, 2019.
- [110] Ronen Zaidel-Bar, Guo Zhenhuan, and Chen Luxenburg. The contractome - A systems view of actomyosin contractility in non-muscle cells. *Journal of Cell Science*, 128(12):2209–2217, 2015.
- [111] Willem-jan Pannekoek, Johan De Rooij, and Martijn Gloerich. Force transduction by cadherin adhesions in morphogenesis [version 1 ; peer review : 3 approved]. *F1000Research*, 8:1–14, 2019.
- [112] Anita S Kris, Roger D Kamm, and Alisha L Sieminski. VASP involvement in force-mediated adherens junction strengthening. *Biochemical and Biophysical Research Communications*, 375(1):134–138, 2008.
- [113] B. Ladoux, W. J. Nelson, J. Yan, and R. M. Mège. The mechanotransduction machinery at work at adherens junctions. *Integrative Biology (United Kingdom)*, 7(10):1109–1119, 2015.

- [114] Giulia Zecchin. *Branch Extension in Pancreatic Organoids An Investigation of Cell Movement Using 2D Cell Tracking*. PhD thesis, 2020.
- [115] Yoav G. Pollack, Philip Bittihn, and Ramin Golestanian. A competitive advantage through fast dead matter elimination in confined cellular aggregates. *New Journal of Physics*, 24(7), 2022.
- [116] Ryan Yanashima, Antonio A. García, James Aldridge, Noah Weiss, Mark A. Hayes, and James H. Andrews. Cutting a Drop of Water Pinned by Wire Loops Using a Superhydrophobic Surface and Knife. *PLoS ONE*, 7(9):3–8, 2012.
- [117] Medhavi Vishwakarma, Jacopo Di Russo, Dimitri Probst, Ulrich S. Schwarz, Tamal Das, and Joachim P. Spatz. Mechanical interactions among followers determine the emergence of leaders in migrating epithelial cell collectives. *Nature Communications*, 9(1), 2018.
- [118] S Okuda, N Takata, Y Hasegawa, M Kawada, Y Inoue, and T Adachi. Strain-triggered mechanical feedback in self-organizing optic-cup morphogenesis. pages 1–13, 2018.
- [119] Chii Jou Chan, Maria Costanzo, Teresa Ruiz-Herrero, Gregor Mönke, Ryan J. Petrie, Martin Bergert, Alba Diz-Muñoz, L. Mahadevan, and Takashi Hiiragi. Hydraulic control of mammalian embryo size and cell fate. *Nature*, 571(7763):112–116, 2019.
- [120] Pablo A. Fernández, Benedikt Buchmann, Andriy Goychuk, Lisa K. Engelbrecht, Marion K. Raich, Christina H. Scheel, Erwin Frey, and Andreas R. Bausch. Surface-tension-induced budding drives alveologenesis in human mammary gland organoids. *Nature Physics*, 17(10):1130–1136, 2021.
- [121] S. R. K. Vedula, M. C. Leong, T. L. Lai, P. Hersen, A. J. Kabla, C. T. Lim, and B. Ladoux. Emerging modes of collective cell migration induced by geometrical constraints. *Proceedings of the National Academy of Sciences*, 109(32):12974–12979, 2012.
- [122] M. Fethullah Simsek, Angad Singh Chandel, Didar Saparov, Oriana Q.H. Zinani, Nicholas Clason, and Ertuğrul M. Özbudak. Periodic inhibition of Erk activity drives sequential somite segmentation. *Nature*, 2022.
- [123] Yuchuan Miao, Yannis Djefal, Alessandro De Simone, Kongju Zhu, Jong Gwan Lee, Ziqi Lu, Andrew Silberfeld, Jyoti Rao, Oscar A. Tarazona, Alessandro Mongera, Pietro Rigoni, Margarete Diaz-Cuadros, Laura Min Sook Song, Stefano Di Talia, and Olivier Pourquié. Reconstruction and deconstruction of human somitogenesis in vitro. *Nature*, 614(February), 2022.
- [124] Alexander P. Browning, Jesse A. Sharp, Ryan J. Murphy, Gency Gunasingh, Brodie Lawson, Kevin Burrage, Nikolas K. Haass, and Matthew J. Simpson. Quantitative analysis of tumour spheroid structure. *eLife*, 10:1–25, 2021.

Bibliography

- [125] Rei Mukomoto, Yuji Nashimoto, Takato Terai, Takuto Imaizumi, Kaoru Hiramoto, Kosuke Ino, Ryuji Yokokawa, Takashi Miura, and Hitoshi Shiku. Oxygen consumption rate of tumour spheroids during necrotic-like core formation. *Analyst*, 145(19):6342–6348, 2020.
- [126] Ryan J. Murphy, Alexander P. Browning, Gency Gunasingh, Nikolas K. Haass, and Matthew J. Simpson. Designing and interpreting 4D tumour spheroid experiments. *Communications Biology*, 5(1), 2022.
- [127] Tamara Madácsy, Petra Pallagi, and Jozsef Maleth. Cystic Fibrosis of the Pancreas: The Role of CFTR Channel in the Regulation of Intracellular Ca²⁺ Signaling and Mitochondrial Function in the Exocrine Pancreas. *Frontiers in Physiology*, 9(December):1–11, 2018.
- [128] Barry Lubarsky and Mark A. Krasnow. Tube morphogenesis: Making and shaping biological tubes. *Cell*, 112(1):19–28, 2003.
- [129] M Ilcim Thestrup, Sara Caviglia, Jordi Cayuso, Ronja L S Heyne, Racha Ahmad, Wolfgang Hofmeister, Letizia Satriano, David G Wilkinson, Jesper B Andersen, and Elke A Ober. A morphogenetic EphB/EphrinB code controls hepatopancreatic duct formation. *Nature Communications*, (2019):1–15.
- [130] Michel Bagnat, Isla D. Cheung, Keith E. Mostov, and Didier Y.R. Stainier. Genetic control of single lumen formation in the zebrafish gut. *Nature Cell Biology*, 9(8):954–960, 2007.
- [131] Esteban Hoijman, Davide Rubbini, Julien Colombelli, and Berta Alsina. Mitotic cell rounding and epithelial thinning regulate lumen growth and shape. *Nature Communications*, 6, 2015.
- [132] Julien G. Dumortier, Jean-Léon Maître, Hervé Turlier, Mathieu Le Verge-Serandour, Anna Francesca Tortorelli, Annette Mielke, and Ludmilla de Plater. Hydraulic fracturing and active coarsening position the lumen of the mouse blastocyst. *Science*, 365(August):465–468, 2019.
- [133] Matthew Buechner. Tubes and the single *C. elegans* excretory cell. *Trends in Cell Biology*, 12(10):479–484, 2002.
- [134] Jayanta Debnath, Kenna R Mills, Nicole L Collins, Mauricio J Reginato, Senthil K Muthuswamy, Joan S Brugge, and V Gudjonsson. The Role of Apoptosis in Creating and Maintaining Luminal Space within Normal and Oncogene-Expressing Mammary Acini Brigham and Women ’ s Hospital. *Cell*, 111:29–40, 2002.
- [135] Fernando Martín-Belmonte, Wei Yu, Alejo E. Rodríguez-Fraticelli, Andrew J Ewald, Zena Werb, Miguel A Alonso, and Keith E. Mostov. Cell Polarity Dynamics Controls the Mechanism of Lumen Formation in Epithelial Morphogenesis. *Current Biology*, 18:507–513, 2008.

- [136] Wei Yu, Annette M. Shewan, Paul Brakeman, Dennis J. Eastburn, Anirban Datta, David M. Bryant, Qi Wen Fan, William A. Weiss, Mirjam M.P. Zegers, and Keith E. Mostov. Involvement of RhoA, ROCK I and myosin II in inverted orientation of epithelial polarity. *EMBO Reports*, 9(9):923–929, 2008.
- [137] George E. Davis and Kayla J. Bayless. An integrin and Rho GTPase-dependent pinocytic vacuole mechanism controls capillary lumen formation in collagen and fibrin matrices. *Microcirculation*, 10(1):27–44, 2003.
- [138] Seungbok Lee and Peter A. Kolodziej. The plakin short stop and the RhoA GTPase are required for E-cadherin-dependent apical surface remodeling during tracheal tube fusion. *Development*, 129(6):1509–1520, 2002.
- [139] Mihye Lee, Seungbok Lee, Alireza Dehghani Zadeh, and Peter A. Kolodziej. Distinct sites in E-cadherin regulate different steps in *Drosophila* tracheal tube fusion. *Development*, 130(24):5989–5999, 2003.
- [140] Aldo Ferrari, Alexey Veligodskiy, Ulrich Berge, Miriam S. Lucas, and Ruth Kroschewski. ROCK-mediated contractility, tight junctions and channels contribute to the conversion of a preapical patch into apical surface during isochoric lumen initiation. *Journal of Cell Science*, 121(21):3649–3663, 2008.
- [141] David M. Bryant, Anirban Datta, Alejo E. Rodríguez-Fraticelli, Johan Peränen, Fernando Martín-Belmonte, and Keith E. Mostov. A molecular network for de novo generation of the apical surface and lumen. *Nature Cell Biology*, 12(11):1035–1045, 2010.
- [142] Adam Navis and Celeste M. Nelson. Pulling together: Tissue-generated forces that drive lumen morphogenesis. *Seminars in Cell and Developmental Biology*, 55:139–147, 2016.
- [143] Adam Navis and Michel Bagnat. Developing pressures: FLUID forces driving morphogenesis. *Current Opinion in Genetics and Development*, 32:24–30, 2015.
- [144] Yara E. Sanchez-Corrales, Guy B. Blanchard, and Katja Röper. Radially-patterned cell behaviours during tube budding from an epithelium. *eLife*, pages 1–36, 2018.
- [145] Bruno Monier, Melanie Gettings, Guillaume Gay, Thomas Mangeat, Sonia Schott, Ana Guarner, and Magali Suzanne. Apico-basal forces exerted by apoptotic cells drive epithelium folding. *Nature*, 518(7538):245–248, 2015.
- [146] Mayank Chugh, Akankshi Munjal, and Sean G. Megason. Hydrostatic pressure as a driver of cell and tissue morphogenesis. *Seminars in Cell and Developmental Biology*, 131(April):134–145, 2022.
- [147] Boris Strilić, Jan Eglinger, Michael Krieg, Martin Zeeb, Jennifer Axnick, Pavel Babál, Daniel J. Müller, and Eckhard Lammert. Electrostatic cell-surface repulsion initiates lumen formation in developing blood vessels. *Current Biology*, 20(22):2003–2009, 2010.

Bibliography

- [148] Marta N. Shahbazi, Antonio Scialdone, Natalia Skorupska, Antonia Weberling, Gaëlle Recher, Meng Zhu, Agnieszka Jedrusik, Liani G. Devito, Laila Noli, Iain C. MacAulay, Christa Buecker, Yakoub Khalaf, Dusko Ilic, Thierry Voet, John C. Marioni, and Magdalena Zernicka-Goetz. Pluripotent state transitions coordinate morphogenesis in mouse and human embryos. *Nature*, 552(7684):239–243, 2017.
- [149] Sabyasachi Dasgupta, Kapish Gupta, Yue Zhang, Virgile Viasnoff, and Jacques Prost. Physics of lumen growth. *Proceedings of the National Academy of Sciences of the United States of America*, 115(21):E4751–E4757, 2018.
- [150] Mathieu Le Verge-Serandour and Hervé Turlier. A hydro-osmotic coarsening theory of biological cavity formation. *PLoS Computational Biology*, 17(9):1–20, 2021.
- [151] Kana Fuji, Sakurako Tanida, Masaki Sano, Makiko Nonomura, Daniel Riveline, Hisao Honda, and Tetsuya Hiraiwa. Computational approaches for simulating luminogenesis. *Seminars in Cell and Developmental Biology*, 131(June):173–185, 2022.
- [152] Hisao Honda, Nami Motosugi, Tatsuzo Nagai, Masaharu Tanemura, and Takashi Hiiragi. Computer simulation of emerging asymmetry in the mouse blastocyst. *Development*, 135(8):1407–1414, 2008.
- [153] Yukitaka Ishimoto and Yoshihiro Morishita. Bubbly vertex dynamics: A dynamical and geometrical model for epithelial tissues with curved cell shapes. *Physical Review E - Statistical, Nonlinear, and Soft Matter Physics*, 90(5):1–23, 2014.
- [154] Makiko Nonomura. Study on multicellular systems using a phase field model. *PLoS ONE*, 7(4):1–9, 2012.
- [155] M. Akiyama, M. Nonomura, A. Tero, and R. Kobayashi. Numerical study on spindle positioning using phase field method. *Physical Biology*, 16(1), 2019.
- [156] Hervé Turlier and Timo Betz. Unveiling the Active Nature of Living-Membrane Fluctuations and Mechanics. *Annual Review of Condensed Matter Physics*, 10(1):213–232, 2018.
- [157] George T. Eisenhoffer, Patrick D. Loftus, Masaaki Yoshigi, Hideo Otsuna, Chi Bin Chien, Paul A. Morcos, and Jody Rosenblatt. Crowding induces live cell extrusion to maintain homeostatic cell numbers in epithelia. *Nature*, 484(7395):546–549, 2012.
- [158] Gang Cheng, Janet Tse, Rakesh K. Jain, and Lance L. Munn. Micro-environmental mechanical stress controls tumor spheroid size and morphology by suppressing proliferation and inducing apoptosis in cancer cells. *PLoS ONE*, 4(2), 2009.
- [159] Yong Jae Kim and Jeongeun Hyun. Mechanosensitive ion channels in apoptosis and ferroptosis: focusing on the role of Piezo1. *BMB Reports*, 56(3):145–152, 2023.

- [160] Tam Luan Le, Alpha S. Yap, and Jennifer L. Stow. Recycling of E-cadherin: A potential mechanism for regulating cadherin dynamics. *Journal of Cell Biology*, 146(1):219–232, 1999.
- [161] Tam Luan Le, Shannon R. Joseph, Alpha S. Yap, and Jennifer L. Stow. Protein kinase C regulates endocytosis and recycling of E-cadherin. *American Journal of Physiology - Cell Physiology*, 283(2 52-2):489–499, 2002.
- [162] Ming Guo, Adrian F. Pegoraro, Angelo Mao, Enhua H. Zhou, Praveen R. Arany, Yulong Han, Dylan T. Burnette, Mikkel H. Jensen, Karen E. Kasza, Jeffrey R. Moore, Frederick C. Mackintosh, Jeffrey J. Fredberg, David J. Mooney, Jennifer Lippincott-Schwartz, and David A. Weitz. Cell volume change through water efflux impacts cell stiffness and stem cell fate. *Proceedings of the National Academy of Sciences of the United States of America*, 114(41):E8618–E8627, 2017.
- [163] Mihály Kovács, Judit Tóth, Csaba Hetényi, András Málnási-Csizmadia, and James R. Seller. Mechanism of blebbistatin inhibition of myosin II. *Journal of Biological Chemistry*, 279(34):35557–35563, 2004.
- [164] Robert B. Wysolmerski and David Lagunoff. Involvement of myosin light-chain kinase in endothelial cell retraction. *Proceedings of the National Academy of Sciences of the United States of America*, 87(1):16–20, 1990.
- [165] Junli Ding, Zhenzhen Li, Liang Li, Yanhui Ding, Duomei Wang, Song Meng, Qing Zhou, Shuyu Gui, Wei Wei, Huaqing Zhu, and Yuan Wang. Myosin light chain kinase inhibitor ML7 improves vascular endothelial dysfunction and permeability via the mitogen-activated protein kinase pathway in a rabbit model of atherosclerosis. *Biomedicine and Pharmacotherapy*, 128(March):1–8, 2020.
- [166] Dorota A. Nawrot, Lutfiye Yildiz Ozer, and Ayman Al Haj Zen. A Novel High Content Angiogenesis Assay Reveals That Lacidipine, L-Type Calcium Channel Blocker, Induces In Vitro Vascular Lumen Expansion. *International Journal of Molecular Sciences*, 23(9), 2022.
- [167] Claudia G. Vasquez, Vipul T. Vachharajani, Carlos Garzon-Coral, and Alexander R. Dunn. Physical basis for the determination of lumen shape in a simple epithelium. *Nature Communications*, 12(1):1–12, 2021.
- [168] Teresa Ruiz-Herrero, Kévin Alessandri, Basile V. Gurchenkov, Pierre Nassoy, and L. Mahadevan. Organ size control via hydraulically gated oscillations. *Development (Cambridge)*, 144(23):4422–4427, 2017.
- [169] Jayanta Debnath and Joan S. Brugge. Modelling glandular epithelial cancers in three-dimensional cultures. *Nature Reviews Cancer*, 5(9):675–688, 2005.
- [170] Maria Duda, Natalie J. Kirkland, Nargess Khalilgharibi, Melda Tozluoglu, Alice C. Yuen, Nicolas Carpi, Anna Bove, Matthieu Piel, Guillaume Charras, Buzz Baum,

Bibliography

- and Yanlan Mao. Polarization of Myosin II Refines Tissue Material Properties to Buffer Mechanical Stress. *Developmental Cell*, 48(2):245–260.e7, 2019.
- [171] Kai Weißenbruch, Justin Grewe, Marc Hippler, Magdalena Fladung, Moritz Tremmel, Kathrin Stricker, Ulrich S. Schwarz, and Martin Bastmeyer. Distinct roles of nonmuscle myosin ii isoforms for establishing tension and elasticity during cell morphodynamics. *eLife*, 10:1–35, 2021.
- [172] Claudia G. Vasquez, Vipul T. Vachharajani, Carlos Garzon-Coral, and Alexander R. Dunn. Physical basis for the determination of lumen shape in a simple epithelium. *Nature Communications*, 12(1):1–12, 2021.
- [173] Michelle I. Violette, Pavneesh Madan, and Andrew J. Watson. Na⁺/K⁺-ATPase regulates tight junction formation and function during mouse preimplantation development. *Developmental Biology*, 289(2):406–419, 2006.
- [174] Chen Wang, Na Wu, Beibei Pei, Xiaoyan Ma, and Wenhui Yang. Claudin and pancreatic cancer. *Frontiers in Oncology*, 13(March):1–12, 2023.
- [175] Tatjana Arsenijevic, Jason Perret, Jean Luc Van Laethem, and Christine Delporte. Aquaporins involvement in pancreas physiology and in pancreatic diseases. *International Journal of Molecular Sciences*, 20(20):1–14, 2019.
- [176] Sungmin Nam and Ovijit Chaudhuri. Mitotic cells generate protrusive extracellular forces to divide in three-dimensional microenvironments. *Nature Physics*, 14(6):621–628, 2018.
- [177] Giulia Paci and Yanlan Mao. Forced into shape: Mechanical forces in *Drosophila* development and homeostasis. *Seminars in Cell and Developmental Biology*, 120(May):160–170, 2021.
- [178] Kevin Suh, Youn Kyoung Cho, Isaac B Breinyn, and Daniel J Cohen. E-cadherin biointerfaces reprogram collective cell migration and cell cycling by forcing homeostatic conditions. *bioRxiv*, 2023.
- [179] Fabeha Fazal, Lianzhi Gu, Ivanna Ihnatovych, YooJeong Han, WenYang Hu, Nenad Antic, Fernando Carreira, James F. Blomquist, Thomas J. Hope, David S. Ucker, and Primal de Lanerolle. Inhibiting Myosin Light Chain Kinase Induces Apoptosis In Vitro and In Vivo. *Molecular and Cellular Biology*, 25(14):6259–6266, 2005.
- [180] Eric Waschkau. *Scaffold-Guided Morphogenesis of Pancreatic Ductal Adenocarcinoma Cells in a Microfluidic Chip*. Master of science (m . sc .) thesis, 2021.
- [181] Mikhail Nikolaev, Olga Mitrofanova, Nicolas Broguiere, Sara Geraldo, Devanjali Dutta, Yoji Tabata, Bilge Elci, Nathalie Brandenberg, Irina Kolotuev, Nikolce Gjorevski, Hans Clevers, and Matthias P. Lutolf. Homeostatic mini-intestines through scaffold-guided organoid morphogenesis. *Nature*, 585(September), 2020.

- [182] N. Gjorevski, M. Nikolaev, T. E. Brown, O. Mitrofanova, N. Brandenburg, F. W. DelRio, F. M. Yavitt, P. Liberali, K. S. Anseth, and M. P. Lutolf. Tissue geometry drives deterministic organoid patterning. *Science*, 375(6576), 2022.
- [183] Silvia Caianiello, Marta Bertolaso, and Guglielmo Militello. *Thinking in 3 dimensions: philosophies of the microenvironment in organoids and organs-on-chip*, volume 45. Springer International Publishing, 2023.
- [184] Chii J. Chan and Takashi Hiiragi. Integration of luminal pressure and signalling in tissue self-organization. *Development (Cambridge)*, 147(5):1–10, 2020.
- [185] Ernest Latorre, Sohan Kale, Laura Casares, Manuel Gómez-González, Marina Uroz, Léo Valon, Roshna V. Nair, Elena Garreta, Nuria Montserrat, Aránzazu del Campo, Benoit Ladoux, Marino Arroyo, and Xavier Trepát. Active superelasticity in three-dimensional epithelia of controlled shape. *Nature*, 563(7730):203–208, 2018.
- [186] D.E. Leckband and J. de Rooij. Cadherin Adhesion and Mechanotransduction. *Annual Review of Cell and Developmental Biology*, 30(1):291–315, 2014.
- [187] Mitchell K.L. Han and Johan De Rooij. Resolving the cadherin-F-actin connection. *Nature Cell Biology*, 19(1):14–16, 2017.
- [188] Anant Mamidi, Christy Prawiro, Philip A. Seymour, Kristian Honnens de Lichtenberg, Abigail Jackson, Palle Serup, and Henrik Semb. Mechanosignalling via integrins directs fate decisions of pancreatic progenitors. *Nature*, 564(7734):114–118, 2018.
- [189] Sirio Dupont, Leonardo Morsut, Mariaceleste Aragona, Elena Enzo, Stefano Gulitti, Michelangelo Cordenonsi, Francesca Zanconato, Jimmy Le Digabel, Mattia Forcato, Silvio Bicciato, Nicola Elvassore, and Stefano Piccolo. Role of YAP / TAZ in mechanotransduction. *Nature*, 2011.
- [190] Sevi Durdu, Murat Iskar, Celine Revenu, Nicole Schieber, Andreas Kunze, Peer Bork, Yannick Schwab, and Darren Gilmour. Luminal signalling links cell communication to tissue architecture during organogenesis. *Nature*, 515(7525):120–124, 2014.
- [191] Allyson Quinn Ryan, Chii Jou Chan, François Graner, and Takashi Hiiragi. Lumen Expansion Facilitates Epiblast-Primitive Endoderm Fate Specification during Mouse Blastocyst Formation. *Developmental Cell*, 51(6):684–697.e4, 2019.
- [192] Shunda Wang, Lei You, Menghua Dai, and Yupei Zhao. Mucins in pancreatic cancer: A well-established but promising family for diagnosis, prognosis and therapy. *Journal of Cellular and Molecular Medicine*, 24(18):10279–10289, 2020.
- [193] Irina Gitlin and John V. Fahy. Mucus secretion blocked at its source in the lungs. *Nature*, 603(7903):798–799, 2022.

Bibliography

- [194] Ying Lai, Giorgio Fois, Jose R. Flores, Michael J. Tuvim, Qiangjun Zhou, Kailu Yang, Jeremy Leitz, John Peters, Yunxiang Zhang, Richard A. Pfuetzner, Luis Esquivies, Philip Jones, Manfred Frick, Burton F. Dickey, and Axel T. Brunger. Inhibition of calcium-triggered secretion by hydrocarbon-stapled peptides. *Nature*, 603(7903):949–956, 2022.
- [195] Joseph Plateau. *Statique expérimentale et théorique des liquides soumis aux seules forces moléculaires*. Gauthier-Villars, 2nd edition, 1873.
- [196] Félix Savart. Mémoire sur la Constitution des Veines liquides lancées par des orifices circulaires en mince paroi. *Annales de Chimie*, 53(337), 1833.
- [197] Bastian E. Rapp. Plateau-Rayleigh Instability. *Microfluidics: Modelling, Mechanics and Mathematics*, pages 467–477, 2017.
- [198] Katharina Graessel, Christian Bächer, and Stephan Gekle. Rayleigh-Plateau instability of anisotropic interfaces. Part 1. An analytical and numerical study of fluid interfaces. *Journal of Fluid Mechanics*, 910, 2021.
- [199] Roy Bar-Ziv and Elisha Moses. Instability and "pearling" states produced in tubular membranes by competition of curvature and tension. *Physical Review Letters*, 73(10):1392–1395, 1994.
- [200] Ilan Tsafrir, Dror Sagi, Tamar Arzi, Marie Alice Guedeau-Boudeville, Vidar Frette, Daniel Kandel, and Joel Stavans. Pearling instabilities of membrane tubes with anchored polymers. *Physical Review Letters*, 86(6):1138–1141, 2001.
- [201] Roy Bar-Ziv, Tsvi Tlusty, Elisha Moses, Samuel A. Safran, and Alexander Bershadsky. Pearling in cells: A clue to understanding cell shape. *Proceedings of the National Academy of Sciences of the United States of America*, 96(18):10140–10145, 1999.
- [202] Preben Alstrøm, Victor M. Eguíluz, Morten Colding-Jørgensen, Finn Gustafsson, and Niels Henrik Holstein-Rathlou. Instability and "sausage-string" appearance in blood vessels during high blood pressure. *Physical Review Letters*, 82(9):1995–1998, 1999.
- [203] Pramod A. Pullarkat, Paul Dommersnes, Pablo Fernández, Jean François Joanny, and Albrecht Ott. Osmotically driven shape transformations in axons. *Physical Review Letters*, 96(4):1–4, 2006.
- [204] Sangwon Lee. *Drastic Fluid Uptake by Pancreatic Cancer Organoids : Tip Swelling and Pearling*. PhD thesis, University of Göttingen, 2023.
- [205] Tomomi Kiyomitsu and Iain M. Cheeseman. Cortical dynein and asymmetric membrane elongation coordinately position the spindle in anaphase. *Cell*, 154(2):391, 2013.

- [206] Jordan Jacobelli, F Chris Bennett, Priya Pandurangi, Aaron J Tooley, and Matthew F Krummel. Myosin-IIA and ICAM-1 Regulate the Interchange between Two Distinct Modes of T Cell Migration1. *The Journal of Immunology*, 182(4):2041–2050, 2009.
- [207] Junichi Maruyama, Kazutoshi Inami, Fumiyoshi Michishita, Xinliang Jiang, Hiroaki Iwasa, Kentaro Nakagawa, Mari Ishigami-Yuasa, Hiroyuki Kagechika, Norio Miyamura, Jun Hirayama, Hiroshi Nishina, Daichi Nogawa, Kouhei Yamamoto, and Yutaka Hata. Novel YAP1 Activator, Identified by Transcription-Based Functional Screen, Limits Multiple Myeloma Growth. *Molecular Cancer Research*, 16(2):197–211, 2018.
- [208] Johannes Schindelin, Ignacio Arganda-Carreras, Erwin Frise, Verena Kaynig, Mark Longair, Tobias Pietzsch, Stephan Preibisch, Curtis Rueden, Stephan Saalfeld, Benjamin Schmid, Jean Yves Tinevez, Daniel James White, Volker Hartenstein, Kevin Eliceiri, Pavel Tomancak, and Albert Cardona. Fiji: An open-source platform for biological-image analysis. *Nature Methods*, 9(7):676–682, 2012.
- [209] Stuart Berg, Dominik Kutra, Thorben Kroeger, Christoph N. Straehle, Bernhard X. Kausler, Carsten Haubold, Martin Schiegg, Janez Ales, Thorsten Beier, Markus Rudy, Kemal Eren, Jaime I. Cervantes, Buote Xu, Fynn Beuttenmueller, Adrian Wolny, Chong Zhang, Ullrich Koethe, Fred A. Hamprecht, and Anna Kreshuk. Ilastik: Interactive Machine Learning for (Bio)Image Analysis. *Nature Methods*, 16(12):1226–1232, 2019.
- [210] P Thévenaz, U E Ruttimann, and M Unser. A Pyramid Approach to Subpixel Registration Based on Intensity. *IEEE Transactions on Image Processing*, 7(1):27–41, 1998.
- [211] Ved Sharma. ImageJ plugin HyperStackReg V5.6, 2018.
- [212] Eugene Katrukha. KymoResliceWide plugin for ImageJ.
- [213] Ayshwarya Subramanian, Eriene-heidi Sidhom, Maheswarareddy Emani, Katherine Vernon, Nareh Sahakian, Yiming Zhou, Maria Kost-alimova, Michal Slyper, Julia Waldman, Danielle Dionne, Lan T Nguyen, Astrid Weins, Jamie L Marshall, Orit Rosenblatt-rosen, Aviv Regev, and Anna Greka. Single cell census of human kidney organoids shows reproducibility and diminished off-target cells after transplantation. *Nature Communications*, (2019).
- [214] Na Zhao, Reid T Powell, Xueying Yuan, Goeun Bae, Kevin P Roarty, Fabio Stossi, Martina Strempe, Michael J Toneff, Hannah L Johnson, Sendurai A Mani, Philip Jones, Clifford C Stephan, and Jeffrey M Rosen. Morphological screening of mesenchymal mammary tumor organoids to identify drugs that reverse epithelial-mesenchymal transition. (2021):1–13.

Bibliography

- [215] Bauer L LeSavage, Riley A Suhar, Nicolas Broguiere, Matthias P Lutolf, and Sarah C Heilshorn. Next-generation cancer organoids. *Nature Materials*, 21(2):143–159, 2022.
- [216] B. Buchmann, L.K. Meixner, F.P. Hutterer, M.K. Raich, C.H. Scheel, and A.R. Bausch. Mechanical plasticity of the ECM directs invasive branching morphogenesis in human mammary gland organoids. (23):1–15, 2019.
- [217] Jiranuwat Sapudom, Liv Kalbitzer, Xiancheng Wu, Steve Martin, Klaus Kroy, and Tilo Pompe. Fibril bending stiffness of 3D collagen matrices instructs spreading and clustering of invasive and non-invasive breast cancer cells. *Biomaterials*, 193(August 2018):47–57, 2019.
- [218] Jiranuwat Sapudom, Stefan Rubner, Steve Martin, Tony Kurth, Stefanie Riedel, Claudia T. Mierke, and Tilo Pompe. The phenotype of cancer cell invasion controlled by fibril diameter and pore size of 3D collagen networks. *Biomaterials*, 52(1):367–375, 2015.
- [219] Edouard Hannezo and Benjamin D. Simons. Statistical theory of branching morphogenesis. *Development Growth and Differentiation*, 60(9):512–521, 2018.
- [220] Jean Leon Maître, Ritsuya Niwayama, Herve Turlier, François Nedelec, and Takashi Hiiragi. Pulsatile cell-autonomous contractility drives compaction in the mouse embryo. *Nature Cell Biology*, 17(7):849–855, 2015.
- [221] Mojtaba Shamsipur, Ali Barati, and Ziba Nematifar. Fluorescent pH nanosensors: Design strategies and applications. *Journal of Photochemistry and Photobiology C: Photochemistry Reviews*, 39:76–141, 2019.
- [222] Maximilian Reichert, Shigetsugu Takano, Steffen Heeg, Basil Bakir, Gregory P Botta, and Anil K Rustgi. Isolation, culture and genetic manipulation of mouse pancreatic ductal cells. *Nature protocols*, 8(7):1354–1365, 2013.
- [223] Swati Parekh, Christoph Ziegenhain, Beate Vieth, Wolfgang Enard, and Ines Hellmann. The impact of amplification on differential expression analyses by RNA-seq. *Scientific Reports*, 6(January):1–11, 2016.
- [224] Evan Z. Macosko, Anindita Basu, Rahul Satija, James Nemeshe, Karthik Shekhar, Melissa Goldman, Itay Tirosh, Allison R. Bialas, Nolan Kamitaki, Emily M. Martersteck, John J. Trombetta, David A. Weitz, Joshua R. Sanes, Alex K. Shalek, Aviv Regev, and Steven A. McCarroll. Highly parallel genome-wide expression profiling of individual cells using nanoliter droplets. *Cell*, 161(5):1202–1214, 2015.
- [225] R Core Team. *R: A Language and Environment for Statistical Computing*. R Foundation for Statistical Computing, Vienna, Austria, 2021.
- [226] Michael I. Love, Wolfgang Huber, and Simon Anders. Moderated estimation of fold change and dispersion for RNA-seq data with DESeq2. *Genome Biology*, 15(12):1–21, 2014.

- [227] Gennady Korotkevich, Vladimir Sukhov, Nikolay Budin, Boris Shpak, Maxim N Artyomov, and Alexey Sergushichev. Fast gene set enrichment analysis. *bioRxiv*, page 60012, jan 2021.
- [228] Arthur Liberzon, Chet Birger, Helga Thorvaldsdóttir, Mahmoud Ghandi, Jill P. Mesirov, and Pablo Tamayo. The Molecular Signatures Database Hallmark Gene Set Collection. *Cell Systems*, 1(6):417–425, 2015.
- [229] Aravind Subramanian, Pablo Tamayo, Vamsi K. Mootha, Sayan Mukherjee, Benjamin L. Ebert, Michael A. Gillette, Amanda Paulovich, Scott L. Pomeroy, Todd R. Golub, Eric S. Lander, and Jill P. Mesirov. Gene set enrichment analysis: A knowledge-based approach for interpreting genome-wide expression profiles. *Proceedings of the National Academy of Sciences of the United States of America*, 102(43):15545–15550, 2005.
- [230] Raivo Kolde. Package ‘pheatmap’: pretty heat map. pages 1–8, 2019.

Glossary

5-FU 5-fluorouracil. 12

AMIS Apical Membrane Initiation Site. 69

aPKC atypical protein kinase C. 9, 76

ATP Adenosine triphosphate. 45

BARW branching-annihilating random walk. 7

BMP bone morphogenic protein. 7

BSA Bovine Serum Albumin. 106

CAF Cancer-Associated Fibroblasts. 14, 15

CFTR Cystic fibrosis transmembrane conductance regulator. 74

DMEM Dulbecco's Modified Eagle Medium. 17, 18, 104

dTMP deoxythymidine monophosphate. 12

ECM extracellular matrix. 3, 7, 14, 15, 17–19, 24, 28, 41, 50, 68, 84, 88, 119

EGF epithelial growth factor. 7

EGFR Epidermal Growth Factor Receptor. 13

EMT Epithelial to Mesenchymal Transition. 14, 40

ESC Embryonic Stem Cell. 15

FBS Fetal Bovine Serum. 17, 18, 104

IBDRW inflationary branching-delayed random walk. 8

IPMN Intraductal Papillary Mucinous Neoplasm. 3, 13, 14, 18, 67, 74, 87

iPSC induced Pluripotent Stem Cell. 15

MCN Mucinous Cystic Neoplasm. 13, 18, 67, 68, 74, 87

Glossary

MDCK Madin-Derby canine kidney. 30, 68, 69, 76, 83

MMP Matrix metalloproteinase. 24, 33, 38, 45, 49, 55, 57, 61

MUC1 Mucin 1. 87

PanIN Pancreatic Intraepithelial Neoplasia. 3, 13, 14, 18, 67, 74

PAP Pre-Apical Patch. 69

PDAC Pancreatic Ductal Adenocarcinoma. 2–5, 8, 10, 12–14, 17–19, 22, 30, 32, 36, 41, 46, 61, 67, 75, 77, 80, 83–85, 87, 89, 104, 118, 119

PMLC2 Phosphorylated Myosin Light Chain 2. 48

SHH sonic hedgehog. 6, 14

TGF- β transforming growth factor β . 6, 12

TRITC tetramethylrhodamine. 99